Ultrashort-Pulse Matter Interactions Using Compact Fiber CPA Technology

by

Michael K. Haines

A dissertation submitted in partial fulfillment
of the requirements for the degree of
Doctor of Philosophy
(Electrical Engineering)
in the University of Michigan
2016

Doctoral Committee:

Professor Almantas Galvanauskas, Chair
Assistant Research Scientist Aghapi G Mordovanakis
Professor Herbert Graves Winful
Professor Steven M Yalisove

Dedication:

To my parents, sister, and 3 brothers.

Table of Contents

Dedication ii

List of Figures vi

List of Abbreviations x

Chapter

1. Introduction 1

    1.1. Ultrashort Pulse – Matter Interactions and CPA Technology 1

    1.2. Compact CPA Technology: Chirped Bragg Gratings 1

    1.3. Chirped Volume Bragg Gratings in High Average Power Systems 6

    1.4. High Repetition Rate Laser to Induce Laser-Induced Periodic Surface Structures on Si 11

    1.5. Ultrashort Pulses in Eye Surgery 13

    1.6. References 18

2. Temporal Reciprocity with Chirped Volume Bragg Grating Pulse Stretchers and Compressors 23

    2.1. Introduction 23

    2.2. Numerical Modeling and Apodization Functions 24

    2.3. Results and Discussion 28

    2.4. Conclusion 36

2.5. References 37

3. Thermal Loading Effects on Chirped Volume Bragg Grating Stretcher/Compressor Systems 38

3.1. Introduction 38

3.2. Experimental Setup: 200 W CVBG-based Fiber CPA System 39

3.3. Volumetric temperature distribution in thermally-loaded high power CVBGs 41

3.4. CVBG spatial fidelity at high average powers 51

3.5. CVBG temporal fidelity at high average powers 60

3.6. Generalized Results 64

3.7. Conclusion 66

3.8. References 68

4. Polarization dependence of high spatial frequency laser-induced periodic surface structures on silicon 69

4.1. Introduction 69

4.2. Experimental Setup 70

4.3. Results and Discussion 74

4.4. Conclusion 79

4.5. Acknowledgements 79

4.6. References 80

5. Second-Harmonic Generation in Scleral Collagen as a Guide for Controlled Subsurface Photodisruption 82

5.1. Introduction 82

5.2. Theoretical Model: Second Harmonic Generation 83

5.3. Experimental Setup and Method....86
5.4. Results and Discussion....90
5.5. Conclusion....97
5.6. References....98
6. Conclusion and Future Work....100
6.1. Unanswered Questions....101
6.2. References....109
Appendix....110

List of Figures

Figure 1.1. Principle operation of CBG 2

Figure 1.2. CBG unit Bragg cell 3

Figure 1.3. Nonlinear GVD in CBG 4

Figure 1.4. Apodization of a CBG 6

Figure 1.5. Measuring spot size of propagating beam 11

Figure 1.6. Proposed eye surgery in sclera 14

Figure 2.1 Schematic illustration of apodization functions of various orders: no apodization (upper left), p = 16 (upper right), p = 6 (lower left), and p = 2 (lower right) 26

Figure 2.2 Apodizing a CVBG greatly improves pulse quality 28

Figure 2.3 Dispersion ripples in the group delay of the CVBG 31

Figure 2.4 Applying super Gaussian apodization to a CVBG greatly suppresses group delay ripple (GDR) 32

Figure 2.5 By varying the order of apodization, pulse distortions can be minimized but not eliminated 33

Figure 2.6 The quality of recompressed pulses degrades with reflectivity 36

Figure 2.7 The quality of recompressed pulses degrades with reflectivity 34

Figure 2.8 Performance of a CVBG can be analyzed using a length-bandwidth product 36

Figure 2.9 Pulse quality varies with the length-bandwidth product of a 99% reflective CBG ... 36

Figure 3.1 Experimental setup of high-power CVBG/CCC based fiber-CPA laser.....40
Figure 3.2 Optical power distribution along CVBG depended on relation of reflectivity spectrum to incident spectrum.....43
Figure 3.3 Comparison of optical power distribution along CVBG and PTR glass samples for normalized incident power.....45
Figure 3.4 Numerically simulated 3D temperature distribution in CVBG.....47
Figure 3.5 Size of incident beam determined transverse temperature distribution across the front of the CVBG.....48
Figure 3.6 Thermal image of temperature distribution at the input 5 mm X 6 mm facet of the CVBG with 150 W input beam with spectrum identical to CVBG reflectivity spectrum.....49
Figure 3.7 A comparison of simulated peak temperature at the entrance facet of the CVBG to experimental peak temperature as functions of incident power.....50
Figure 3.8 Modulation of refractive index in CVBG caused by distribution of thermal load.....51
Figure 3.9 Thermally induced modulation of refractive index in CVBG, both longitudinally and laterally, yields a GRIN lens that causes the reflected beam to focus.....52
Figure 3.10 Spectrally dependent focal length (and beam divergence) of a thermally-loaded CVBG.....54
Figure 3.11 Calculated M^2 vs. input power for CVBG.....55
Figure 3.12 Input beam used to quantify spatial distortion of reflection from CVBG with increasing input power: measured M^2 and CCD image of this input beam.....56
Figure 3.13 Experimental near-field images of the reflected beam from a CVBG at different powers incident into the CVBG.....56

Figure 3.14 Measured and calculated M^2 vs. input power for CVBG 57
Figure 3.15 The CVBG bent under a thermal load unless the mounting configuration suppressed the bending. Measured M^2 for CVBG in different mounting conditions illustrated this 58
Figure 3.16 Beam distortion was evident in images of beam reflected from a CVBG that had no top mount to suppress thermally induced bending 59
Figure 3.17 Spatial chirp of a CVBG with 50 W incident power and mounted on a copper plate 60
Figure 3.18 Computed recompressed autocorrelations and FWHM pulse duration vs. input power 62
Figure 3.19 50 W autocorrelations, theoretical and measured 63
Figure 3.20 100 W autocorrelations, theoretical and measured 63
Figure 3.21 150 W autocorrelations, theoretical and measured 64
Figure 3.22 Spatial quality of the reflected beam as a function of incident power and CVBG substrate absorption coefficient 65
Figure 3.23 Recompressed pulse quality factor Qt and temporal Strehl ratio as a function of thermal loading of CVBGs 66
Figure 4.1 Experimental CVBG-based CPA system 71
Figure 4.2 Experimental beam and pulse quality 72
Figure 4.3 Raster scanning pattern used for HSFL formation on (100) Si 73
Figure 4.4 SEM image of irradiated Si surface before etching 74
Figure 4.5 SEM of HSFL on (100) Si after etching off oxide 77
Figure 4.6 SEM of HSFL on Si, demonstrating that HSFL form perpendicular to incident polarization 78
Figure 5.1 Experimental setup for B-SHG measurements and femtosecond laser microsurgery 89

Figure 5.2 B-SHG used to determine the surface of scleral tissue. After locating the surface, B-SHG was measured 200-300 μm below the surface.....91

Figure 5.3 Measured B-SHG signal from Figure 5.2 plotted by lateral location 93

Figure 5.4 Photodisruption was attempted at a target penetration depth of 300 μm with a range of incident pulse energy 94

Figure 5.5 Energy needed for subsurface damage depended on the B-SHG conversion efficiency and the scattering coefficient of the incident beam.....96

Figure 6.1 When Si was irradiated under conditions where HSFL had formed (0.22 J/cm^2, 10^6 pulses, 23.4 W average power) but with a stationary beam instead of a translated beam, a mound of Si formed on the surface.....104

Figure 6.2 No LIPSS formed when Si was irradiated with a stationary beam (0.22 J/cm^2, 10^6 pulses, 23.4 W average power) 105

Figure 6.3 Crater formation on Si.....106

Figure 1A Longitudinal power distribution and temperature distribution along CVBG.....112

Figure 2A Fundamental operation of GRIN lens 115

List of Abbreviations

AOM	–	acousto-optic modulator
ASE	–	amplified spontaneous emission
B-SHG	–	backward-propagating second harmonic generation
BME	–	Bergmann Messgeräte Entwicklung (German company)
BPF	–	band-pass filter
BW	–	bandwidth
CBG	–	chirped Bragg grating
CCC	–	chirally-coupled core
CCD	–	charge-coupled device
CFBG	–	chirped fiber Bragg grating
CVBG	–	chirped volume Bragg grating
DM	–	dichroic mirror
EDS	–	energy dispersive X-ray spectroscopy
F-SHG	–	forward-propagating second harmonic generation
FDA	–	Food and Drug Administration
FEA	–	finite element analysis
FIB	–	focused ion beam
FWHM	–	full-width half-maximum

GDR – group delay ripple

GRIN – graded-index (or gradient index)

GVD – group velocity dispersion

HSFL – high spatial frequency laser-induced periodic surface structures

LASIK – laser-assisted *in situ* keratomileusis (or laser *in situ* keratomileusis)

LIPSS – laser-induced periodic surface structures

LNF – Lurie Nanofabrication Facility

LSFL – low spatial frequency laser-induced periodic surface structures

MC^2 – Michigan Center for Materials Characterization (formerly EMAL)

NA – numerical aperture

NIR – near infrared

OCT – optical coherence tomography

PCI – peripheral component interconnect

PMT – photo-multiplying tube

PTR – photo-thermo-refractive (a type of glass)

SEM – scanning electron microscope

SHG – second harmonic generation

SPM – self-phase modulation

SPP – surface plasmon polariton

Chapter 1

Introduction

1.1 Ultrashort Pulse – Matter Interactions and CPA Technology

In 1985, Strickland and Mourou demonstrated chirped pulse amplification (CPA) as a practical technique for generating high-energy ultrashort optical pulses [1]. The technique involved stretching a transform-limited optical pulse by applying a linear chirp to the pulse, amplifying the chirped pulse, and compressing the amplified pulse back into a transform-limited pulse. In the demonstration, the compressed, amplified pulse had 1 mJ of energy in a 1.5 ps pulse duration, which corresponds to a peak power much higher than what could be achieved by direct amplification of the transform-limited pulse. CPA was a simple, compact alternative to the dye lasers of the time [2], and it was first demonstrated using the dispersion of 1.4 km of fiber to stretch pulses and using diffraction gratings to compress amplified pulses.

1.2 Compact CPA Technology: Chirped Bragg Gratings

To make CPA systems more compact, the chirped Bragg grating (CBG) was demonstrated in 1987 [3] and proposed as an alternative pulse compressor [4] (Figure 1.1).

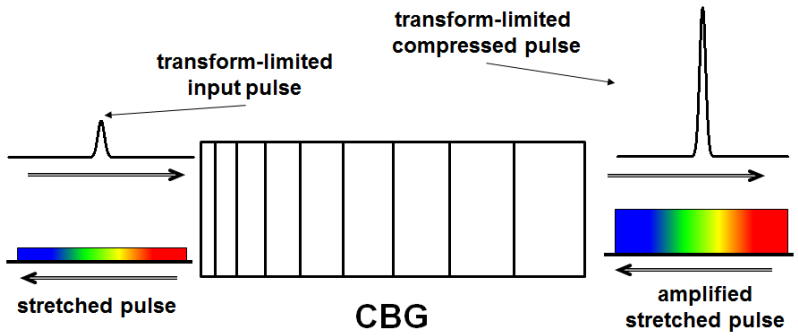

Figure 1.1. Principle operation of CBG. For a CPA system, a chirped Bragg grating (CBG) was an alternative pulse compressor to the diffraction-grating based system. The CBG could also be used to stretch pulses when acting on transform-limited input pulses.

CBGs offered several advantages in performance over the original diffraction-grating based pulse compressors. One advantage was how simple they were to use: a stretched pulse with a positive chirp could be sent into the CBG to acquire a negative chirp and be compressed into a transform-limited pulse. Conversely, a stretched pulse with negative chirp could also be compressed into a transform-limited pulse. Moreover, the CBG could stretch a transform-limited pulse.

Another advantage that the CBG offered was compactness, for the CBG needed to be only a few centimeters long to compress a pulse, whereas the diffraction-grating based pulse compressor needed 10s of centimeters [1] or even meters, depending on the bandwidth. Other advantages included the ability to be integrated into a completely monolithic system [3] and polarization-independent performance. The CBG could also stretch pulses if acting on a transform-limited pulse, whereas a diffraction-grating based pulse stretcher required an additional two lenses in a 4f-system to provide normal dispersion. The CBG was also more robust, providing repeatable performance with only minor variation with temperature or stress, whereas a diffraction-grating based pulse stretcher or compressor could introduce significant pulse distortions if the system were to become misaligned because of temperature or stress [5].

As a Bragg grating, the CBG used a series of interfaces of alternating refractive indices to define its reflection and transmission, where the spacing of two interfaces was a quarter of the incident wave, or λ/4, for a reflective Bragg grating. This spacing was determined by the Bragg condition, in which each reflection interfered constructively with subsequent reflections. The unit Bragg cell (Figure 1.2) was the λ/2 region that contributed to two reflections of the incident wave and repeated along the length of the grating.

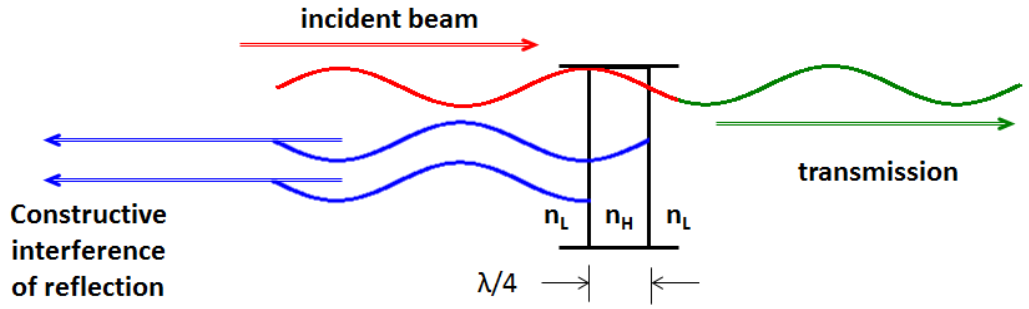

Figure 1.2. CBG unit Bragg cell. The CBG is a Bragg grating, where each unit Bragg cell (shown above) is designed to reflect a particular wavelength λ. To do this, the unit cell is composed of closely spaced interfaces, where each interface comes from the difference in refractive index in the material. The variation in length of each unit cell along the CBG allows it to reflect different wavelengths at each point, thereby compressing a stretched pulse.

The difference of n_H-n_L, known as the depth of modulation of the refractive index, was on the order of 10^{-4}–10^{-3} [6], but because the reflections interfered constructively, the overall reflectivity could be greater than 99%. For a chirped grating, the thickness of the unit Bragg cells varied linearly along the length of the CBG so that each unit cell was designed to reflect a different wavelength. The result was that each wavelength would reflect from a unique point along the CBG, and a stretched pulse could be compressed into a transform-limited pulse. To be more precise, each unit cell contributed to the phase of the reflection, but most unit cells contributed incoherently, with only a few unit cells near the effective plane of reflection contributing coherently to the reflection. The rate at which the thickness of the unit cells varied,

known as the chirp rate, and the length of the CBG defined the bandwidth that could be reflected from the grating.

The CBG had some limitations, however. For highly reflective CBGs, where reflectivity was above 70-80%, these gratings introduced distortions to the pulse. This limited the overall efficiency of a CPA system. These distortions arose because of the reflectivity of the individual unit cells in the CBG; for high reflectivity, the unit cells at the front of the grating provided a reflection that was strong enough to interfere with the reflection from the unit cells in the bulk of the grating. As a result, the reflection of each wavelength acquired a phase from these unit cells in addition to the phase from the main point of reflection, and the compressed pulse was distorted. Figure 1.3 shows how a 99% reflective, 3 cm long, 4 nm bandwidth CBG would introduce distortions from the ideal performance.

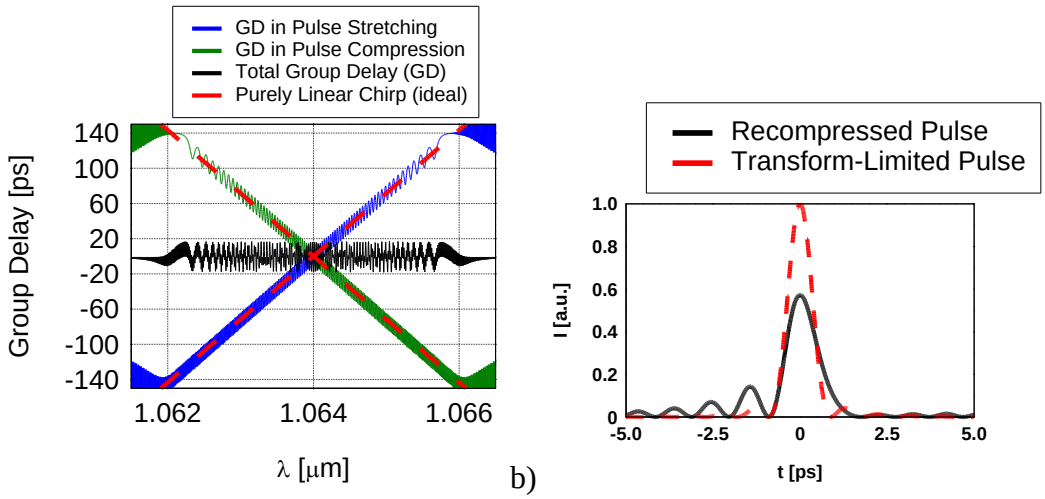

Figure 1.3. Nonlinear GVD in CBG. Although the CBG had certain advantages over a diffraction-grating based pulse compressor, its reflectivity somewhat limited its practical application. For highly reflective CBGs, such as the 99% reflective CBG shown above (3 cm length, 4 nm bandwidth with central wavelength of 1064 nm), a) the actual group delay that the CBG imprinted on the stretched pulse (blue) included strong pulse distortion compared to the ideal, purely linear chirp (red). Pulse compression with the CBG introduced further distortions (green) rather than compensating for distortions introduced by stretching. The total group delay (black) in the recompressed pulse resulted in pulse distortion, as could be seen in b) the recompressed pulse (black), which deviated substantially from its transform-limit (red). This degradation arose from reflectivity at the incident end of the CBG, which interfered with pulse compression for all wavelengths.

To diminish this effect, it was possible to apodize the depth of modulation of the refractive index. Apodization was a mathematical technique of applying a smooth edge to a function, and when it was applied to the refractive index profile of a CBG, the depth of modulation at the edge of the CBG was reduced while the depth of modulation for the rest of the CBG remained constant (Figure 1.4). During the CBG fabrication process, this was done with amplitude or phase masks. As a result of apodizing the CBG, the reflectivity of the unit cells at the incident edge of the CBG was diminished and did not contribute significantly to the overall phase of the pulse [7]. This improved the quality of the recompressed pulse, although it also reduced the overall bandwidth of the reflectivity spectrum by reducing reflectivity of the wavelengths reflected at the edges of the CBG. Given this trade-off, the apodization of the CBG needed to be chosen based on the desired pulse quality and compression efficiency in a CPA system. Using our understanding of the underlying physics of CBGs, we could explore this trade-off in more detail, particularly to know how to optimize apodization for high-reflectivity CBGs, such as CBGs with reflectivity of 95% and above. It would also be interesting to know if a CBG could be made with a sufficiently high reflectivity that apodization no longer mitigated the pulse distortions in the compressed pulse.

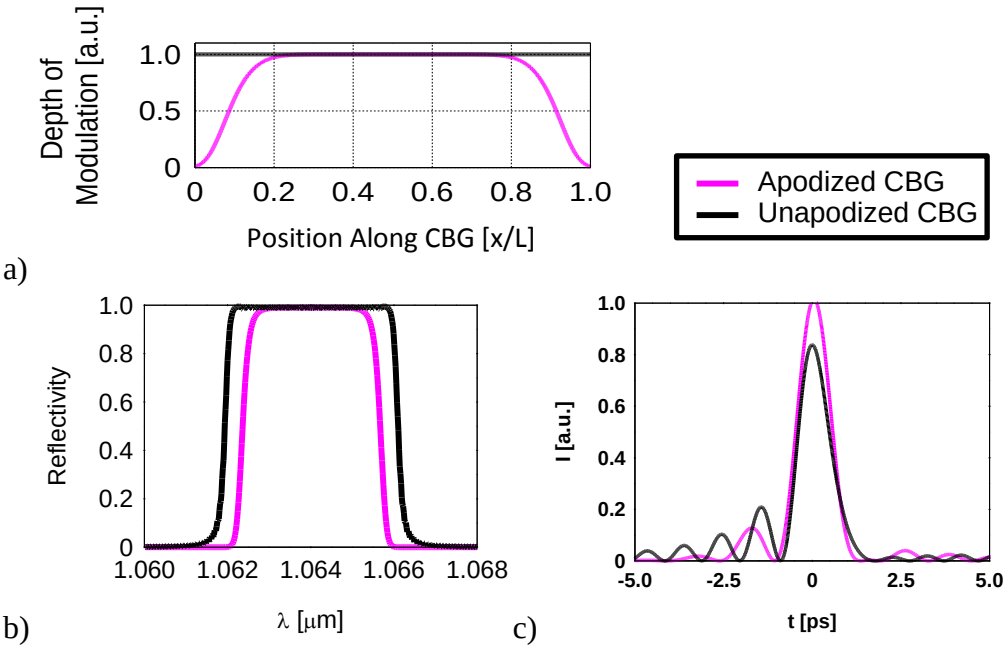

Figure 1.4. Apodization of a CBG. a) One way to improve the performance of a CBG was to apodize the depth of modulation, which reduced the reflectivity from the front of the CBG that interfered with pulse compression. Here, a super Gaussian apodization function of $\exp\{-x^6\}$ was imposed on the CBG. b) The reduced depth of modulation at the edges of the CBG resulted in a reduced reflectivity at the wings of the spectrum, and the apodized CBG had a reduced bandwidth compared to that of an unapodized CBG. c) The resulting compressed pulse from the apodized CBG had less phase distortion than the compressed pulse from the unapodized CBG. Here, the pulses were normalized in energy, so one could see that the apodized CBG compressed more energy into the main pulse, even though the reduced bandwidth of the CBG necessarily broadened the pulse.

1.3 Chirped Volume Bragg Gratings in High Average Power Systems

Two types of CBGs have been developed: the chirped fiber Bragg grating (CFBG), which was developed for fiber-based CPA systems, such as those used in fiber optic communication; and the chirped volume Bragg grating (CVBG), a free-space CBG, []. These two types of CBGs differed both in size and in material. The CFBG was several micrometers in size, typically 6-10 μm in diameter, because it was written into a fused silica fiber that had a germanium-doped (Ge-doped) core. The process of writing a CFBG involved using a UV beam, such as a 334 nm beam from an argon-ion laser [8], to induce a quasi-periodic change to the refractive index. The CVBG, however, had a rectangular cross-section and was much larger, typically 5-10 mm in one direction and up to 20 mm in the other. It was written holographically into photo-thermo-

refractive (PTR) glass instead of fused silica because the process of writing a grating into PTR glass required hundreds of mJ/cm^2 [6], whereas a comparable refractive index change in Ge-doped fused silica required hundreds of kJ/cm^2 [8]. This high fluence, combined with the high absorption of a 334 nm beam in Ge-doped fused silica ($0.3\ cm^{-1}$) [8], made fused silica an unsuitable material for CVBGs.

Each type of CBG had advantages over the other. For example, the CFBG could be integrated into a completely monolithic CPA system, such as an all-fiber laser, that was insensitive to perturbations in alignment so that stress or temperature did not significantly affect its performance. The CVBG, by contrast, needed to be properly aligned with additional free-space components. The CVBG, however, had certain advantages over the CFBG. One advantage was that the quality of stretched and compressed pulses was insensitive to errors in fabrication of the device [9]. The problem for the CFBG came from the fact that in a CPA system, feedback in the amplifier destabilized the system and could have damaged it. To prevent this, the beam from the source must be separated from the amplified stretched pulse by distance or angle in the device. This was not a problem with a diffraction-grating based CPA system or with a CVBG-based CPA system because they were free-space components, so the beam used for stretching pulses could be spatially separated from the beam used for compressing pulses, and in a CVBG-based CPA system, the beams could be at a slight angle to each other instead. Because the CFBG was fiber-based, it was built into a waveguide that did not allow for spatial or angular separation, so CFBG-based CPA systems always required two gratings, one for stretching pulses and the other for compressing them. The quality of the recompressed pulse was highly sensitive to differences in dispersion between these two gratings, so any mismatch in fabricating the CFBGs distorted the recompressed pulse.

Moreover, because the CFBG was fiber technology, the maximum peak power of the compressed pulses in a CFBG-based CPA system was limited by self-phase modulation (SPM) in the fiber [10]. SPM was the modulation of the phase of the pulse as a result of the nonlinear refractive index of the medium through which the pulse propagated. It depended on the peak irradiance of the pulse, the nonlinear refractive index of the medium, and the length of the medium, as given in Eq. 1.1:

$$\phi_{NL}(t) = -\frac{n_2 P(t)\omega_0 L}{c(\pi w_0^2/2)} \tag{1.1}$$

Here, $\phi_{NL}(t)$ was the nonlinear phase, n_2 was the nonlinear refractive index, P(t) was the peak power of the pulse, ω_0 was the central frequency of the pulse, L was the length of the material, c was the speed of light, and w_0 was the $1/e^2$ radius of the beam.

Typically, a pulse was not noticeably distorted when the total SPM was limited to $\pi/10$ radians. For the case of a standard single-mode fiber, the nonlinear refractive index was about $3*10^{-20}$ m^2/W [11] and the core diameter was 6-10 μm. For a fiber with a length of 10 cm, a pulse at a central wavelength of 1 μm would have experienced a phase shift of $\pi/10$ radians through SPM for a peak power of about 250-700 W. This especially limited the energy in an ultrashort pulse; for a Gaussian pulse with a 1 ps FWHM, this limit would be about 0.5-1.4 nJ.

The CVBG had a much larger cross-sectional area than the CFBG, however, typically on the order of mm^2. This allowed the CVBG to handle a beam with an area about 10^6 times larger than the beam in a CFBG. The nonlinear refractive index of PTR glass was comparable to that of fused silica [12], so the SPM limit for the CVBG was about 10^6 higher than the SPM limit for the CFBG, with the SPM limit of the CVBG being on the order of 1 mJ.

This made the CVBG suitable for CPA systems that required ultrashort pulses with high energy. There were many applications of these systems, such as the generation of THz pulses, which had many useful applications of their own, including material inspection, medical imaging, and astronomy [13-15]. Ultrashort pulses were also used to generate X-ray pulses, which were useful for investigating chemical reactions, phase transitions, and so forth [16-17]. A third application of ultrashort pulses was material processing, such as for micromachining or writing fiber Bragg gratings [19].

All of these applications have been demonstrated with ultrashort pulses from Ti:sapphire lasers, which operated at a kHz repetition rate and provided a few Watts of average power. The repetition rates of these lasers were limited by the thermal loading capabilities of the Ti:sapphire crystal amplifiers, which distorted the beams via thermal lensing when the average power of the laser reached a few Watts [19]. These lasers provided sufficient energy for their applications at the expense of providing pulses at only 1 kHz repetition rates. In contrast, fiber amplifiers have been shown to handle average powers on the order of 100 W while providing diffraction-limited beam quality and preserving polarization [20-21]. For the ~1 mJ ultrashort pulses that these applications required, this allowed for pulses at a repetition rate on the order of 100 kHz. Fiber amplifiers could also be more compact than other amplifier systems, such as Ti:sapphire and photonic crystal rods [22], because several meters of a fiber amplifier could be coiled into a 0.1 m^2 area.

The performance of the CVBG in a high average power system had not been characterized, however. In particular, it would be important to determine what performance limitations the CVBG would have in a high average power system, particularly regarding beam quality and pulse quality. This performance would depend on the absorption of the incident

beam, which would induce a thermal load on the CVBG. The absorption of the PTR glass substrate for 1 μm was $5*10^{-5}$ cm^{-1}, and recent developments in the process of CVBG fabrication have yielded CVBGs with absorption values of $2*10^{-4}$ cm^{-1} [6]. These low absorption values allowed the CVBG to operate in high average power systems. Experimentation and an understanding of the physics involved would enable us to identify the power-scaling limits of the CVBG. To that end, two students worked to characterize the spatial and temporal properties of the CVBG: I characterized the thermal loading and spatial fidelity of the CVBG, as described in sections 3.3 and 3.4, and Matt Rever characterized the quality of pulses recompressed with the CVBG, as described in section 3.5.

To quantify the quality of the beam reflected from the CVBG in a high average power system and thereby compare beam quality with varying average power, we used a Gaussian beam, the radius of which changed as described by Eq. 1.2 [23].

$$w(z) = w_0\sqrt{1 + \left(\frac{z}{z_R}\right)^2} \tag{1.2}$$

$$\text{where } z_R = \frac{\pi w_0^2}{\lambda} \tag{1.3}$$

Here, w was the $1/e^2$ spot size at the propagation distance z, w_0 was the spot size at focus, and z_R was the Rayleigh range, which was the area of the beam ($\pi w_0^2/2$) divided by half the wavelength λ.

When the beam was distorted, beam quality degraded and the relationship in Eq. 1.3 no longer held. Instead, the beam diverged faster than ideal and z_R decreased by the multiplicative factor M^2 (see Eq. 1.4) [24].

$$z_R{}' = \frac{z_R}{M^2} \tag{1.4}$$

To measure beam quality, we moved a razor blade into the beam path perpendicular to the direction of propagation, similar to the technique described in the introduction of [25]. The position of the razor blade required to attenuate the beam by 10% and 90%, measured by a power meter, gave a diameter that was 1.28 times larger than the radius of the beam at that location *z* along the axis of propagation (Figure 1.5). After repeating this procedure for several different points along the axis of propagation, we fit the data to Eq. 1.2 to determine the Rayleigh range of the beam, and we used Eq. 1.4 to determine the M^2 of the beam.

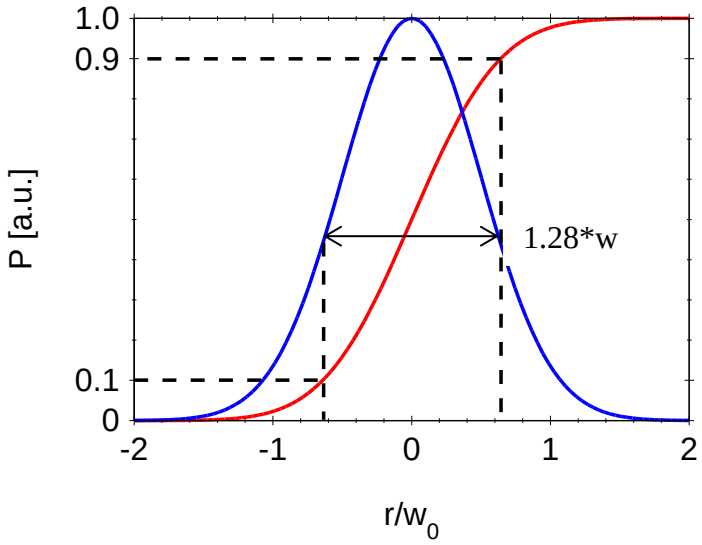

Figure 1.5. Measuring spot size of propagating beam. Beam quality was measured by attenuating the beam with a clean razor blade at 90% and 10% of the power for each point and fitting the data to Eq. 1.2. The beam is depicted in blue, and the integral (red) was the power attenuated as the razor blade as it passed through the beam. When measuring the position for 10% and 90% attenuation, the distance was 1.28 times larger than the radius of the beam.

1.4 High Repetition Rate Laser to Induce Laser-Induced Periodic Surface Structures on Si

Ultrashort pulses have found a wide variety of applications in material processing [29]. One possible application of ultrashort pulses was machining, where ultrashort pulses offered

several advantages over the nanosecond pulses currently used for machining [30-33]. Another application for material processing was the fabrication of coronary stents, which were used to keep coronary arteries open [34-35]. A third application was the bulk modification of transparent materials [36-46], which could be used to fabricate microfluidic channels in fibers [38] or novel telecommunication waveguides [42], among others.

Recently, the discovery of laser-induced periodic surface structures (LIPSS) has triggered immense interest for its applications in semiconductors, such as Si and GaAs [47-50], as well as metals such as Ti [51]. For semiconductors, LIPSS have been shown to alter the electro-optical properties of the material, resulting in higher photoconductivity for solar cell applications [52].

LIPSS are classified by the LIPSS period relative to the central wavelength of the incident pulses λ_0, where low spatial frequency LIPSS (LSFL) have periods between $0.4*\lambda_0$ and λ_0 but high spatial frequency LIPSS (HSFL) have periods of $0.3*\lambda_0$ or less [53]. The formation of both types of LIPSS was described in detail in section 2.4 of [53], and while the underlying physics guiding the formation of LSFL were generally well understood, many researchers debated the underlying physics guiding the formation of HSFL. The theory presented in [53] related HSFL formation to the ability for atomic bonds to soften and for atoms to move to other lattice sites in the crystalline structure; the atoms and the vacancies they left behind formed Frenkel pairs. If the material were undisturbed for a sufficient period of time, atoms would move into vacancies and Frenkel pairs would be annihilated, but if Frenkel pairs remained when subsequent laser pulses arrived, the roughened surface would have allowed for the generation of a surface plasmon polariton (SPP) that guided the formation of HSFL. This period of time was a material-dependent property: in GaAs, for example, Frenkel pairs lasted for at least 1 s [author of 53, private conversations]; in Si, by contrast, the Frenkel pairs did not last for 1 ms.

HSFL have been made on Si with a laser with a 80-90 MHz repetition rate [47-48], which demonstrated that creating HSFL on Si required a laser with a repetition rate between 1 kHz and 90 MHz. To determine more accurately the recombination time for Frenkel pairs in Si, and thus the repetition rate necessary for the formation of HSFL on Si, a femtosecond laser would have needed a variable repetition rate with a comparable range.

To meet this need, a novel fiber laser has been built. It provided femtosecond pulses with a 600 fs full width half maximum (FWHM) pulse duration at a variable repetition rate up to 49 MHz. The laser provided pulses with energy up to 10 μJ at an average power of up to 50 W. This laser was used to irradiate Si to study the dependence of the formation of HSFL on the repetition rate of the laser, as described in detail in Chapter 4.

The HSFL on Si were observed with a scanning electron microscope (SEM). The electron beam from a scanning electron microscope (SEM) could interact with the material in a number of ways, as some detectors in the SEM picked up electrons from the beam that bounced off nuclei in the material (back-scattered electrons) and other detectors picked up electrons from the material that were ejected by the incident beam (secondary electrons). The secondary electrons had less energy than the back-scattered electrons and were more useful for detecting surface features, whereas back-scattered electrons were more useful for distinguishing between atoms of different atomic weights. The electron beam could also excite electrons in the material, which emitted X-rays when they returned to their original state. Because the emitted X-ray energy depended on the atom, energy dispersive X-ray spectroscopy (EDS) revealed the atomic composition of material on the order of 1 μm below the surface [54].

1.5 Ultrashort Pulses in Eye Surgery

Ultrashort pulses have also been useful for many applications in biomedical engineering. One example was laser iridotomy, whereby angle-closure glaucoma was treated as pulses opened drainage canals through which ocular fluids flowed from the interior of the eye to the surface, thus reducing intraocular pressure [54]. Another use of ultrashort pulses in medical applications was in optical coherence tomography (OCT), used for non-invasive imaging of tissue samples [56]. A third example was the use of ultrashort pulses to treat cataracts [57-58], which obscured vision by making the lens opaque.

Perhaps the best-known example of the application of ultrashort pulses in biomedical engineering was the laser eye surgery known as laser-assisted *in situ* keratomileusis (LASIK). In LASIK, ultrashort pulses were used to incise the patient's cornea so that a flap could be removed to expose the middle of the cornea. Ultraviolet pulses were then used to reshape the cornea, and the flap was returned to its original position [59]. The end result for more than 95% of patients was that his vision was improved [60].

It was worth noting that while surgeons used ultrashort pulses to make subsurface incisions in the cornea, there was not an equivalent form of surgery in the sclera. Such a treatment would have allowed for treatment for presbyopia or glaucoma by allowing for subsurface drainage channels or mid-scleral drug delivery implants.

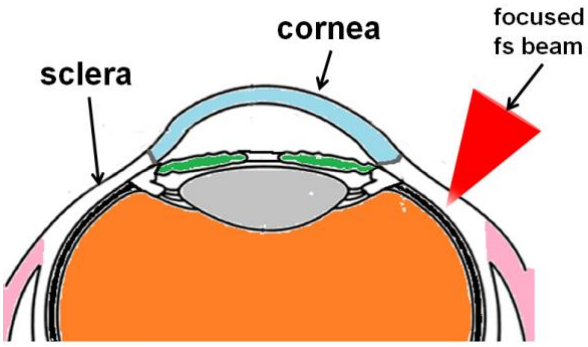

Figure 1.6. Proposed eye surgery in sclera. Eye surgery with ultrashort pulses can currently be performed in the cornea. It is difficult to translate this procedure to the sclera.

There were several challenges to implementing this kind of surgery. One challenge was that the damage threshold of the bulk of the sclera was not known, and this would have made it impossible for an ophthalmologist to select the appropriate pulse energy for a subsurface incision. Another challenge to implementing subsurface scleral surgery came from the fact that the sclera was highly scattering for near infrared (NIR) pulses, and scattering varied strongly between samples. For example, it had been measured to be as low as 10 cm^{-1} for λ = 1064 nm for one sample [62] and as high as 25 cm^{-1} for another sample [63]. The scattering attenuated incident pulses exponentially, as described in Eq. 1.5, where I was the pulse irradiance, z was the distance of propagation, I_0 was the initial pulse irradiance, and μ_s was the scattering coefficient.

$$I(z) = I_0 e^{-(\mu_a + \mu_s)z} \tag{1.5}$$

To be more accurate, absorption also attenuated incident pulses, and so Eq. 1.5 included the absorption coefficient μ_a, but the absorption of NIR pulses in human sclera was ~0.5 cm^{-1} and so was negligible when compared to scattering [63]. Further analysis, therefore, needed to account only for attenuation from scattering.

To compound this problem, strong scattering had been shown to change the size of the beam. Specifically, a 1060 nm beam was transmitted through 500 μm of scleral tissue, and the beam radius increased by an order of magnitude [64]. Clearly, if one were to implement surgery in the sclera using ultrashort pulses, it would have been necessary to measure the scattering coefficient in the patient's sclera and find additional information to determine the damage threshold at the focal region targeted for a subsurface incision.

One way to probe the sclera was to use backward-propagating second harmonic generation (B-SHG). Second harmonic generation (SHG) could be understood from the polarization of a material, described in Eq. 1.6, where *P* was the polarization, *t* was time, ϵ_0 was dielectric permittivity, $\chi^{(m)}$ was the optical susceptibility of order m, and E(t) was an incident electric field.

$$P(t) = \epsilon_0[\chi^{(1)}E(t) + \chi^{(2)}E(t)E(t) + \chi^{(3)}E(t)E(t)E(t) + \cdots] \quad (1.6)$$

SHG was the second order term in the equation, and it could have occurred in any non-centrosymmetric medium. The sclera naturally produced SHG because the collagen that formed the sclera was a non-centrosymmetric triple helix [65]. The process of SHG was highly sensitive to scattering of the incident pulses because the generation of the second harmonic depended on the square of the incident electric field. Moreover, the sclera satisfied the phase-matching conditions that allowed for a portion of the SHG to propagate backward [66]. As it propagated backward, the B-SHG also scattered, thereby introducing a second scattering variable to the measurement. This would have been a disadvantage to using SHG as a scleral probe unless one could separate the scattering coefficients of the two wavelengths.

The SHG also depended on the second-order nonlinear susceptibility of the material, $\chi^{(2)}$. Although the magnitude of $\chi^{(2)}$ in the sclera was not known, its origin was the non-centrosymmetric nature of the collagen that forms the sclera. This might have been the additional information necessary to select the incident pulse energy for scleral surgery because higher $\chi^{(2)}$ could have indicated a higher concentration of collagen in the focal volume. A pure collagen structure had a damage threshold of 0.062 Jcm^{-2}±0.06 Jcm^{-2} at 800 nm [67], whereas water,

which was the main component of the intraocular fluids that filled gaps between collagen fibrils, had an femtosecond laser induced breakdown threshold of 0.2 μJ in a 1 μm spot, which corresponded to a fluence of about 10 Jcm^{-2} [68-69].

It remained to be seen if B-SHG would provide sufficient information for an ophthalmologist to determine the energy needed for subsurface scleral incisions.

1.6 References

1 D. Strickland and G. Mourou. "Compression of Amplified Chirped Optical Pulses." Optics Communications **56**(3), pp. 219-221, 1985.

2 D. Strickland, P. Maine, M. Bouvier, S. Williamson, and G. Mourou. "Picosecond pulse amplification using pulse compression techniques." Conference on Lasers and Electro-Optics THL1, San Francisco, CA, 1986.

3 F. Ouellette. "Dispersion cancellation using linearly chirped Bragg grating filters in optical waveguides." Optics Letters **12**(10), pp 847-849, 1987.

4 A. Galvanauskas. M. E. Fermann. "Optical pulse amplification using chirped Bragg gratings." U.S. Patent 5499134 A, issued August 24, 1994.

5 P. Tournois, P. Hartemann, "Bulk chirped Bragg reflectors for light pulse compression and expansion." Optics Communications **119,** pp 569-575, 1995.

6 L. Glebova, K. Chamma, J. Lumeau, and L. Glebov. "Photo-Thermo-Refractive glass – Properties and Applications." Advances in Optical Materials AIThC2, Istanbul, Turkey, 2011.

7 R. Kashyap. Fiber Bragg Gratings. Burlington, MA: Academic Press. ISBN: 978-0-12-372579-0. 2010. Chapters 5 and 7.

8 D. S. Starodubov, V. Grubsky, and Jack Feinberg. "Bragg grating fabrication in germanosilicate fibers by use of near-UV light: a new pathway for refractive-index changes." Optics Letters **22**(14), pp 1086-1088, July 1997.

9 G. Coppola, A. Irace, A. Cutolo, and M. Iodice. "Effect of fabrication errors in channel waveguide Bragg gratings." Applied Optics **38**(9), pp 1752-1758, March 1999.

10 R. Boyd. Nonlinear Optics. Burlington, MA: Academic Press. ISBN: 978-0-12-369470-6. 2008. Chapter 7.

11 D. Milam. "Review and assessment of measured values of the nonlinear refractive-index coefficient of fused silica." Applied Optics **37**(3), January 1998.

12 S. Santran, M. Martinez-Rosas, L. Canioni, L. Sarger, L. N. Glebova, A. Tirpak, L. B. Glebov. "Nonlinear refractive index of photo-thermo-refractive glass." Optical Materials **28**, pp 401–407, 2006.

13 V. G. Bespalov, A. A. Gorodetski, I. Yu. Denisyuk, S. A. Kozlov, V. N. Krylov, G. V. Lukomski, N. V. Petrov, and S. É. Putilin. "Methods of generating superbroadband terahertz pulses with femtosecond lasers." Journal of Optical Technology **75**(10), pp 636-642, October 2008.

14 T.-J. Wang, S. Yuan, Y. Chen, and S. L. Chin. "Intense broadband THz generation from femtosecond laser filamentation." Chinese Optics Letters **11**(1), 011401, 2013.

15 N. Yang and H.-W. Du. "THz pulse generation from shaped femtosecond laser pulses interaction with gas-plasma." Optics Express **22**(21), pp 25494-25499, 2014.

16 U. Hinze, A. Egbert, and B. Chichkov. "Generation of picosecond hard-x-ray pulses in a femtosecond-laser-driven x-ray diode." Optics Letters **29**(17), pp 2079-2081, 2004.

17 K. Hatanaka, T. Ida, H. Ono, S.-I. Matsushima, H. Fukumura, S. Juodkazis, and H. Misawa. "Chirp effect in hard X-ray generation from liquid target when irradiated by femtosecond pulses." Optics Express **16**(17), pp 12650-12657, 2008.

18 I-B Sohn, M-S Lee, and J-S Woo. "Femtosecond Micromachining Applications for Optical Devices." Journal of the Optical Society of Korea **8**(3), pp 127-131 September 2004.

19 G. Wagner, M. Shiler, and V. Wulfmeyer. "Simulations of thermal lensing of a Ti:Sapphire crystal end-pumped with high average power." Optics Express **13**(20), #8379, 2005.

20 C.-H. Liu, A. Galvanauskas, B. Ehlers, F. Doerfel, S. Heinemann, A. Carter, K. Tankala, and J. Farroni. "700-W single transverse mode Yb-doped fiber laser." Conference on Lasers and Electro-Optics CMS2, San Francisco, CA, 2004.

21 C. Zhu, I. Hu, X. Ma, L. Siiman, and A. Galvanauskas. "Single-frequency and single-transverse mode Yb-doped CCC fiber MOPA with robust polarization SBS-free 511W output." in Advances in Optical Materials, OSA Technical Digest (CD) (Optical Society of America, 2011), paper AMC5.

22 C.-H. Liu, A. Galvanauskas, V. Khitrov, B. Samson, U. Manyam, K. Tankala, D. Machewirth, and S. Heinemann. "High-power single-polarization and single-transverse-mode fiber laser with an all-fiber cavity and fiber-grating stabilized spectrum." Optics Letters **31**(1), pp 17-19, 2006.

23 A. Yariv and P. Yeh. "Optical Waves in Crystals." Hoboken, NJ: John Wiley and Sons. ISBN: 0-471-43081-1. 2003.

24 R. M. Herman and T. A. Wiggins. "Rayleigh range and the M^2 factor for Bessel–Gauss beams." Applied Optics **37**(16), pp 3398-3400, 1998.

25 T. F. Johnston, Jr. "Beam propagation (M^2) measurement made as easy as it gets: the four-cuts method." Applied Optics **37**(21), pp 4840-4850, 1998.

26 T. Cardinal, B. Poumellec, and K. Hirao. "Introduction: Femtosecond Direct Laser Writing and Structuring of Materials (FDLW) feature." Optical Materials Express **1**(5), pp 996-997, September 2011.

27 Y. Prior, K. Zhang, V. Batenkov, Y. Paskover and I.S. Averbukh. "Femtosecond laser material processing - how short is short?" Nonlinear Optics ThB7, Waikoloa, HI, 2004.

28 E. Mazur. "Femtosecond laser processing of materials." CLEO: Science and Innovations STu1E1, San Jose, CA, 2014.

29 M. Gower. "Industrial applications of laser micromachining." Optics Express **7**(2), pp 56-67, July 2000.

30 D. K. Das and T. M. Pollock. "Femtosecond laser machining of cooling holes in thermal barrier coated CMSX4 superalloy." Journal of Materials Processing Technology **209**, pp 5661-5668, 2009.

31 Q. Feng, Y.N. Picard, J.P. McDonald, P.A. Van Rompay, S.M. Yalisove, and T.M. Pollock. "Femtosecond laser machining of single-crystal superalloys through thermal barrier coatings." Materials Science and Engineering A **430**, 203–207, 2006.

32 Q. Feng, Y. N. Picard, H. Liu, S. M. Yalisove, G. Mourou and T. M. Pollock. "Femtosecond laser micromachining of single-crystal superalloys." Superalloys **2004**, pp 687-696, 2004.

33 A.G. Evans, D.R. Mumm, J.W. Hutchinson, G.H. Meier, and F.S. Petitt. "Mechanisms controlling the durability of thermal barrier coatings." Progress in Material Science **46**, pp 505-553, 2001.

34 N. Muhammad and L. Li. "Underwater femtosecond laser micromachining of thin nitinol tubes for medical coronary stent manufacture." Applied Physics A **107**, pp 849–861, 2012.

35 L. Li and N. Muhammad. "Ultra-short Pulse Laser Precision Machining of Coronary Stents." Laser and Tera-Hertz Science and Technology MF4A.3, Wuhan, China, 2012

36 C. Hnatovsky, E. Simova, P. P. Rajeev, D. M. Rayner, P. B. Corkum, and R. S. Taylor. "Applications of Femtosecond Laser-Induced Self-Assembled Nanocracks in Fused Silica Glass." Bragg Gratings, Photosensitivity, and Poling in Glass Waveguides BTuD1, Quebec City, Canada, 2007.

37 R. S. Taylor, C. Hnatovsky, E. Simova, D. M. Rayner, V. R. Bhardwaj, and P. B. Corkum. "Ultra-High Resolution Index of Refraction Profiles of Femtosecond Laser Modified Silica Structures." Conference on Lasers and Electro-Optics CWA18, Baltimore, MD, 2003.

38 C. Hnatovsky, R. S. Taylor, R. Bhardwaj, E. Simova, D. M. Rayner and P. B. Corkum. "3-D Fabrication of Microfluidic Channels in Fused Silica Using Focused Femtosecond Laser Beams and Selective Chemical Etching." Conference on Lasers and Electro-Optics CThCC2, Baltimore, MD, 2005.

39 C. Hnatovsky, R. S. Taylor, R. Bhardwaj, E. Simova, D. M. Rayner and P. B. Corkum. "Long-range periodic planar nanostructures produced in glass by femtosecond laser dielectric modification." Conference on Lasers and Electro-Optics CThV1, Baltimore, MD, 2005.

40 C. Hnatovsky, E. Simova, R. S. Taylor, R. Pattathil, R. Bhardwaj, D. M. Rayner, and P. B. Corkum. "Direct Writing of Nanoporous Capillaries inside Fused Silica Using a Focused Femtosecond Laser Beam." Conference on Lasers and Electro-Optics CMHH4, Long Beach, CA, 2006.

41 E. Simova, C. Hnatovsky, R. S. Taylor, J. Liu, R. Pattathil, R. Bhardwaj, D. M. Rayner, and P. B. Corkum. "Rewritable Nanogratings in Fused Silica Using a Focused Femtosecond Laser Beam." Conference on Lasers and Electro-Optics CMX4, Long Beach, CA, 2006.

42 C. A. Merchant, S. M. Eaton, R. Iyer, A. Helmy, P. R. Herman, J. S. Aitchison. "Low-loss Waveguides Fabricated in $KGd(WO_4)_2$ by High Repetition Rate Femtosecond Laser." Conference on Lasers and Electro-Optics CPDB8, Baltimore, MD, 2007.

43 R. S. Taylor, C. Hnatovsky, and E. Simova. "Applications of femtosecond laser induced self-organized planar nanocracks inside fused silica glass." Laser and Photonics Review **2**(1-2), pp 26-48, 2008.

44 R. S. Taylor, C. Hnatovsky, E. Simova, R. Pattathil, J. Liu, D. M. Rayner, and P. B. Corkum. "Femtosecond Laser Nanomachining Applications in Fused Silica." Conference on Lasers and Electro-Optics CThJ1, Baltimore, MD, 2007.

45 R. S. Taylor, C. Hnatovsky, E. Simova, D. M. Rayner, V. R. Bhardwaj, and P. B. Corkum. "Femtosecond Laser Fabricated Nanostructures in Silica Glass." Conference on Lasers and Electro-Optics, Baltimore, MD, 2003.

46 S. Juodkazis, D. de Ligny, R. Buividas, C. Hnatovsky, E. G. Gamaly, A. V. Rode. "Femtosecond Laser Structuring of Amorphous and Crystalline Materials." International Quantum Electronics Conference / Conference on Lasers and Electro-Optics / Pacific Rim, ACOFT Presentation, Sydney, Australia, 2011.

47 R. Le Harzic, H. Schuck, D. Sauer, T. Anhut, I. Riemann and K. König. "Sub-100 nm nanostructuring of silicon by ultrashort laser pulses." Optics Express **13**(17), pp 6651-6656 August 2005.

48 R. Le Harzic, D. Dörr, D. Sauer, M. Neumeier, M. Epple, H. Zimmermann, and F. Stracke. "Large-area, uniform, high-spatial-frequency ripples generated on silicon using a nanojoule-femtosecond laser at high repetition rate." Optics Letters **36**(2), pp 229-231, 2011.

49 H. Zhai, X. Wang, and H. Hu. "Diagnosis of Transparent Ejected Material in Femtosecond Laser Ablation." CLEO Pacific Rim, Shanghai, China, 2009.

50 A. A. Ionin, Y. M. Klimachev, A. Y. Kozlov, S. I. Kudryashov, A. E. Ligachev, S. V. Makarov, L. V. Seleznev, D. V. Sinitsyn, A. A. Rudenko, R. A. Khmelnitsky. "Direct femtosecond laser fabrication of antireflective layer on GaAs surface." Applied Physics B (Lasers and Optics), **111**, pp 419-423, 2013.

51 S. Höhm, A. Rosenfeld, J. Krüger, and J. Bonse. "Laser-induced periodic surface structures on titanium upon single- and two-color femtosecond double-pulse irradiation." Optics Express **23**(20), 245810, 2015.

52 Z-Y Zhao, Z-Q Song, W-Z Shi, and Q-Z Zhao. "Optical absorption and photocurrent enhancement in semi-insulating gallium arsenide by femtosecond laser pulse surface microstructuring." Optics Express **22**(10), #208639, 2014.

53 Abere, M. "From Point Defects to Ripples: Ultrafast Laser Induced High Spatial Frequency Laser Induced Periodic Surface Structures." Dissertation, University of Michigan, Ann Arbor 2015. Print.

54 R.S. Frenkel and D. W. Aitken. "Energy Dispersive X-Ray Emission Spectroscopy." Applied Spectroscopy **24**(6), pp 557-566, 1970.

55 R. M. Klapper. "Q switched Neodymium:YAG Laser Iridotomy." Ophthalmology **91**(9), pp 1017–1021 1984.

56 W. J. Choi, J. Na, S. Y. Ryu, B. H. Lee, and D-S. Ko. "Realization of 3-D Topographic and Tomographic Images with Ultrahigh-resolution Full-field Optical Coherence Tomography." Journal of the Optical Society of Korea **11**(1), pp 18-25, March 2007.

57 B. M. Wu, G. P. Williams, A. Tan, and J. S. Mehta. "A Comparison of Different Operating Systems for Femtosecond Lasers in Cataract Surgery." Journal of Ophthalmology **2015**, 616478, 2015.

58 S. Serrao, G. Lombardo, G. Desiderio, L. Buratto, D. Schiano-Lomoriello, M. Pileri, and M. Lombardo. "Analysis of Femtosecond Laser Assisted Capsulotomy Cutting Edges and Manual Capsulorhexis Using Environmental Scanning Electron Microscopy." Journal of Ophthalmology **2014**, 520713, 2014.

59 J. Schwiegerling. "LASIK and Beyond." Optics and Photonics News, pp 30-33 January 2002.

60 K. Solomon, L. E. Fernández de Castro, H. P. Sandoval, J. M. Biber, B. Groal, K. D. Neff, M. S. Ying, J. W. French, E. D. Donnenfeld, and R. L. Lindstrom.

"LASIK World Literature Review: Quality of Life and Patient Satisfaction." Ophthalmology **116**(4), pp 691–701, April 2009.

61 Y. Komai and T. Ushikif. "The Three-Dimensional Organization of Collagen Fibrils in the Human Cornea and Sclera." Investigative Ophthalmology & Visual Science **32**(8), pp 2244-2258, 1991.

62 A. Vogel, C. Dlugos, R. Nuffer, and R. Bringruber. "Optical Properties of Human Sclera, and Their Consequences for Transscleral Laser Applications." Lasers in Surgery and Medicine **11**, pp 331-340, 1991.

63 A. N. Bashkatov, E. A. Genina, V. I. Kochubey, and V. V. Tuchin. "Optical Properties of Human Sclera in Spectral Range 370–2500 nm." Biomedical Optics and Spectroscopy **109**(2) pp 197-204, 2010.

64 Z. S. Sacks, R. M. Kurtz, T. Juhasz. "High precision subsurface photodisruption in human sclera." Journal of Biomedical Optics **7**(3), pp 442–450, July 2002.

65 Lodish H, Berk A, Zipursky SL, et al. Molecular Cell Biology. 4th edition. New York: W. H. Freeman; 2000. Section 22.3, Collagen: The Fibrous Proteins of the Matrix. Available from: http://www.ncbi.nlm.nih.gov/books/NBK21582/

66 R. LaComb, O. Nadiarnykh, S. S. Townsend, P. J. Campagnola. "Phase matching considerations in second harmonic generation from tissues: Effects on emission directionality, conversion efficiency and observed morphology." Optics Communications **281**, pp 1823–1832, 2008.

67 Y. Liu, S. Sun, S. Singha, M. R. Cho, R. J. Gordon. "3D femtosecond laser patterning of collagen for directed cell attachment." Biomaterials **26**, pp 4597–4605, 2005.

68 E. N. Glezer, C. B. Schaffer, N. Nishimura, and E. Mazur. "Minimally disruptive laser-induced breakdown in water." Optics Letters **22**(23) pp 1817-1819, 1997.

69 C. B. Schaffer, N. Nishimura, and E. Mazur. "Thresholds for femtosecond laser-induced breakdown in bulk transparent solids and water." URL: http://mazur-www.harvard.edu/

Chapter 2

Temporal Reciprocity of Chirped Volume Bragg Grating Pulse Stretchers and Compressors

2.1 Introduction

Chirped pulse amplification (CPA) is necessary for any applications of ultrashort-pulses that requires high energy pulses, such as micromachining, THz generation, X-ray generation, and so forth [1-3]. The emergence of fiber laser technology has enabled compact, monolithic, and robust laser systems that can lead to practical CPA systems. To realize fully the potential for practical CPA systems, the pulse stretchers and compressors need to be compact, and so the conventional diffraction-grating based pulse stretchers and compressors, which are large and not robust, should be replaced with a more practical alternative. Chirped volume Bragg gratings (CVBGs) offer such an alternative because they are compact pulse stretchers and compressors [4] that are only a few centimeters long. Additionally, a CVBG can serve as both pulse stretcher and compressor by virtue of its symmetric geometry.

This practical technology has some trade-offs, however. One trade-off is the degradation of temporal reciprocity with increasing reflectivity of a CVBG. Perfect temporal reciprocity would yield complete reproducibility of the initial pulse profile after it is stretched and recompressed in the same CVBG. Reciprocity is broken by the abrupt change in depth of modulation at the edges of the grating [6-7], and so the dispersion of the CVBG acquires a non-reciprocal ripple that distorts the recompressed pulse. This ripple increases with increasing

reflectivity of the CVBG, and so the maximum grating reflectivity for practical applications is limited to approximately 80% [6]. This is comparable to the typical diffraction-grating based pulse compressor efficiency of about 60-80%, which is limited by the fact that four grating reflections are needed for pulse compression. Nevertheless, it would be beneficial to access the CVBG reflectivities of more than 95%, which are achievable by the volume grating fabrication technology.

One could anticipate that it would be possible to mitigate or even eliminate the temporal non-reciprocity effects by removing this abrupt change in depth of modulation at the edge of the grating through apodization [7-9]. Our analysis shows that the temporal non-reciprocity can never be completely removed through apodization. We also show, however, that the non-reciprocity can be significantly reduced for a certain optimized apodization profile, to a degree that practically useful CVBG pulse stretchers and compressors with efficiencies exceeding 95% can be achieved.

2.2 Numerical Modeling and Apodization Functions

In the presented analysis, the performance of apodized and unapodized CVBG is modeled with transfer-matrix calculations of the complex reflectivity spectrum, as described in [10]. The transfer matrix of a unit Bragg cell, $M_{\text{unit cell}}$, is repeated below [Eq. 2.1], where the meaning of each symbol is identical to the meaning presented in [10]. Transfer-matrix calculations agree well with direct integration of coupled-mode equations [10], and also were shown to agree well with experimental results [6].

$$M_{unit\ cell} = \frac{1}{1-r^2}\begin{bmatrix} e^{i\phi} - r^2 e^{-i\Delta\phi} & 2irsin(\phi_h) \\ -2irsin(\phi_h) & e^{-i\phi} - r^2 e^{i\Delta\phi} \end{bmatrix} \tag{2.1}$$

To quantify the effect of apodization on performance of a CVBG, the same form of apodization is used throughout the analysis, specifically the super Gaussian function. The order *p* of the super Gaussian function in Eq. 2.2 is the quantification of the apodization [Eq. 2.2]:

$$\Delta n(\lambda) = \Delta n_0 \exp\left\{-\left(\frac{\lambda-\lambda_0}{CR*\frac{L}{2}}\right)^p / |ln(0.01)|\right\} \quad (2.2)$$

Here, the maximum depth of modulation Δn_0 is multiplied to a super Gaussian of order *p*. The CVBG has a central wavelength λ_0, a chirp rate *CR*, and a length *L*, and reflectivity at the edges of the CVBG is 1% of Δn_0. Figure 2.1 schematically illustrates few examples of apodization.

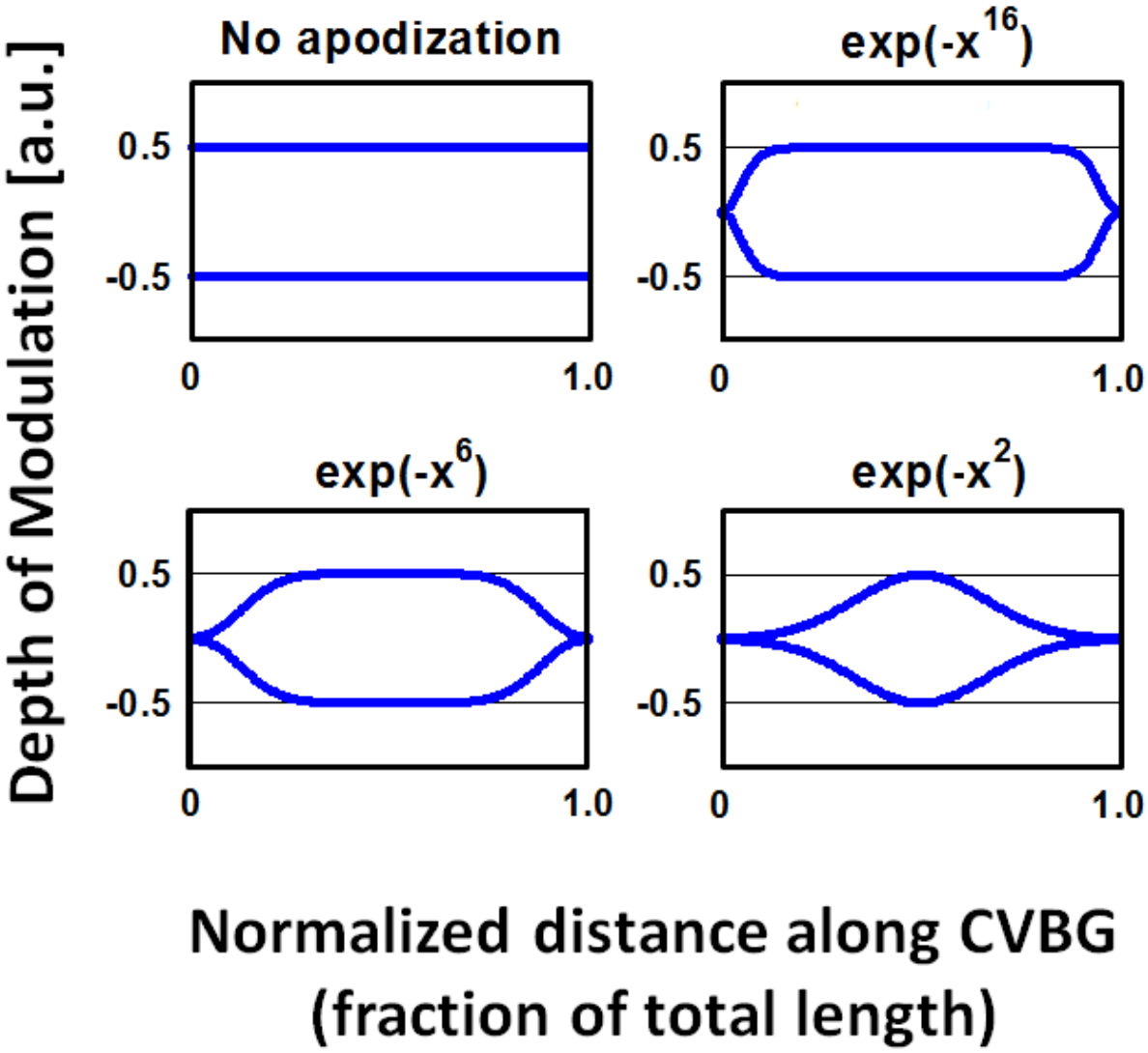

Figure 2.1 Schematic illustration of apodization functions of various orders: no apodization (upper left), p = 16 (upper right), p = 6 (lower left), and p = 2 (lower right).

To explore the reciprocity of a CVBG, we adopt the following procedure. To discount any effects associated with the spectral shape of an input signal, we take the input signal to be bandwidth-limited at the input of the CVBG stretcher, and with a "flat-top" bandwidth significantly exceeding the CVBG bandwidth, i.e. signal spectrum completely filling the reflectivity spectrum of the CVBG. Pulse stretching is simulated by launching the input signal

into one side of the CVBG, and pulse recompression is simulated by launching the stretched pulse into the opposite side of the CVBG.

For quantifying the magnitude of pulse distortions after the pulse recompression, we introduce the effective pulse duration τ [Eq. 2.3], defined in a manner analogous to the effective mode area of a fiber. This definition captures the spread of energy in time, accounting for pre-pulses and post-pulses, which usually is not well-captured just by using the full-width at half-maximum (FWHM) pulse duration.

$$\tau = \frac{\left(\int_{-\infty}^{\infty} P(t)dt\right)^2}{\int_{-\infty}^{\infty} P(t)^2 dt} \tag{2.3}$$

Here, P(t) is the recompressed pulse power temporal profile. Furthermore, we introduce pulse quality *Q*, which is defined as the ratio of effective pulse durations of a recompressed pulse and of its transform-limit [Eq. 2.4]. This quality factor effectively characterizes the degradation of the distribution of pulse energy after the recompression.

$$Q = \frac{\tau_{recompressed}}{\tau_{transform-limited}} \tag{2.4}$$

Using this figure of merit, the ideal value of *Q* is 1, which occurs when a recompressed pulse is transform-limited and there are no dispersion-induced pulse distortions. Increasing values of *Q* indicate the amount of CVBG-induced distortions on the recompressed pulse, i.e. for any finite amount of CVBG non-reciprocity Q-value of the recompressed pulse will be higher than 1. Figure 2.2 illustrates how distortions to the recompressed pulse appear for two specific

Q values: Q = 2.3 (in (a)) and Q = 1.18 (in (b)). Because some of the energy being "shifted" to pulse power, peak power of the recompressed pulses degrades: it is ~60% for Q = 2.3, and ~90% for Q = 1.18 compared to the undistorted pulse. The maximum acceptable Q value should be defined based on the particular application of ultrashort pulses. However, based on the results presented in this illustration, we can assume that for Q $\leq$ 1.2, recompressed pulses are of practically acceptable quality.

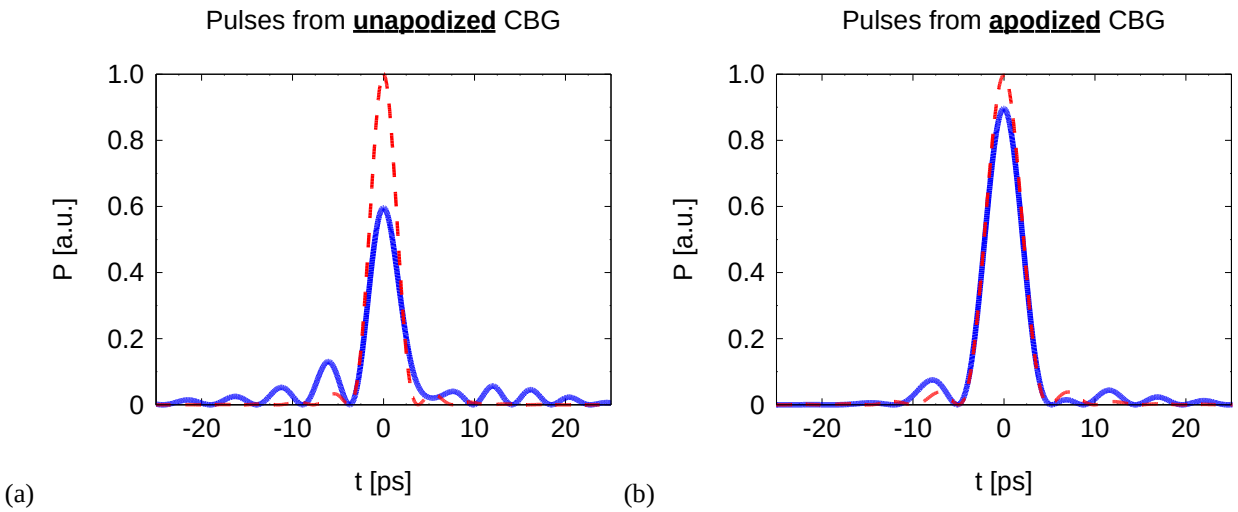

Figure 2.2 Apodizing a CVBG greatly improves pulse quality. Comparing the recompressed pulses from an unapodized CVBG to those from a CVBG apodized with a super Gaussian apodization function of the order $p = 8$ (from Eq. 2.2), it is clear that apodizing a CVBG greatly suppresses pulse distortion. Both CVBGs are 3 cm long with 99% reflectivity and a 0.9 nm bandwidth. (a) Recompressed pulses (solid) from an unapodized CVBG are strongly distorted compared to their transform-limit (dashed), and $Q = 2.30$ (Eq. 2.4). (b) Recompressed pulses (solid) from an apodized CVBG are nearly transform-limited, and $Q = 1.18$.

2.3 Results and Discussion

Distortions in the recompressed pulses due to the non-reciprocity of unapodized CVBGs have been demonstrated both theoretically and experimentally [6]. The degree of non-reciprocity increases with increasing grating reflectivity, so the reflectivity of a practically useful, unapodized CVBG cannot exceed about 80%. The non-reciprocity is associated with the abrupt edges of the grating structure, which lead to spurious weak reflections from the front and the

back of the grating that interfere with the strong main signal reflected from the reflection band of the grating. This interference leads to dispersion ripples, which are asymmetric with respect to the wavelengths reflected at the "front" and the "back" end of the grating (Figure 2.3). For a pulse stretched and compressed with the same grating, the ripples would add for each propagation direction, thus producing a non-reciprocal dispersion contribution onto the phase of the recompressed pulse.

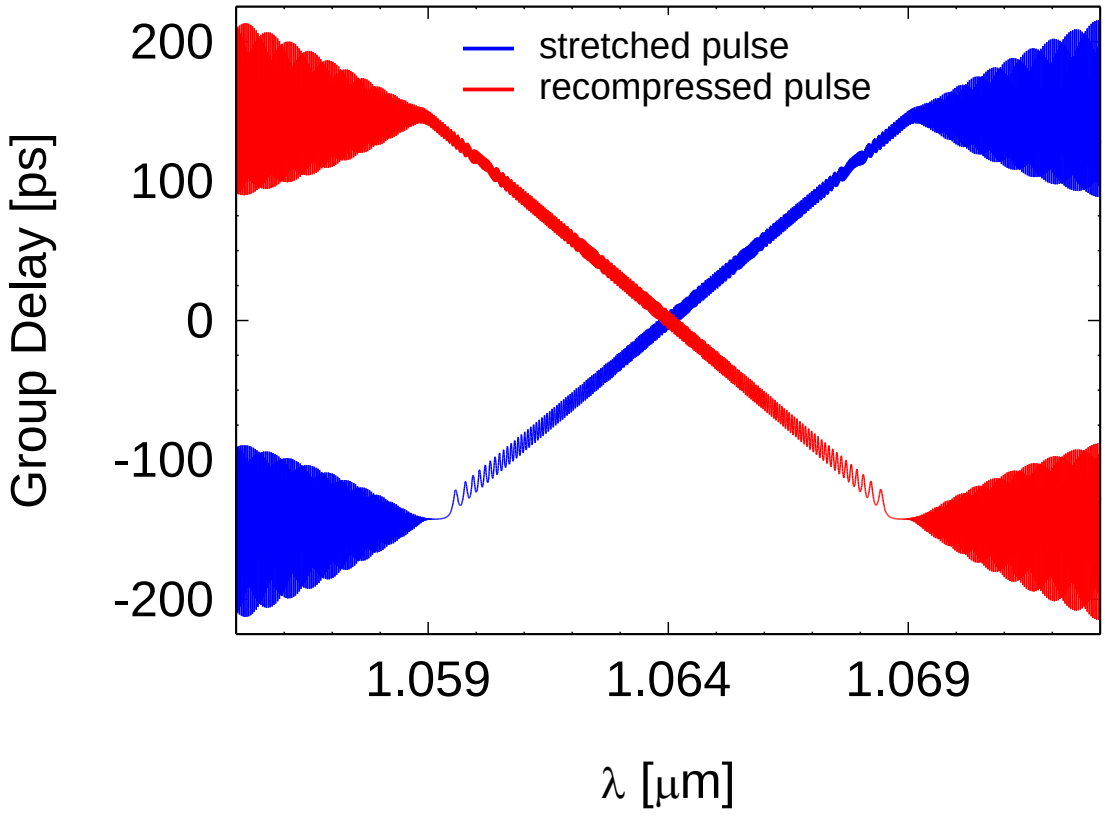

Figure 2.3 Dispersion ripples in the group delay of the CVBG. CVBG bandwidth is 10 nm. Because the group delay of the stretched and recompressed pulses are not opposite with respect to each other, the CVBG is non-reciprocal.

One could anticipate that if a grating is apodized, the smooth transitions of the modulated reflectivity at the grating edges would reduce these spurious reflections, and thus reduce the

non-reciprocal dispersion contribution of the grating. Indeed, apodization improves the pulse quality of a CVBG (Figure 2.2). In this figure, recompressed pulses from an unapodized CVBG and a CVBG apodized with a super Gaussian of the order $p = 8$ are shown and compared to the corresponding bandwidth-limited pulses. The improvement of the recompressed pulse quality is apparent. For the unapodized CVBG, the recompressed pulse peak power is only about 60% of the peak power of the bandwidth-limited pulse, and Q = 2.3, indicating significant pulse energy outside the main pulse. For the apodized CVBG, the peak power is about 90% of the peak power of the bandwidth-limited pulse, and Q = 1.18, corresponding to a pulse with significantly smaller temporal distortions.

It is instructive to compare the residual dispersion of unapodized and apodized CVBGs. The residual dispersion is calculated after the pulse stretching and recompressing with the same grating. The group delay ripple (GDR) of the unapodized CVBG consists of a combination of high and low spectral frequency oscillations (Figure 2.4). These oscillations have been shown to distort compressed pulses [12]. In contrast, the GDR of the apodized CVBG consists mainly of low spectral frequency oscillations, thus reducing pulse distortions.

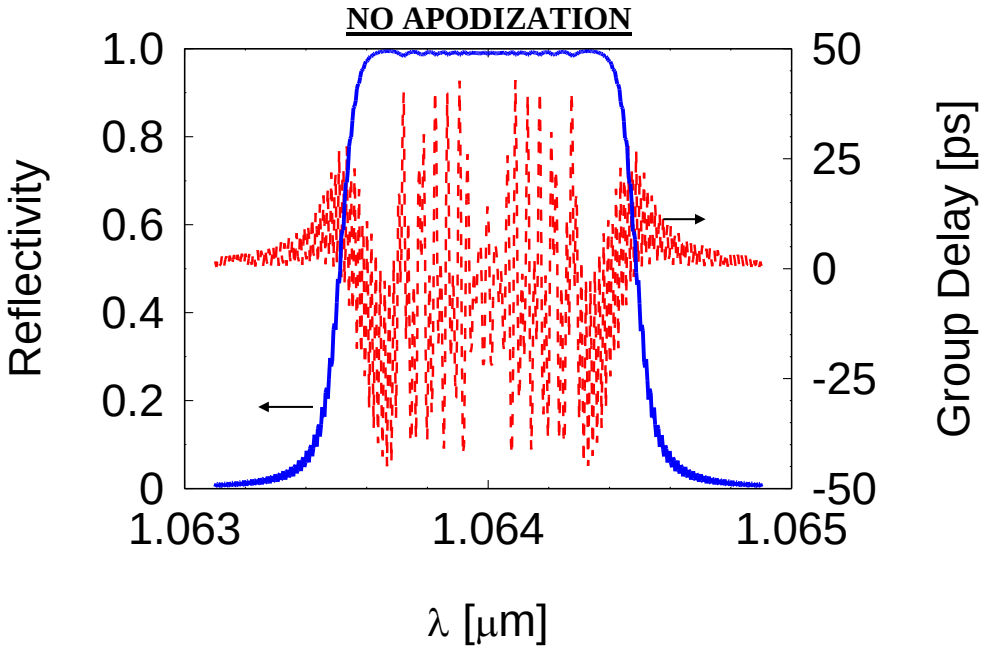

(a)

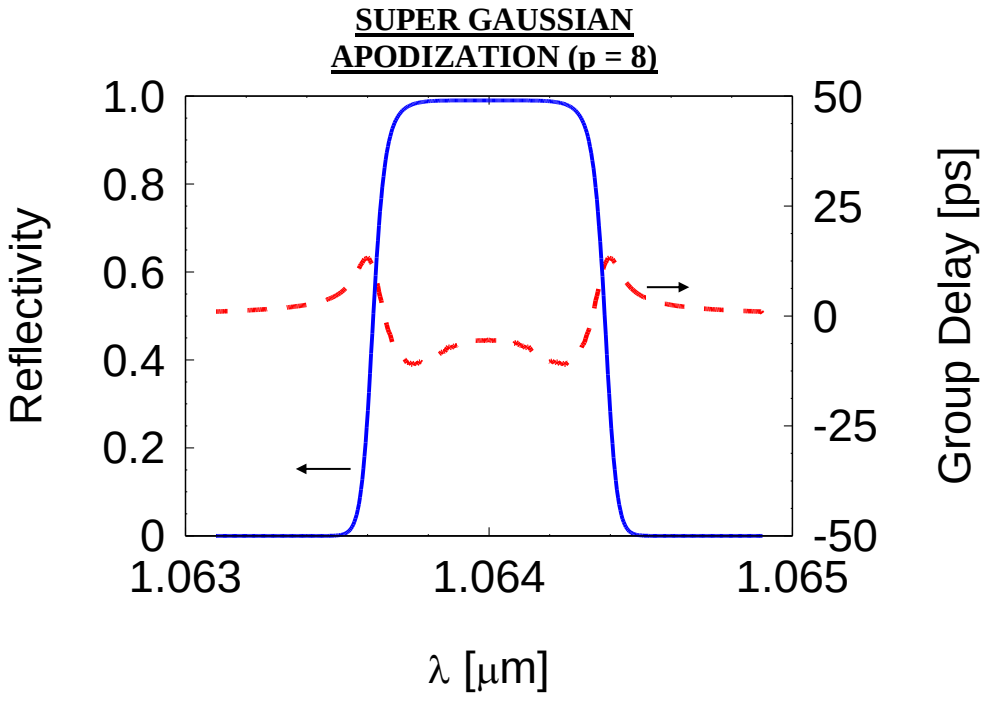

(b)

Figure 2.4 Applying super Gaussian apodization to a CVBG greatly suppresses group delay ripple (GDR). Using the same parameters as in Figure 2.2, (a) the unapodized CVBG shows more phase distortion than (b) the apodized CVBG.

It is worth exploring the possibility of completely eliminating non-reciprocal dispersion by using a particular apodization profile. The results presented in Figure 2.5 show that the non-reciprocal dispersion can be minimized but not eliminated. The figure shows the dependence of pulse quality on varying super Gaussian apodization profiles for different narrow and broadband CVBGs. This dependence varies with the CVBG bandwidth, but the optimum always occurs for the range of orders of super Gaussian apodization $p \approx 6$–8, where pulse quality reaches Q ≈ 1.1 - 1.2.

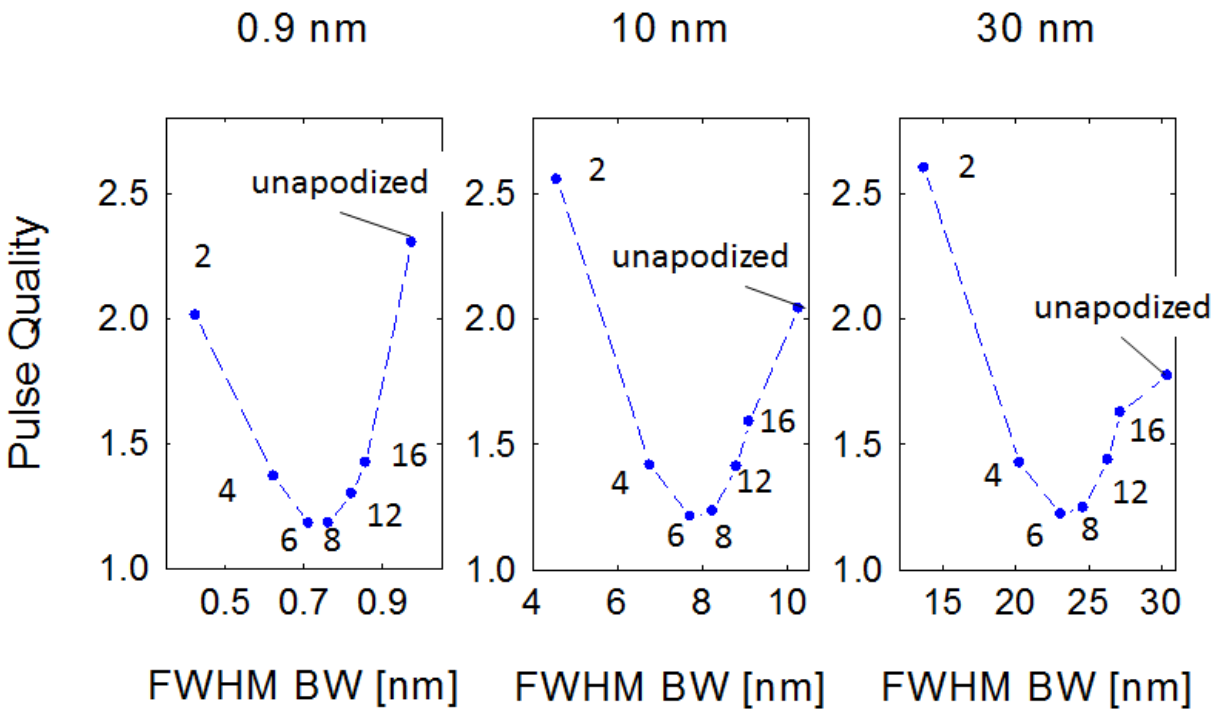

Figure 2.5 By varying the order of apodization, pulse distortions can be minimized but not eliminated. The optimal pulse quality is achieved for $p \approx$ 6-8. The CVBGs are 99% reflective and 3 cm long, and the bandwidth is listed at the top of each plot. The order of apodization p is listed next to each point.

It is interesting to note that recompressed pulse quality appears to degrade for very "smooth" apodization profiles, and becomes most pronounced for the Gaussian profile. We also explored how these apodization-shape dependencies are affected by different CBG reflectivity

magnitudes (Figure 2.6-Figure 2.7). As anticipated, distortions of the recompressed pulse shape increase with increasing CBG reflectivity for all apodization profiles.

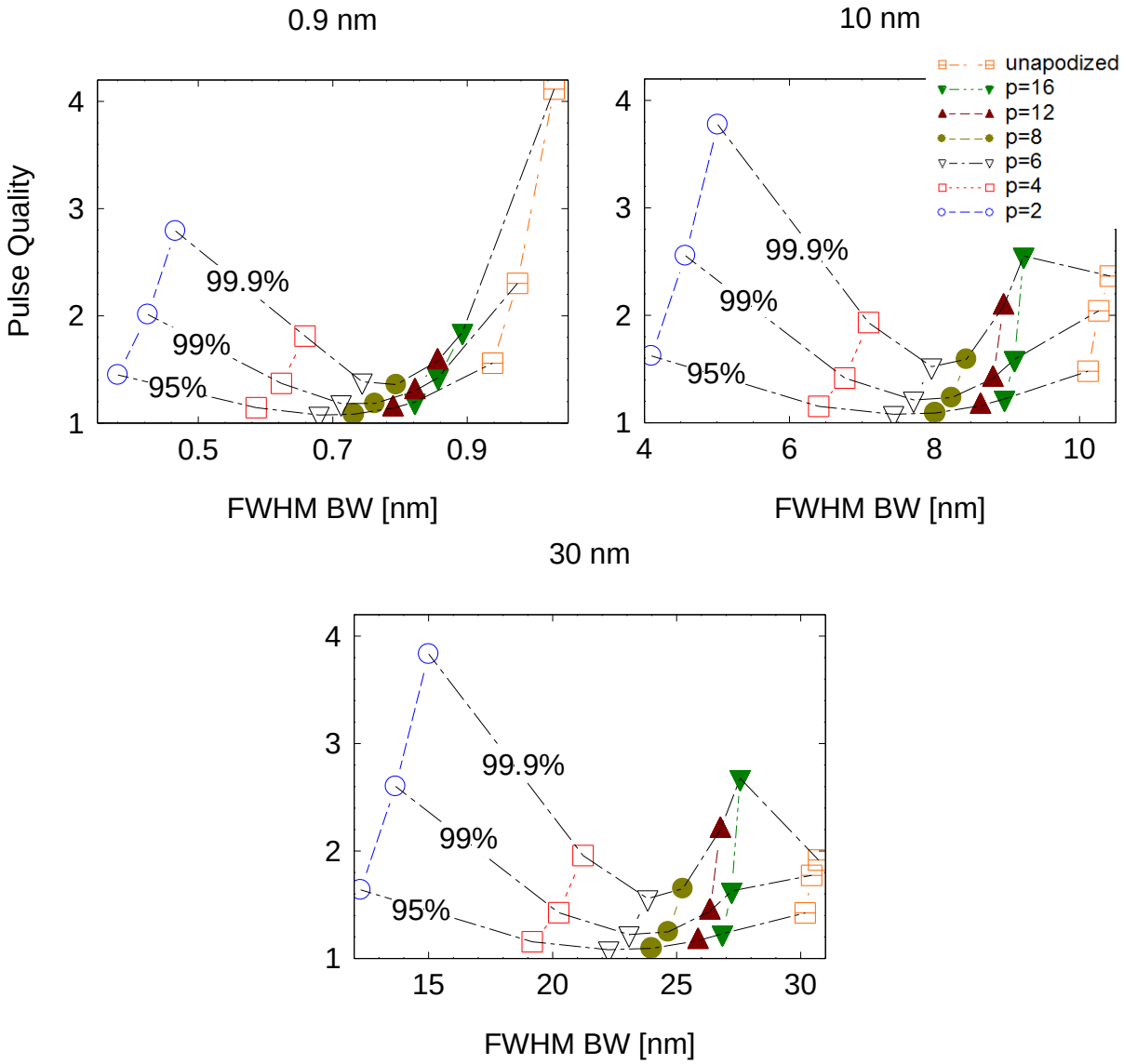

Figure 2.6 The quality of recompressed pulses degrades with reflectivity. The CVBG is 3 cm long, and the bandwidth of the CVBG is listed at the top of each plot. The order *p* of apodization is listed in the legend, which applies to all figures.

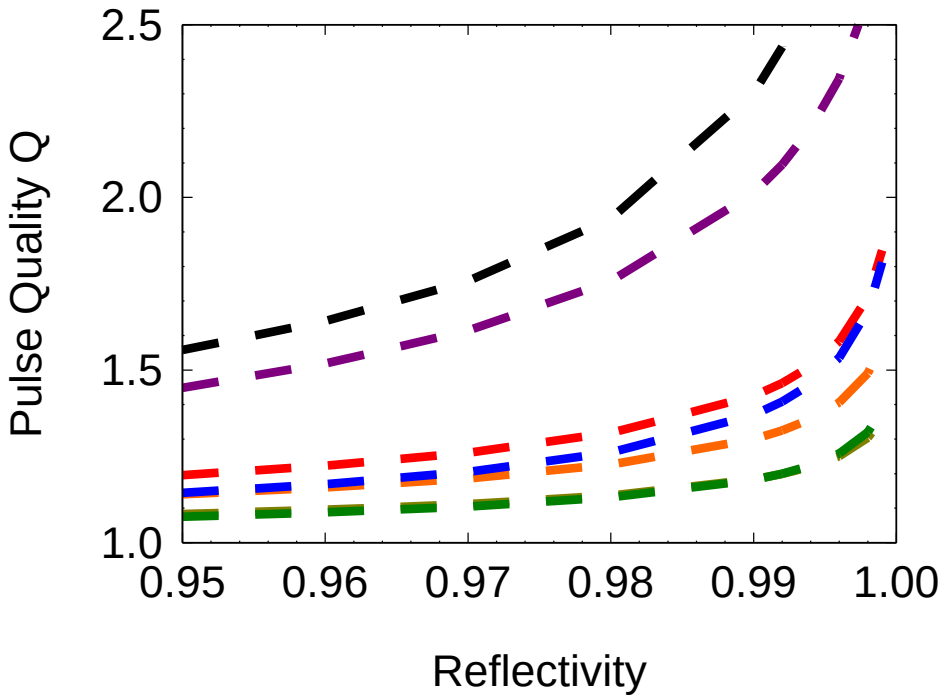

Figure 2.7 The quality of recompressed pulses degrades with reflectivity. The CBG is 3 cm long with a 0.9 nm bandwidth.

One interesting observation is that non-reciprocity of a CBG is completely determined by its length-bandwidth product. In other words, two different gratings with different lengths and bandwidths will produce exactly the same distortion if their length-bandwidth product is the same. This is illustrated in Figure 2.9. This allows us to universally plot the recompressed pulse quality Q as a function of this length-bandwidth product, as shown in Figure 2.9. This plot reveals that for the apodization factors in the middle range pulse quality Q is not much affected by grating length and bandwidth, but at the edges of this range (i.e. for unapodized and Gaussian-apodized profiles) it exhibits some distinct dependence on the CBG bandwidth and length.

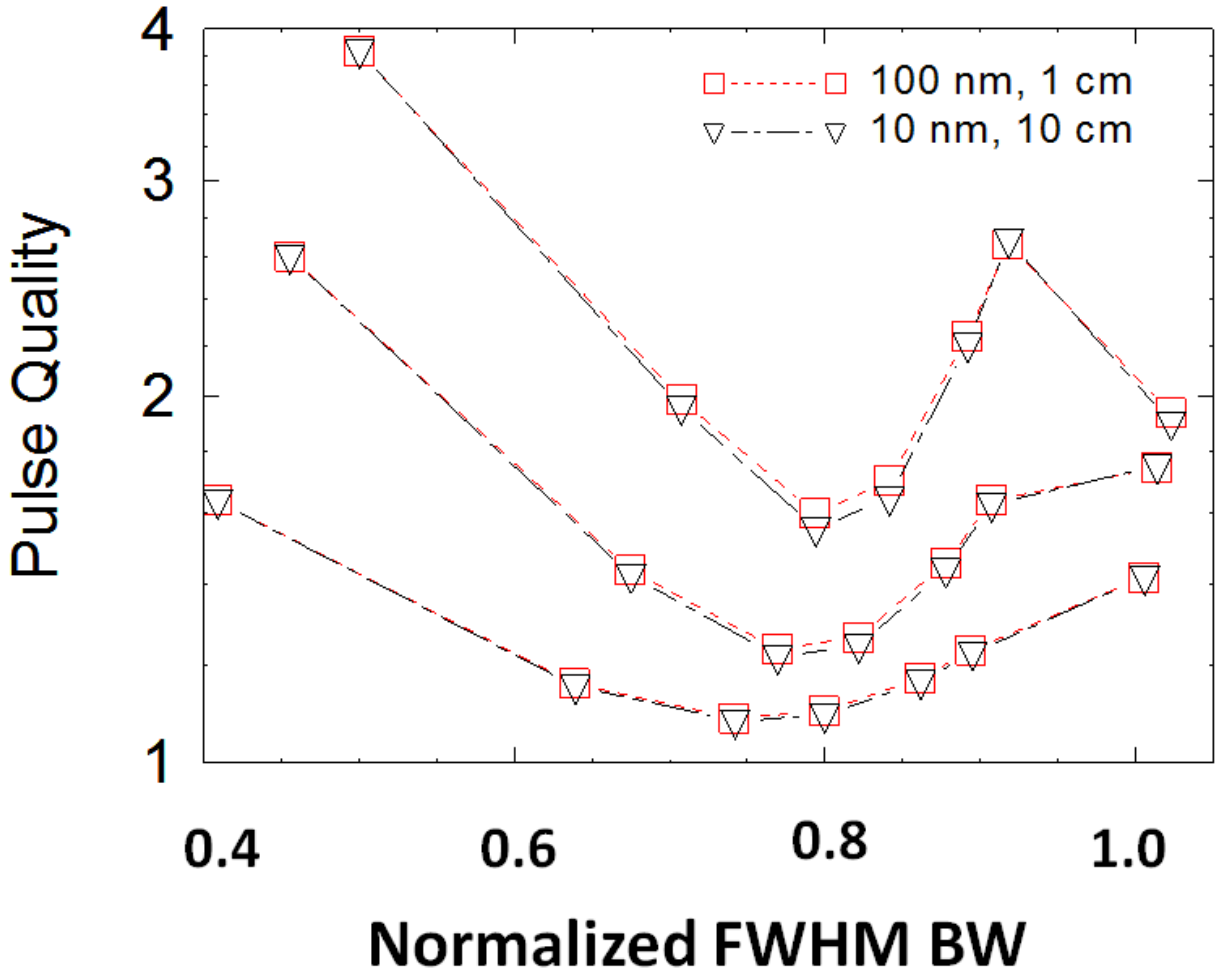

Figure 2.8 Performance of a CVBG can be analyzed using a length-bandwidth product.

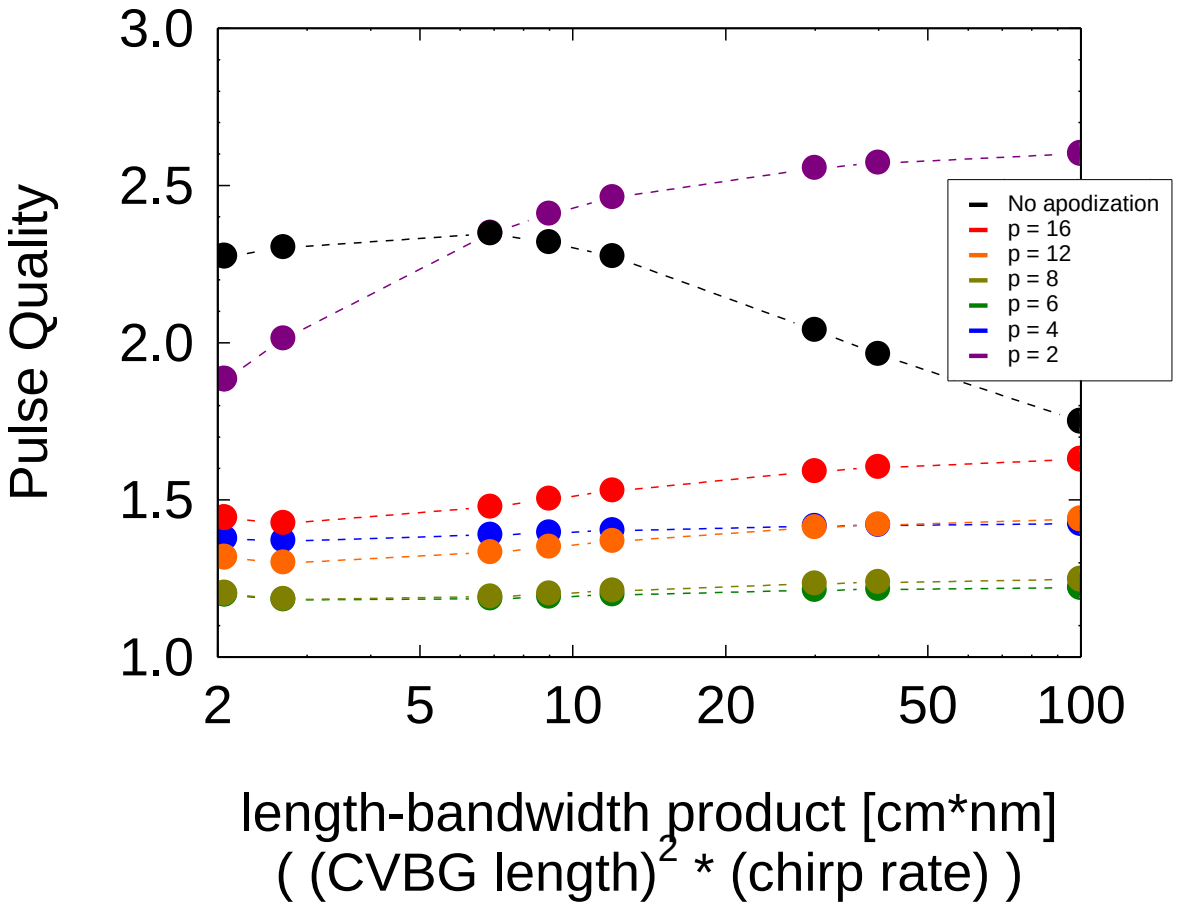

Figure 2.9 Pulse quality varies with the length-bandwidth product of a 99% reflective CBG.

2.4 Conclusion

We have shown that it is possible to increase practically useful CBG reflectivity from approximately 80% in an unapodized grating to approximately 95% (and higher) in a suitably apodized grating. This is much higher than typical compressor efficiencies achievable with diffraction-grating based systems.

2.5 References

1 V. G. Bespalov, A. A. Gorodetski, I. Yu. Denisyuk, S. A. Kozlov, V. N. Krylov, G. V. Lukomski, N. V. Petrov, and S. É. Putilin. "Methods of generating superbroadband terahertz pulses with femtosecond lasers." Journal of Optical Technology **75**(10), pp 636-642, October 2008.

2 U. Hinze, A. Egbert, and B. Chichkov. "Generation of picosecond hard-x-ray pulses in a femtosecond-laser-driven x-ray diode." Optics Letters **29**(17), pp 2079-2081, 2004.

3 M. Gower. "Industrial applications of laser micromachining." Optics Express **7**(2), pp 56-67, July 2000.

4 A. Galvanauskas. M. E. Fermann. "Optical pulse amplification using chirped Bragg gratings." U.S. Patent 5499134 A, issued August 24, 1994.

5 P. Tournois, P. Hartemann, "Bulk chirped Bragg reflectors for light pulse compression and expansion." Optics Communications **119**, pp 569-575, 1995.

6 M. Rever, G. Chang, V. Smirnov, E. Rotari, I. Cohanoshi, S. Mokhov, L. Glebov, A. Galvanauskas, "Temporal Reciprocity of Chirped Volume Bragg Grating Pulse Compressors," *Conference on Lasers and Electro-Optics 2010*, OSA Technical Digest (CD) (Optical Society of America, 2010), paper CThA3.

7 R. Kashyap, Fiber Bragg Gratings. 2nd ed. San Diego, CA. Academic Press, 2010, ch. 5 & 7.

8 K. O. Hill, "Aperiodic Distributed-Parameter Waveguides for Integrated Optics," Appl. Opt. **13**, 1853-1856, 1974.

9 M. Matsuhara and K. O. Hill, "Optical-Waveguide Band-Rejection Filters: Design," Appl. Opt. **13**, pp 2886-2888, 1974.

10 N. Matuschek, F. Kärtner, and U. Keller, "Exact Coupled-Mode Theories for Multilayer Interference Coatings with Arbitrary Strong Index Modulations." IEEE Journal of Quantum Electronics, **33**(3), pp 295-302, March 1997.

11 O.V. Belai, E.V. Podivilov, and D.A. Shapiro, "Group delay in Bragg grating with linear chirp." Optics Communications **266**, pp 512-520, 2006.

12 M. Sumetsky and B. Eggleton. "Theory of group delay ripple generated by chirped fiber gratings." Optics Express **10**(7), pp 332-340, 2002.

Chapter 3

Thermal Loading Effects on Chirped Volume Bragg Grating Stretcher/Compressor Systems

3.1 Introduction

Ultrafast high-power fiber chirped pulse amplification (CPA) lasers are promising for a wide range of applications including material processing and inspection, THz imaging, and EUV and X-ray generation. Fiber lasers are particularly attractive over conventional bulk solid-state lasers because they can be made compact by coiling the amplifiers, they are monolithic, and they can be spliced together, thereby removing the need to align components. Moreover, fiber lasers can produce diffraction-limited beams even at high power because of the lack of thermal aberration.

In order for a fiber-CPA system to reach its potential for compactness and robustness, the bulk diffraction grating stretcher and compressor systems currently in use need to be replaced. Chirped-volume-Bragg-gratings (CVBGs) are compact and robust devices that can be used to stretch and recompress pulses for CPA lasers and offer substantial benefits over their bulk diffraction grating alternatives. First and foremost, they are small; with only a few centimeters of length, a CVBG can stretch a transform-limited femtosecond or few-picosecond pulse to hundreds of picoseconds (the chirp rate is 100 ps/cm-length) and recompress the pulse back. This greatly reduces the overall size of a CPA system, and is essential for preserving the advantages of a fiber-laser system. Moreover, they are simple to use; all that must be done is to send a pulse

into one end of the grating, and a stretched or recompressed pulse will be reflected back, depending on the orientation of the CVBG. This makes them suitable for monolithic systems in which free-space components with complex alignment are unusable. Furthermore, these devices are polarization independent, and have been shown to withstand high average power and energy without damage because they are made of photo-thermo-refractive (PTR) glass.

Although CVBG stretchers and compressors are not presently limited by damage, what has remained unknown is how they perform when used in high average-power systems. Namely, the effects of thermal loading on the qualities of the reflected beam and recompressed pulse have not been explored. In this work, a CVBG-based fiber-CPA system is demonstrated and characterized up to an average power of 200 W uncompressed to reveal limitations on the spatial and temporal fidelity of the CVBG. The spatial fidelity of the CVBG is shown to be its limiting factor, for it can provide nearly diffraction-limited beam quality up to 100 W, and this power limitation is determined primarily by residual absorption in the CVBG. The temporal fidelity of the CVBG, however, is not limited to 200 W. The reason for these limits is well explained by the physics of thermal loading on the dielectric structure, and an understanding of this phenomenon allows us to identify paths toward increasing the power scalability of CVBGs.

3.2 200 W CVBG based Fiber CPA system

A CVBG-based FCPA setup is shown in Figure 3.1. It is an ytterbium (Yb) fiber-CPA system with which up to 200 W of average power incident and 130 W reflected (compressed) from a CVBG with pulse durations of ~350 fs has been demonstrated. The system is seeded with a Nd:Glass oscillator generating 180 fs pulses at a repetition rate of 72 MHz with a central wavelength of 1064 nm. The pulses are sent into the broadband, 3 cm long CVBG stretcher, after

which they have an edge-to-edge pulse duration of ~300 ps. Next, a negative dispersion device is used to cancel out the residual fiber dispersion, since the stretcher and compressor are intrinsically reciprocal. In this experiment, a miniature 2-grating Treacy compressor is used. However, this is merely for experimental convenience. In a production system, an appropriate length of anomalous dispersion fiber, such as properly engineered photonic band-gap fiber, would be used in order to avoid using free-space components.

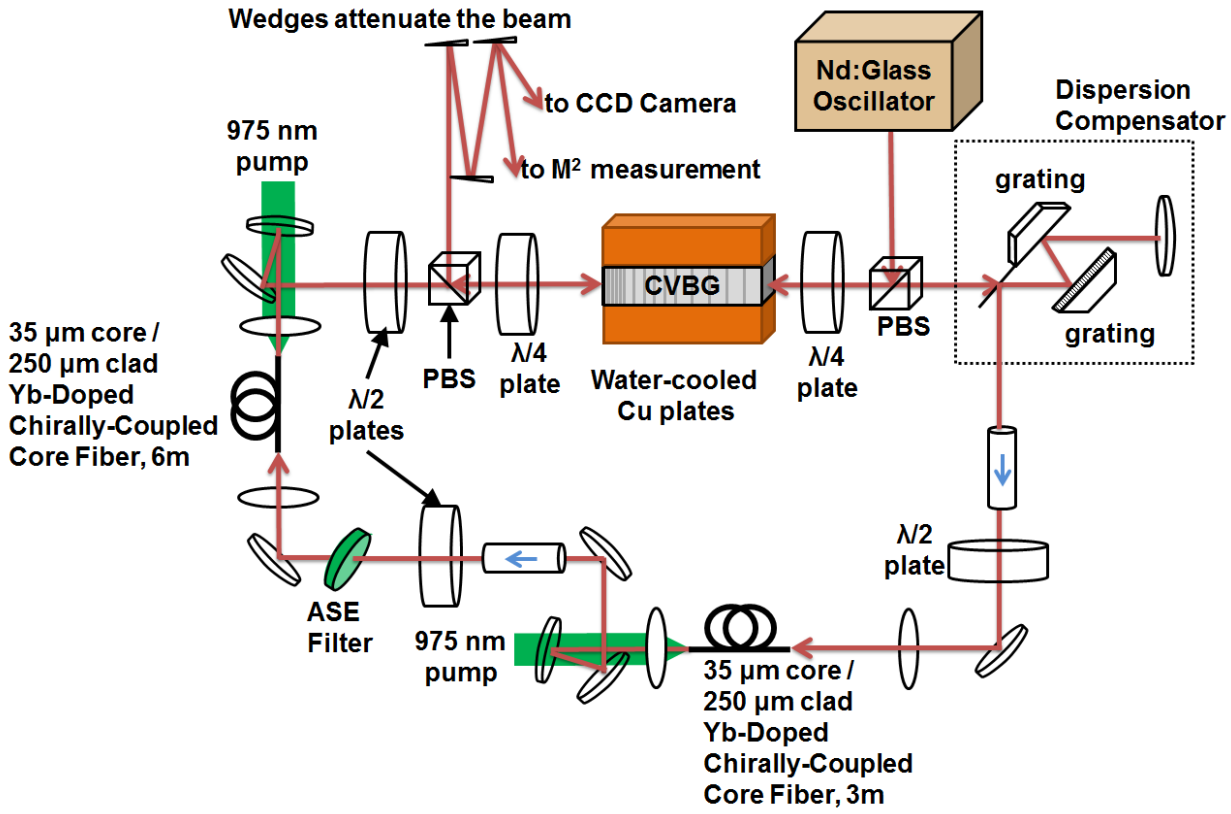

Figure 3.1 Experimental setup of high-power CVBG/CCC based fiber-CPA laser.

A series of amplifiers increased the average power to 200 W. All amplifiers were diode-pumped at 975 nm and operated in a counter-propagating configuration. The first amplifier was a 3 m long, 35 µm core/250 µm cladding chirally-coupled core (CCC) amplifier fiber that brought the power to 2 W. An amplified spontaneous emission (ASE) filter suppressed ASE from this

amplifier. The final amplifier was a 6 m long, 35 μm core/250 μm cladding CCC fiber amplifier, which boosted the power to its final level. The amplifier fibers were robustly single-mode and required only simple alignment to maximize the power throughput.

The same CVBG used to stretch the pulse was used for compression to ensure exact reciprocity of the stretcher and compressor. The beam was sent in at a small angle (~3°) to prevent crosstalk and to avoid the need for isolators or other transmission components that could burn at high power. Though the compressed beam was at a small angle, it roughly overlapped the stretched beam so that they would experience the same thermal load. A pair of water-cooled copper plates further reduced the thermal effects.

To isolate the spatial fidelity of the CVBG from that of the output beam, the output of the second amplifier was fixed at 200 W. This ensured that there was no change in the spatial quality of the output beam caused by varying thermal loading conditions on the amplifier. The power load on the CVBG was controlled with polarization components inserted after the second amplifier; a half-wave plate controlled the polarization of the amplified pulses and a polarizing beam splitter controlled the incident power, and hence the thermal load, onto the CVBG.

3.3 Volumetric temperature distribution in thermally-loaded high power CVBGs

The spatial and temporal fidelity of a CVBG depend on the thermal loading conditions in the CVBG, which occur because of residual absorption in the substrate at the operation wavelengths. An incident high-power beam thus deposits a fraction of its power into the substrate, yielding a volumetric temperature distribution in the grating. This distribution, which depends on the average power, spatial profile, and spectrum of the incident beam, then

determines distortions imprinted onto the temporal and spatial profiles of the reflected compressed-signal beam.

The dominant thermal-loading effect that primarily defines both the spatial and temporal fidelity of the CVBG is associated with the longitudinal optical power distribution in a chirped grating. This power distribution is caused by the grating's spectral reflection characteristics, which is to say that the local Bragg condition will distribute the power longitudinally depending on the relation of the input spectrum to the reflectivity spectrum (Figure 3.2).

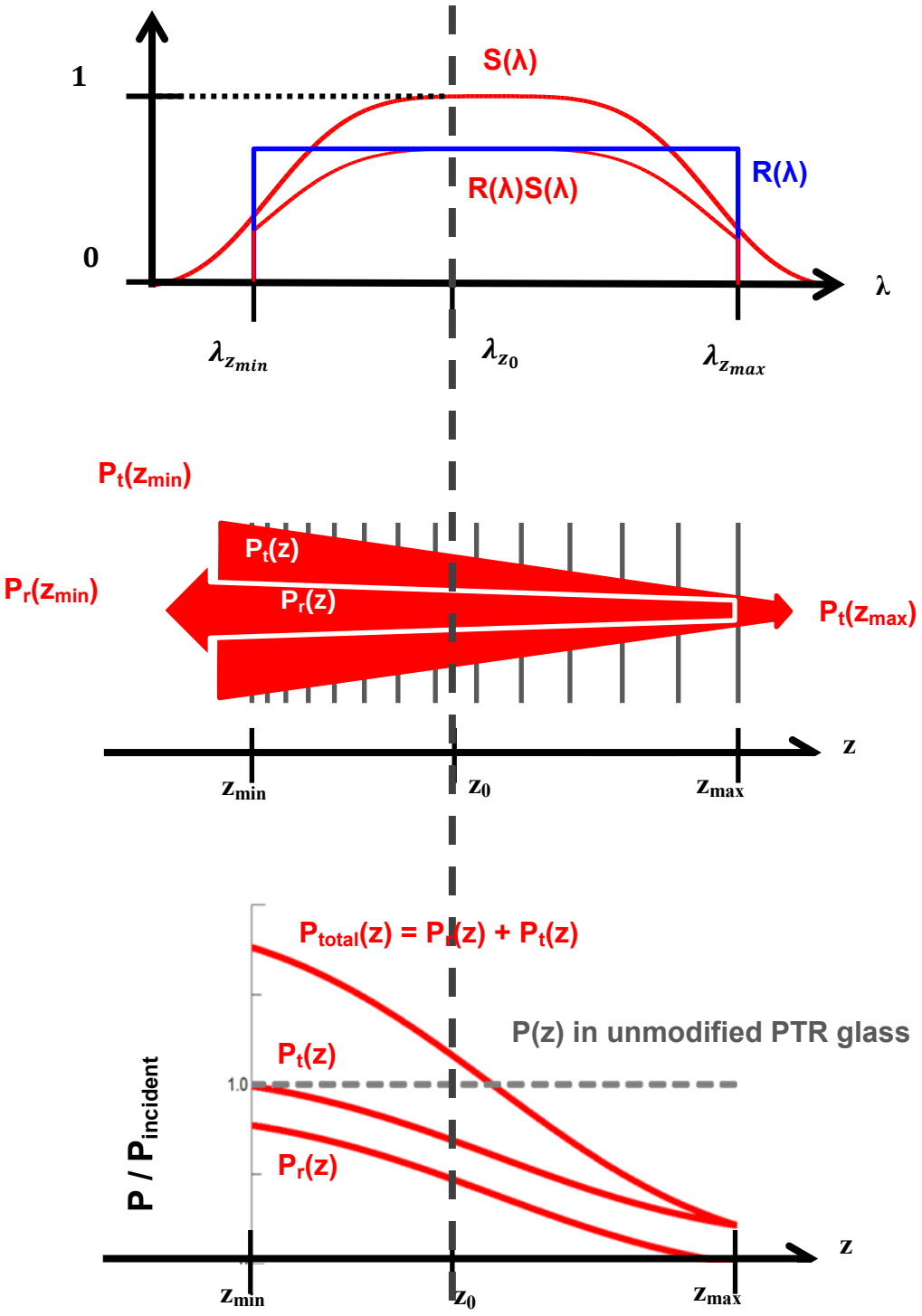

Figure 3.2 Illustrated dependence of optical power distribution along CVBG on relation of reflectivity spectrum to incident spectrum

This power distribution can be computed analytically at each point as the sum of the power reflected after the point with the power transmitted to the point (see Figure 3.2). The reflected power is the sum of the reflections for all wavelengths between the wavelength reflected at the point of interest and the end of the reflectivity spectrum of the CVBG, as described in Eq 3.1 below. Here, $S_\lambda(\lambda)$ is the input pulse spectrum, α is the material absorption, $R(\lambda)$ is the grating reflectivity, and L is the grating length.

$$P_r(z_0) = \int_{\lambda_{z_0}}^{\lambda_{z_{max}}} e^{-\alpha(2z_{refl}-z)} S_\lambda(\lambda) R(\lambda) d\lambda \tag{3.1}$$

$$\text{with } z_{refl} = \frac{\lambda - \lambda_{z_{min}}}{\lambda_{z_{max}} - \lambda_{z_{min}}} L \tag{3.2}$$

The transmitted power is the sum of the power transmitted from all wavelengths in the reflectivity spectrum before that point and the power of all wavelengths after that point, as described below:

$$P_t(z_0) = \int_{-\infty}^{\lambda_{z_0}} e^{-\alpha z} S_\lambda(\lambda)(1 - R(\lambda)) d\lambda + \int_{\lambda_{z_0}}^{\infty} e^{-\alpha z} S_\lambda(\lambda) d\lambda \tag{3.3}$$

The power distribution in the CVBG is the sum of these two terms, as given in Equation 3.4:

$$P_{total}(z_0) =$$

$$\int_{\lambda_{z_0}}^{\lambda_{z_{max}}} e^{-\alpha(2z_{refl}-z)} S_\lambda(\lambda) R(\lambda) d\lambda + \int_{-\infty}^{\lambda_{z_0}} e^{-\alpha z} S_\lambda(\lambda)(1 - R(\lambda)) d\lambda + \int_{\lambda_{z_0}}^{\infty} e^{-\alpha z} S_\lambda(\lambda) d\lambda \tag{3.4}$$

For comparison, and to show that the longitudinal power distribution is caused by the grating effect rather than by absorption, which is 10^{-3} cm^{-1} or less for the current generation of gratings, Figure 3.3 shows a sample calculation for both the above equation and the power distribution due only to exponential absorption in a blank slab of PTR glass (with 10^{-3} cm^{-1} absorption). As can be seen, the grating effect is dominant.

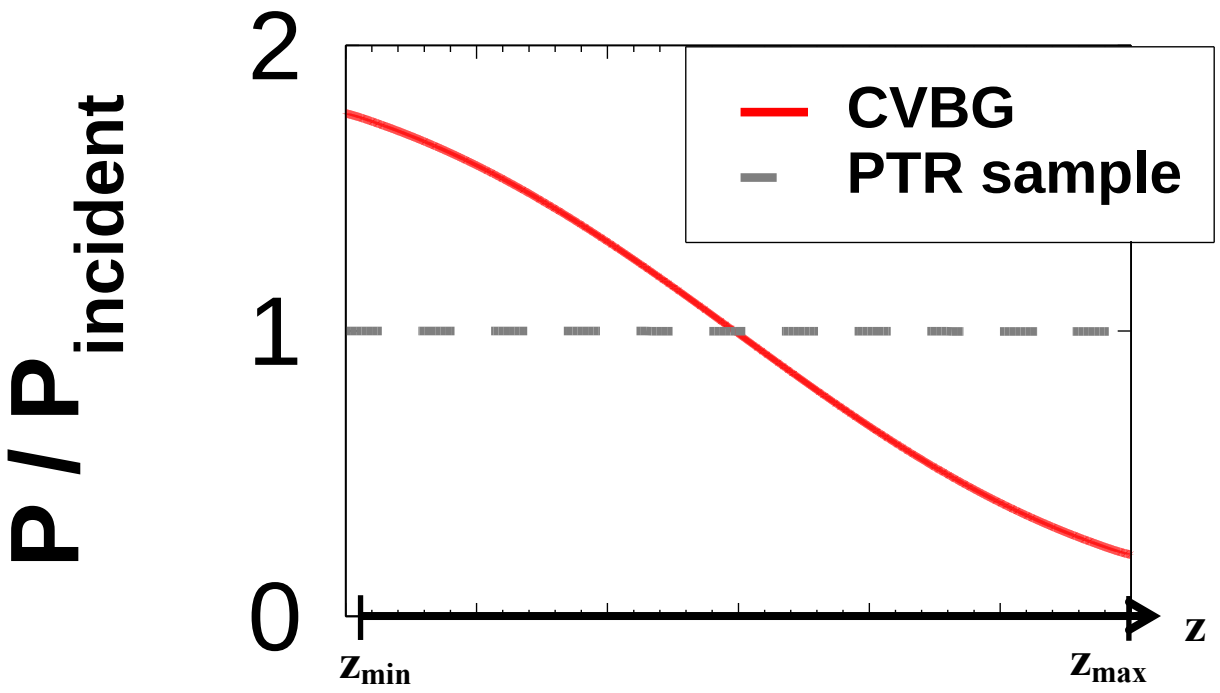

Figure 3.3 Comparison of optical power distribution along CVBG and PTR glass samples for normalized incident power

Given the longitudinal power distribution, the 3D temperature in the CVBG can be computed using finite-element analysis (FEA) to solve the steady-state heat transfer equation:

$$\nabla \cdot (-k\nabla \mathrm{T}) = Q \tag{3.5}$$

$$\text{with } Q(r,z) = P(z) * \alpha \exp\{-2r^2/w_0^2\} \tag{3.6}$$

The numerical model used for the calculations in this work is based on COMSOL Multiphysics. Using numerical methods allows for generalizing the model to include cooling conditions as well as spatial overlapping of the stretched and compressed beams (so they encounter the same thermal distortion) in the gratings, whether complete, partial, or not at all due to angle and displacement. This made it possible to simulate accurately the experimental conditions.

The boundary conditions are set according to the cooling system in the experimental setup, with all four sides of the CVBG placed in direct contact with a water-cooled copper mount. The water flows through 4 mm wide pipes in the mount at a constant temperature of 8°C and at a rate of 0.3 gal/min. The remaining surfaces were taken to be insulated. Though convection cooling from the air can be taken into account, it is found to be negligible and therefore needlessly increases computation time. The heat source Q in Eq. 3.6 is obtained by multiplying the power at position z from Eq. 3.4 by the absorption coefficient and distributing the power over the Gaussian beam area. Figure 3.4 shows a simulated volumetric temperature distribution from the model for a CVBG corresponding to the specifications of the CVBG presented experimentally in this study: the sample has the dimensions 5 mm X 6 mm X 27 mm as well as a 10 nm bandwidth centered at 1064 nm, and an absorption coefficient of $6.9*10^{-4}$ cm^{-1}. The remaining material properties are taken to be the same as those of silica glass, which is a stock material in COMSOL, because the material properties of PTR glass are very similar to those of silica glass [4]. The input pulse is a 200 W Gaussian beam with a 2 mm ($1/e^2$) diameter and a Gaussian spectrum with a 10 nm FWHM so that the profile of the input fills the reflectivity spectrum of the CVBG.

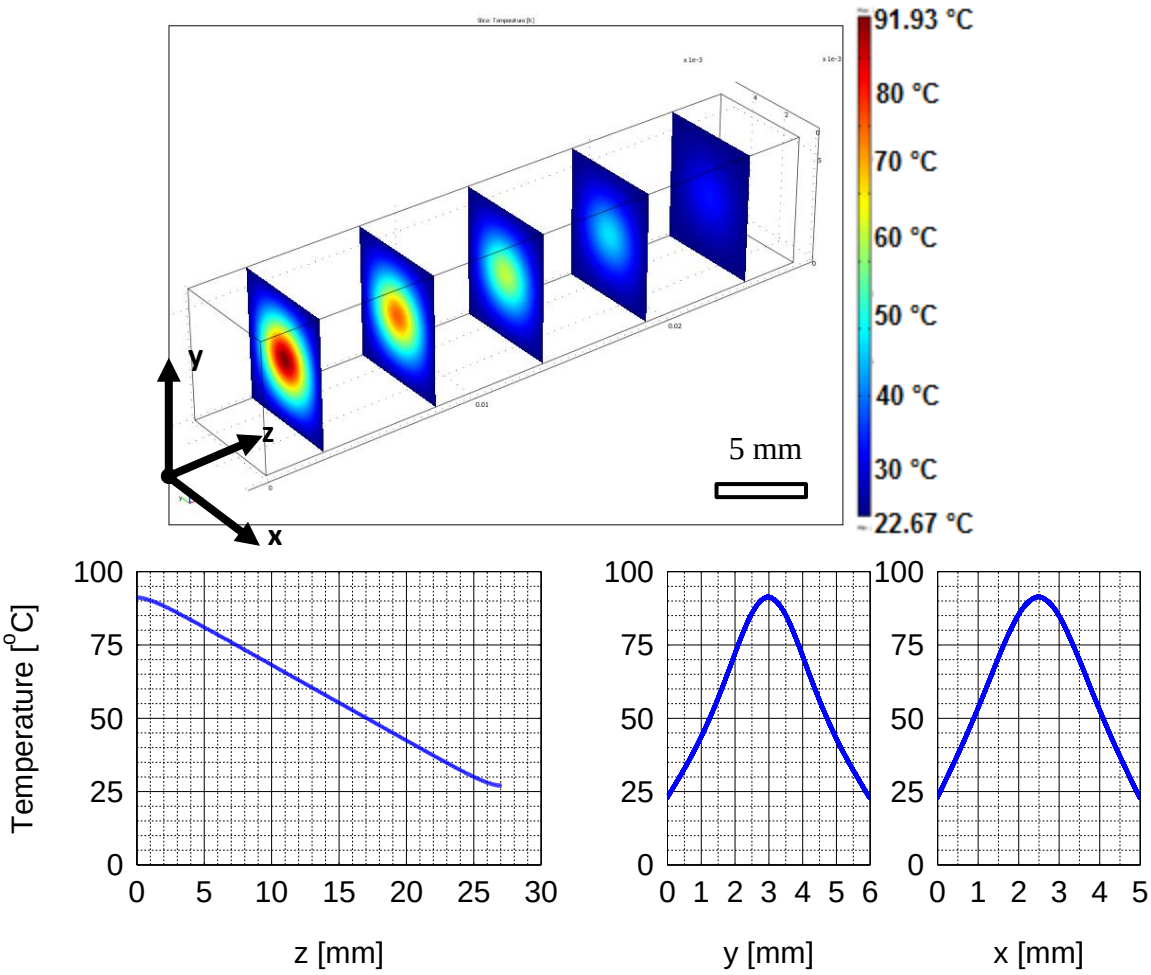

Figure 3.4 Numerically simulated 3D temperature distribution in CVBG. An example of a numerically simulated 3D temperature distribution in a CVBG. In this example, a 2 mm diameter beam of 200 W average power enters the grating in the center of the left facet. The input signal spectrum fills the CVBG spectrum. The temperature of the water cooling the heat-sink in this calculation is assumed to be 8°C, and the simulated temperature of the heat-sink itself is 23°C. Beam incidence and reflection are along the z-axis. A color-coded bar on the right indicates the temperature in °C, and longitudinal and transverse distributions of thermal load on CVBG are plotted beneath. The longitudinal distribution was taken along the center of the CVBG, and the transverse distributions were taken along the front of the CVBG.

This thermal load was found to be separable into longitudinal and transverse components, as shown in Figure 3.4. One can see from this figure that the longitudinal temperature distribution is consistent with the analytical result of the longitudinal optical power distribution from Eq. 3.1, shown in Figure 3.3, when the input spectrum of the pulse and reflectivity spectrum of the CVBG are matched. The transverse thermal distribution was determined by the transverse shape of the input beam. In this case, the Gaussian beam produced nearly Gaussian

thermal distributions laterally, each with the same width but a different peak temperature at every cross-section of the sample.

The transverse thermal distribution would change if the size of the input beam were changed. Figure 3.5 shows the distribution of the thermal load across the front of the CVBG for input beams that are 1 mm and 2 mm wide.

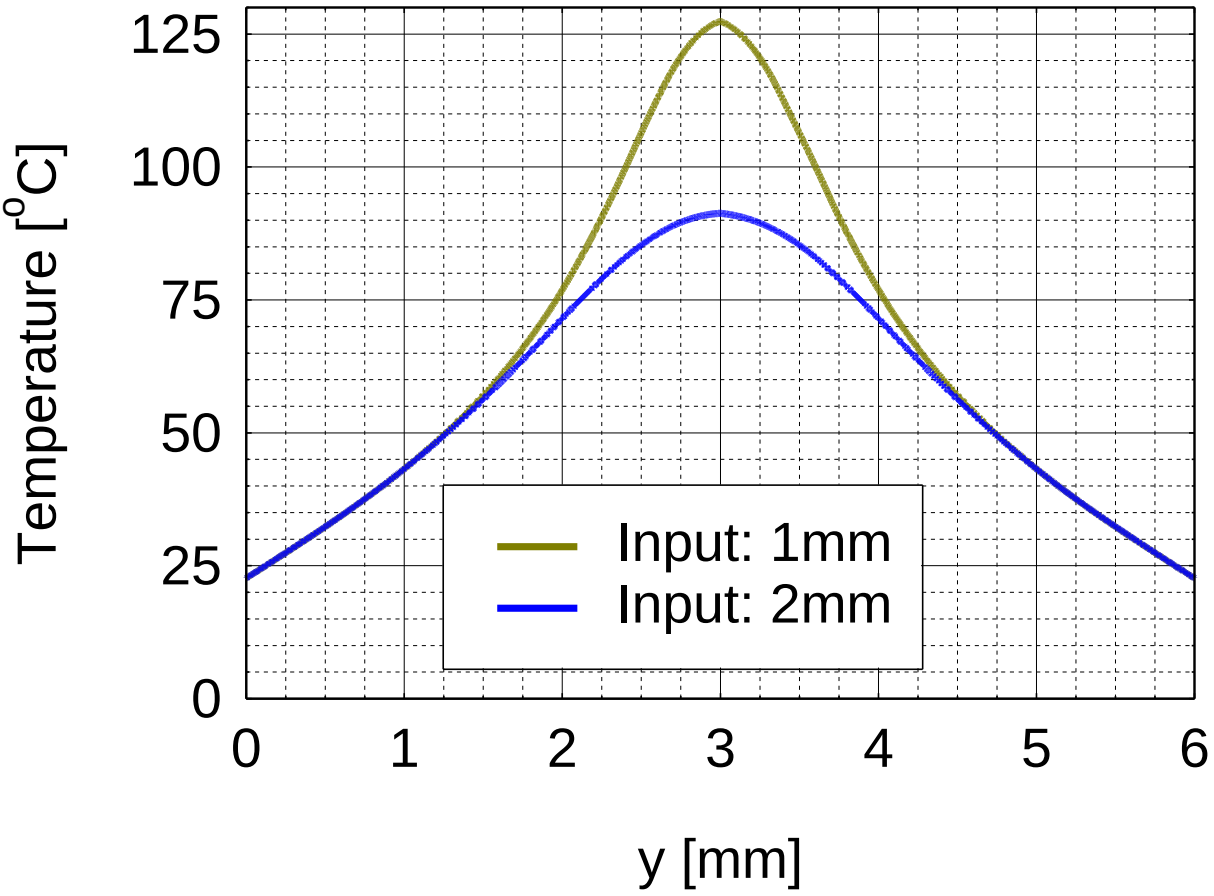

Figure 3.5 Size of incident beam determined transverse temperature distribution across the front of the CVBG. Transverse thermal distribution across the front of the CVBG for input beams of 1 mm and 2 mm width.

We compared numerical predictions with actual CVBG measurements, performed with a thermal-imaging camera. A thermal image of the CVBG at 150 W of input power is shown in Figure 3.6. The peak temperature in the center of the front of the CVBG was measured to be

77.5°C and was simulated to be 71.3°C. The simulated value is higher than would be seen for a fixed temperature of the mount because the mount heats slightly when a thermal load is applied to the CVBG; this is also seen experimentally. The difference between the measured and simulated temperatures is partially attributable to an increase in temperature of the water flowing though the mount, which was simulated at a fixed temperature of 8°C, and it is partially attributable to numerical error in the experimental measurement.

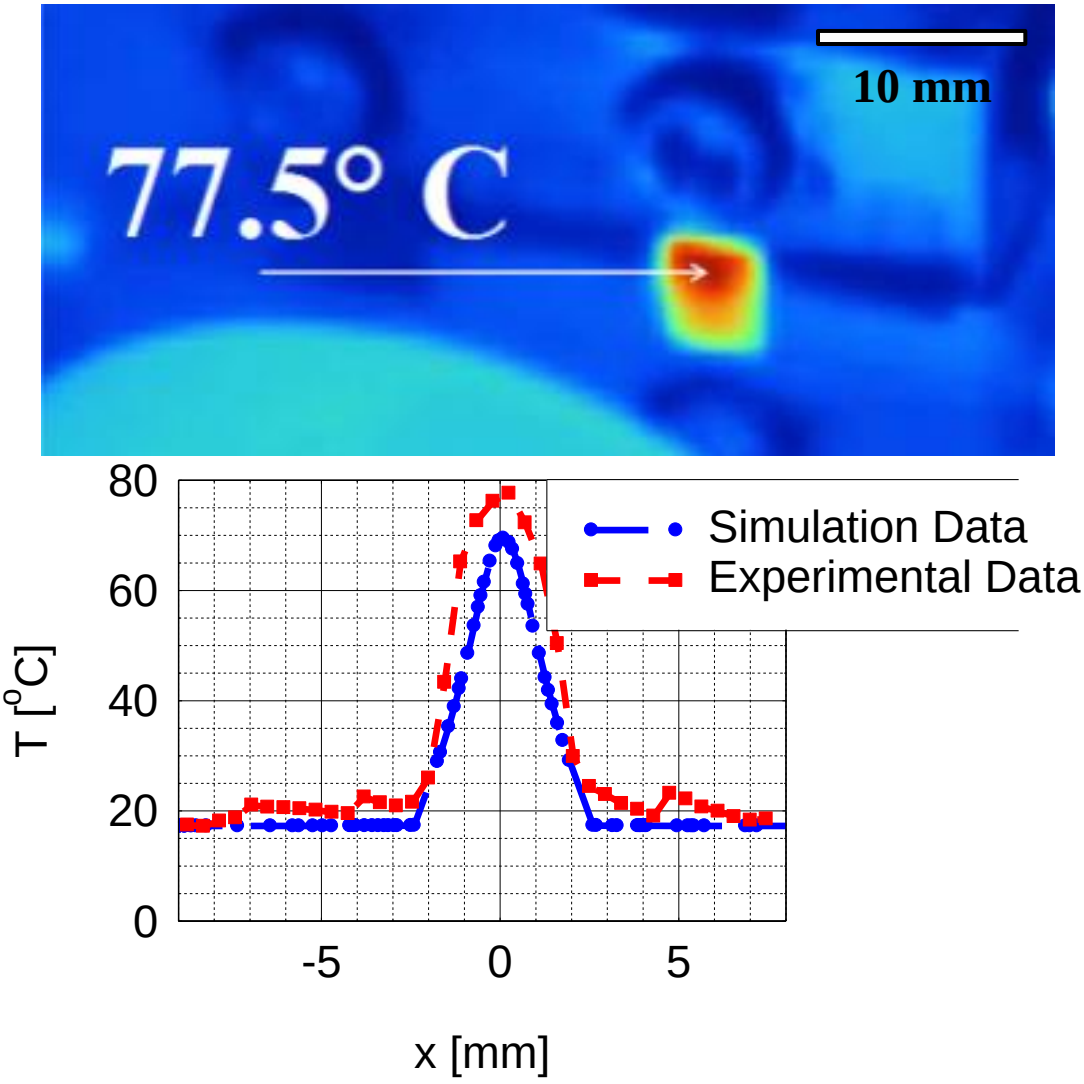

Figure 3.6 Thermal image of temperature distribution at the input 5 mm X 6 mm facet of the CVBG with 150 W input beam, whose spectrum fills the CVBG spectrum. Scale bar is 10 mm.

The measured dependence of peak temperature at the center of the input facet of the CVBG as a function of incident power is shown in Figure 3.7. The slope of this curve is 0.3527°C/W, which is close to the numerically predicted slope of 0.3463°C/W. The difference between these slopes indicates the margin of error in the experimental and simulated results.

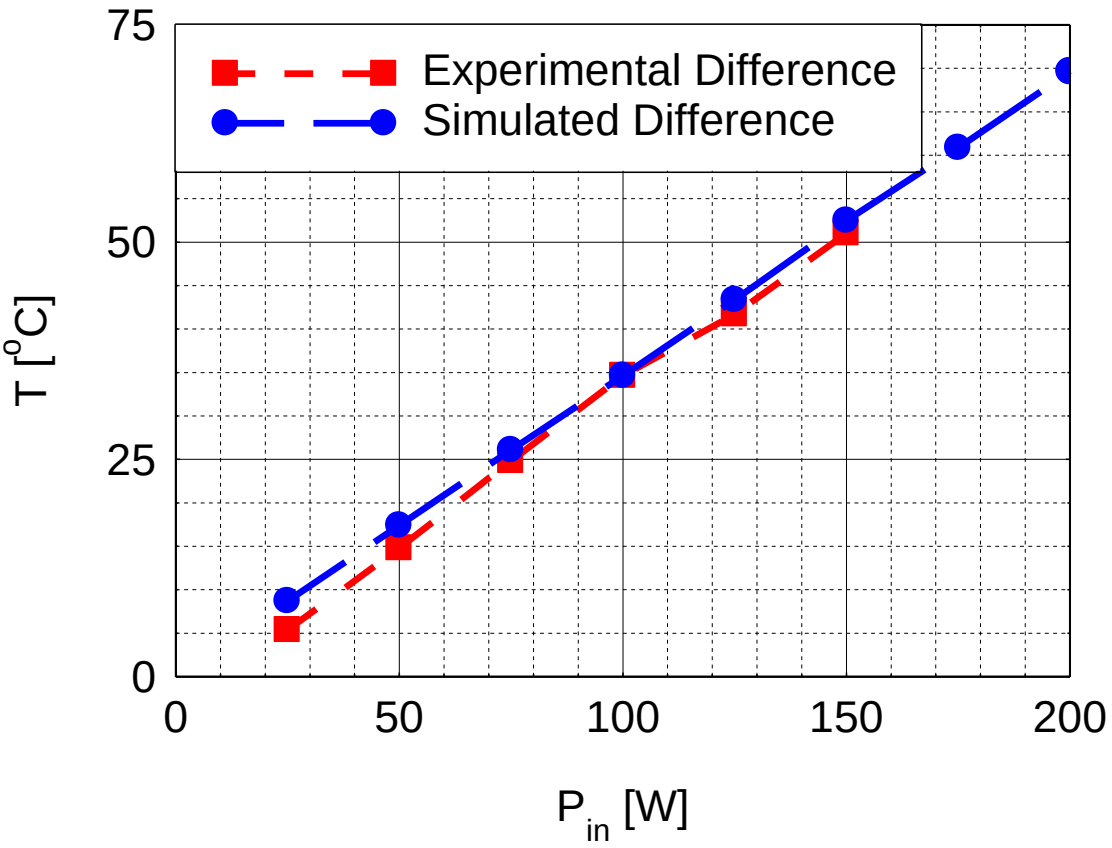

Figure 3.7 A comparison of simulated peak temperature at the entrance facet of the CVBG to experimental peak temperature as functions of incident power.

This temperature distribution translates into a corresponding modulation of refractive index in the CVBG via the thermo-optic effect, which is $5*10^{-7}$/K in PTR glass [4]. Based on the thermal load calculated earlier in this section, the corresponding modulation of refractive index is the product of the localized thermal load with the thermo-optic coefficient, as shown in Figure 3.8.

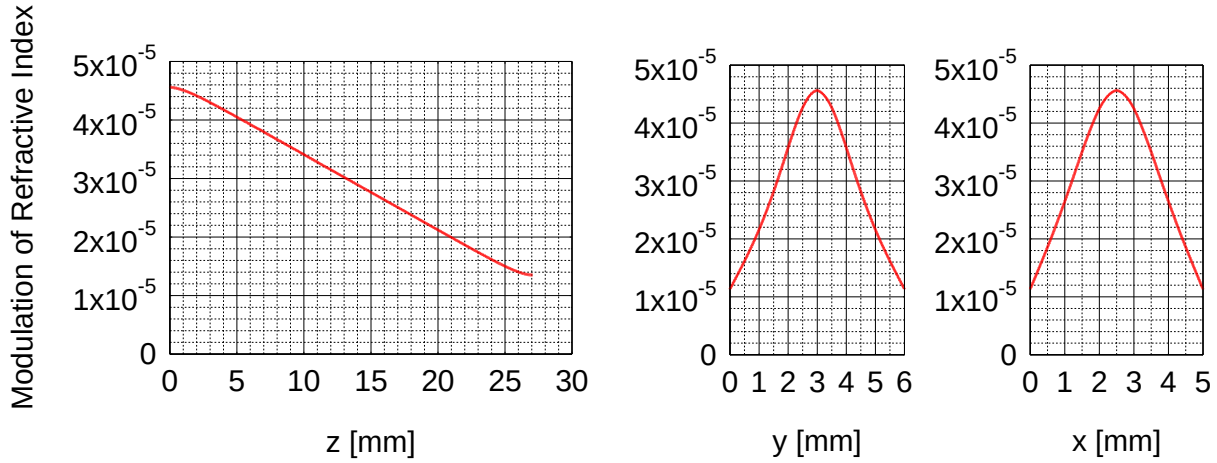

Figure 3.8 Modulation of refractive index in CVBG caused by distribution of thermal load as presented in Figure 3.4.

This non-uniform modulation of refractive index affects both the spatial and temporal fidelity of the CVBG, as described in detail in the subsequent sections. The spatial fidelity of the CVBG is affected both by the transverse and longitudinal profiles of the refractive index; the transverse profile yields a relatively weak gradient-index (GRIN) lens, and the longitudinal profile determines the varying focusing power along the CVBG. The relative focusing power of the GRIN lenses is illustrated in Figure 3.9. The chirped nature of the CVBG provides for each spectral component to reflect from a unique point in the CVBG, thus experiencing a unique focusing power that results in spatial distortion of the beam.

The temporal fidelity of the CVBG is affected primarily by the longitudinal profile, which modulates the dispersion relation in the CVBG by changing the local Bragg condition. This can be largely negated, however, by overlapping the stretched and recompressed signal beams in the CVBG.

3.4 CVBG spatial fidelity at high average powers

The volumetric modulation of refractive index determines the spatial fidelity of the CVBG. The transverse profile yields a gradient-index (GRIN) lens with relatively weak focal power, and the longitudinal profile determines the focal power as a function of position along the CVBG. The relative focal power of the GRIN lenses is illustrated in Figure 3.9.

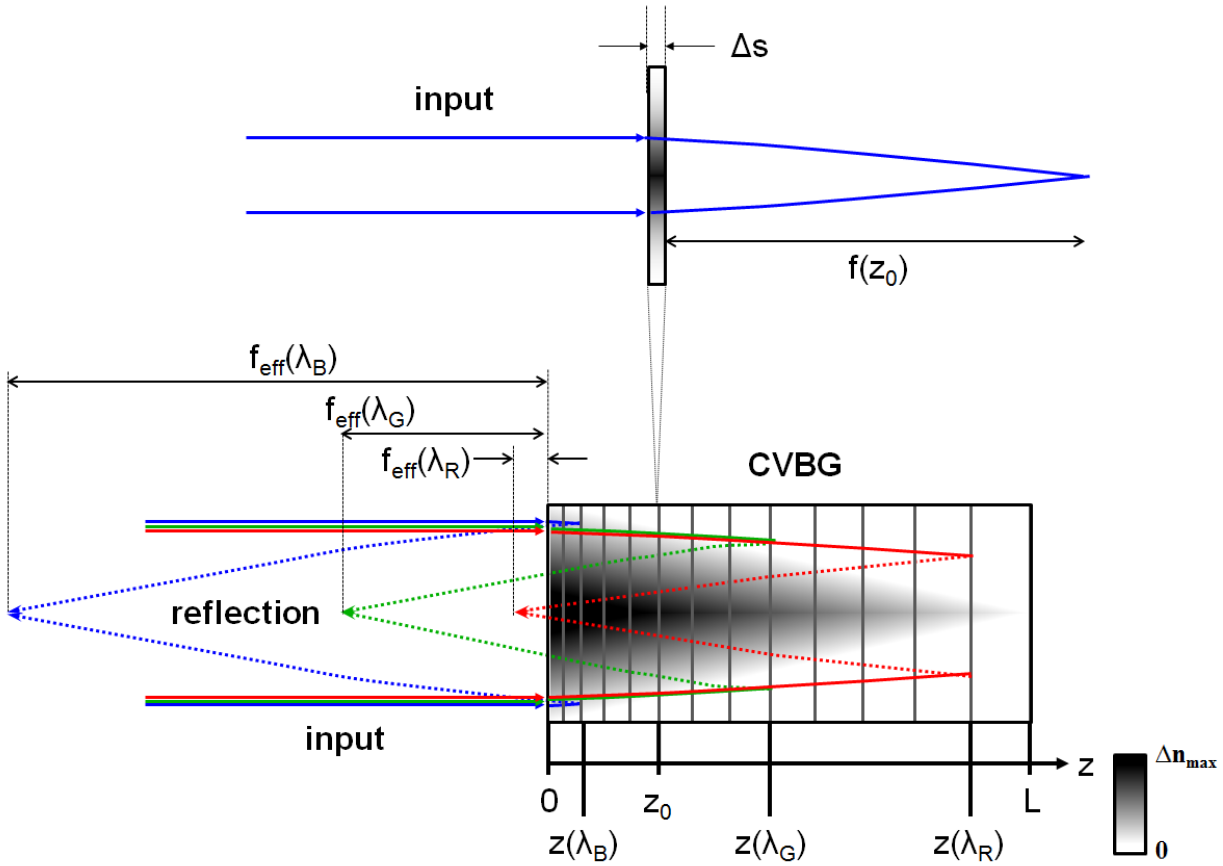

Figure 3.9 Thermally induced modulation of refractive index in CVBG, both longitudinally and laterally, yields a GRIN lens that causes the reflected beam to focus. The focal length f_{eff} is wavelength dependent because each wavelength λ reflects from a different point z(λ). Wavelengths reflected from the incident end of the CVBG (blue, λ_B) focus far away from the CVBG, whereas wavelengths reflected at the far end of the CVBG (red, λ_R) focus close to the CVBG.

To determine the effective focal length of the CVBG for each wavelength in the reflected spectrum, the general formula for a GRIN lens can be applied to the gradient index determined by the profile of the incident beam at each point along the CVBG. Note that this assumes that the

refractive index does not vary longitudinally, which is valid for a sufficiently small Δs, and that $|\nabla^2 n|$ is constant laterally, which is valid for a parabolic approximation of the refractive index profile ($n(r) = n_{max}\text{-}ar^2$).

$$f = \frac{r}{\tan(\sin^{-1}(n_0 * \sin(\tan^{-1}(\Delta s * |\nabla n|/n_0))))} \quad \rightarrow \quad f(z_0) = \frac{1}{2a\Delta s}, \text{ where } a = \frac{2\alpha P(z)}{k w_0^2}\frac{dn}{dT} \quad (3.7)$$

From this, the effective focal length of the CVBG can be calculated using the formula for a series of lenses back-to-back. The integral is doubled because each wavelength travels to its point of reflection and back to the input facet.

$$\frac{1}{f_{eff}(\lambda)} = 2 * \int_0^{z(\lambda)} \frac{1}{f(z)} dz \quad \rightarrow \quad f_{eff}(\lambda) = \frac{k\pi w_0^2}{2\alpha\frac{dn}{dT}\int_0^{z(\lambda)} P(z)dz} \quad (3.8)$$

In this equation, f_{eff} is the overall effective focal length of the CVBG, w_0 is the $1/e^2$ radius of the incident beam, α is the absorption coefficient, P(z) is the longitudinal power distribution, dn/dT is the thermo-optic coefficient, k is the coefficient of heat conduction of the material, and z(λ) is the point in the CVBG at which λ is reflected. Figure 3.10 shows the dependence of effective focal length and beam divergence on wavelength and input power. The variation in focal length and beam divergence induces a longitudinal spatial chirp, essentially chromatic aberration, in the reflected compressed-signal beam that degrades the spatial fidelity of the CVBG with increasing input power.

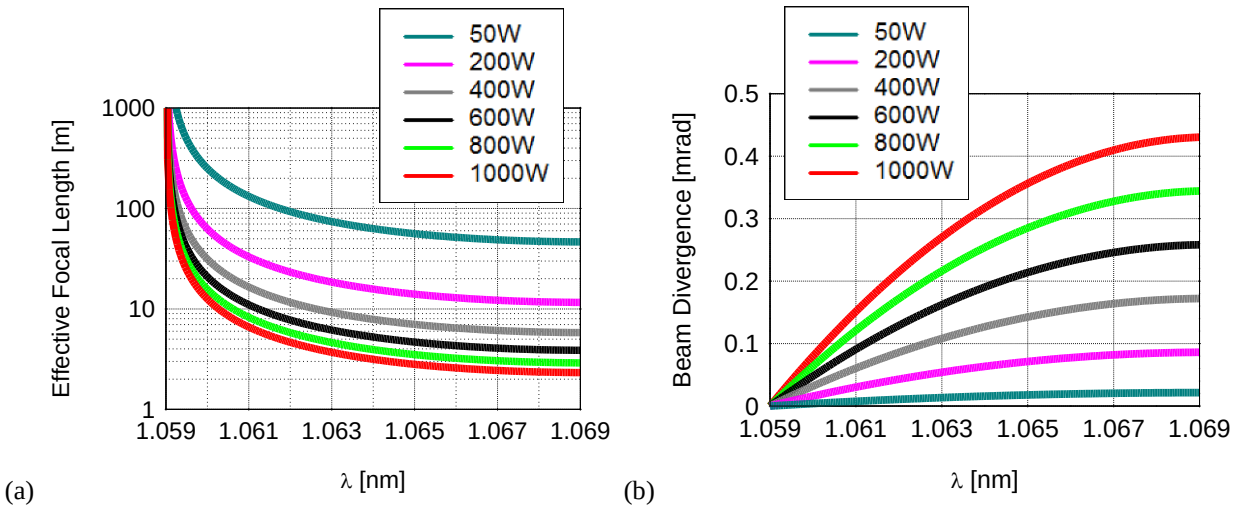

Figure 3.10 Spectrally dependent focal length (and beam divergence) of a thermally-loaded CVBG. (a) Calculated dependence of focal length vs. wavelength due to the thermally-induced longitudinally-varying GRIN lens in CVBG at different incident power levels. High-power beam is incident on blue end (1.059 μm) of grating. (b) Beam divergence introduced by the same phenomenon. Distortions arise because the convergence of the reflection is wavelength-dependent.

The relation of this wavelength-dependent focal length to the overall beam quality is given in Eq. 3.9 below, where we determine the $1/e^2$ radius of the beam by integrating the beam propagation across the spectrum [9], where $f_{eff}(\lambda)$ is the effective focal length of the CVBG at λ and $z_R(\lambda)$ is the Rayleigh range. The M^2 of the beam is the square of the ratio of the focused spot size to the input spot size. Simulation results in Figure 3.11 show that the spatial quality of the CVBG degrades rather linearly across much of the power range.

$$\frac{1}{e^2}\int_{-BW/CR}^{BW/CR}\frac{1}{1+\left(\frac{f_{eff}(\lambda)}{z_R(\lambda)}\right)^2}ds=\int_{-BW/CR}^{BW/CR}\frac{e^{\frac{-(w/w_0(\lambda))^2}{(1+f_{eff}(\lambda)^2/z_R^2(\lambda))}}}{1+\left(\frac{f_{eff}(\lambda)}{z_R(\lambda)}\right)^2}ds \tag{3.9}$$

$$\text{with } w_0(\lambda)=\frac{w_{in}f_{eff}(\lambda)}{(f_{eff}(\lambda)+z_{R,in})} \text{ and } z_R(\lambda)=\frac{f_{eff}(\lambda)^2 z_{R,in}}{(f_{eff}(\lambda)+z_{R,in})^2} \tag{3.10}$$

Figure 3.11 Calculated M^2 vs. input power for 2.7 cm long and 10 nm bandwidth CVBG.

To determine the effect of thermal loading on the spatial fidelity of the CVBG, we used an incident beam that was relatively free of spatial distortion. At 200 W, we measured the M^2 of the incident beam to be 1.1 in both directions, as shown in Figure 3.12.

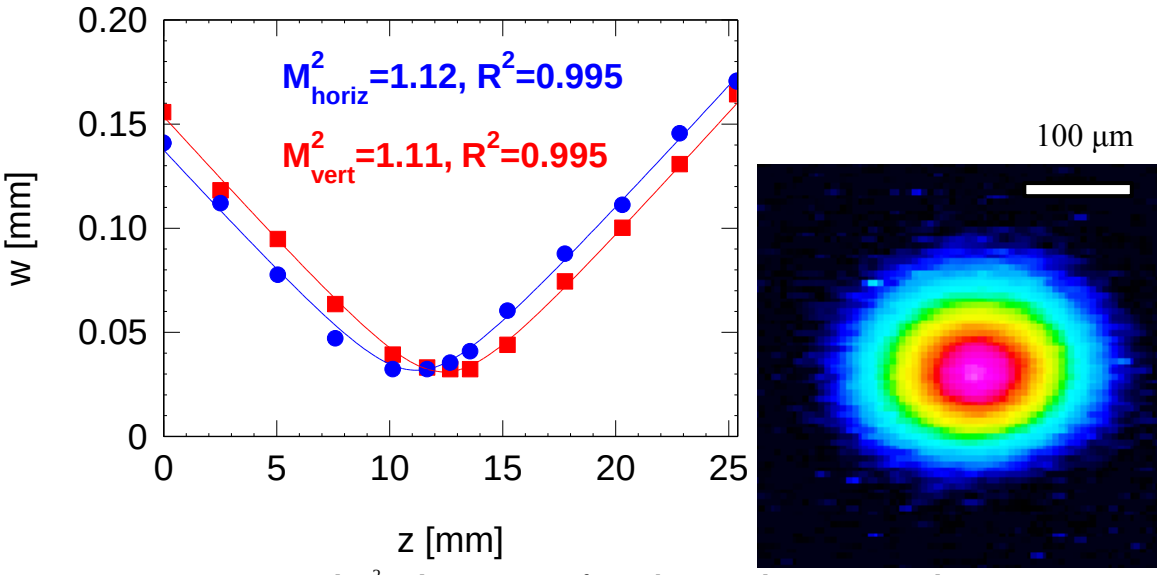

Figure 3.12 Measured M^2 and CCD image of input beam used in experimental setup

Experimental results show degradation of beam quality at incident powers much lower than predicted by this model. Figure 3.13 shows near-field images of the reflected beam for increasing incident power, and it demonstrates a visual degradation of the spatial beam fidelity gradually with increasing incident power up to 200 W. Because we maintain a constant power output from the fiber amplifier system, this degradation of the beam depends only on the thermal load of the CVBG. We include the corresponding M^2 values for this beam degradation and compare them to our calculations (Figure 3.14).

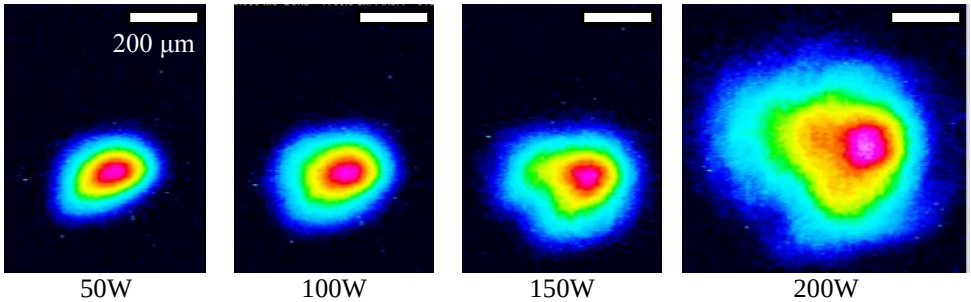

Figure 3.13 Experimental reflected beam near-field images at different powers incident into the CVBG. Gradual beam degradation with increasing power is seen here. Scale bar for all images is 200 µm.

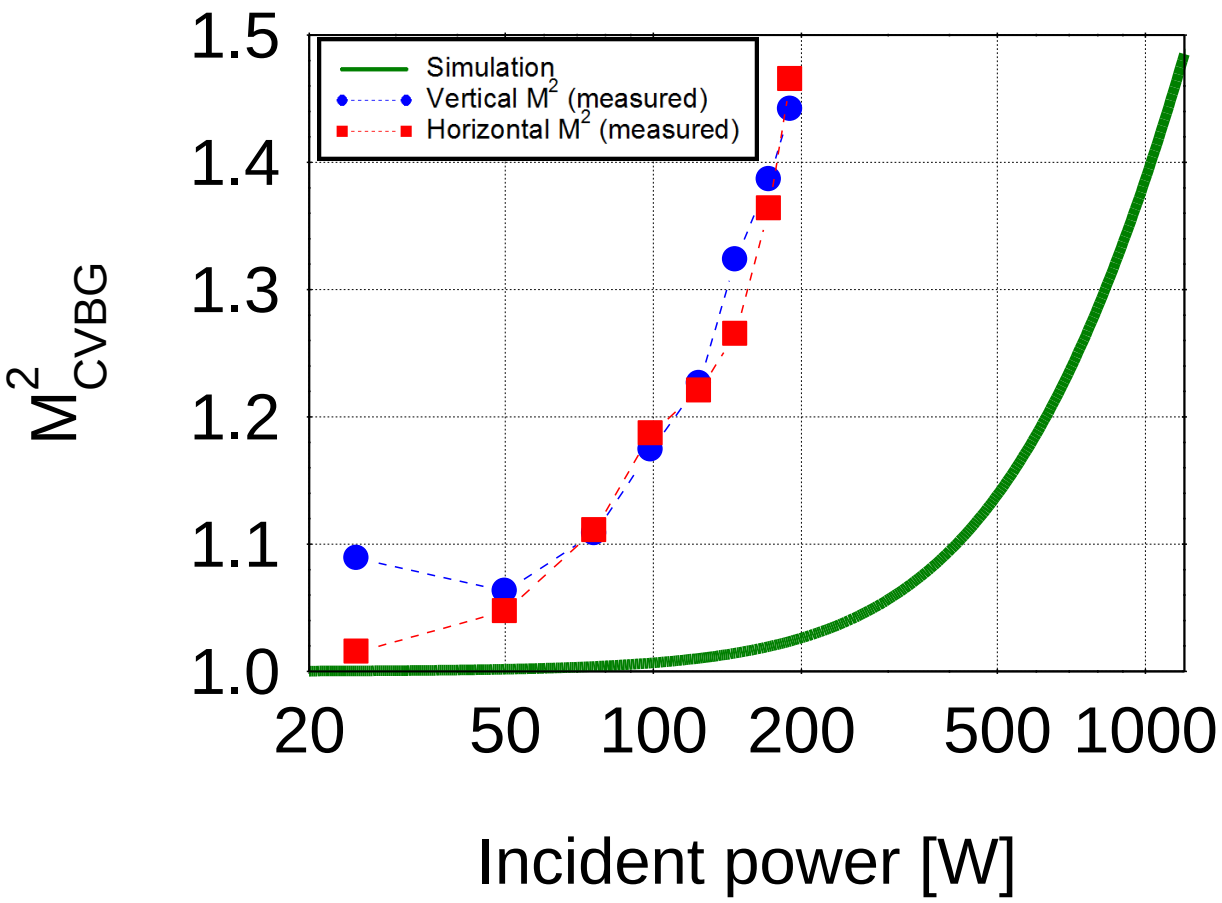

Figure 3.14 Measured and calculated M^2 vs. input power for 2.7 cm long, 10 nm bandwidth CVBG. Blue dots represent the measured vertical M^2, red dots represent the measured horizontal M^2, and the green curve represents the simulated M^2 values.

The discrepancy between the experimental and simulated results comes from the tendency of the CVBG to bend under a thermal load. While the reason for this bending is a topic of ongoing research, the mechanics to control it require that the water-cooled copper plates in which it is mounted (Figure 3.15a) provide sufficient force on all sides to compensate for the thermally-induced bending. When the CVBG is freely mounted, this bending dominates the performance of the CVBG. Figure 3.15b compares the M^2 values of reflected beams from the CVBG as measured above with the M^2 values of reflected beams from a freely mounted CVBG.

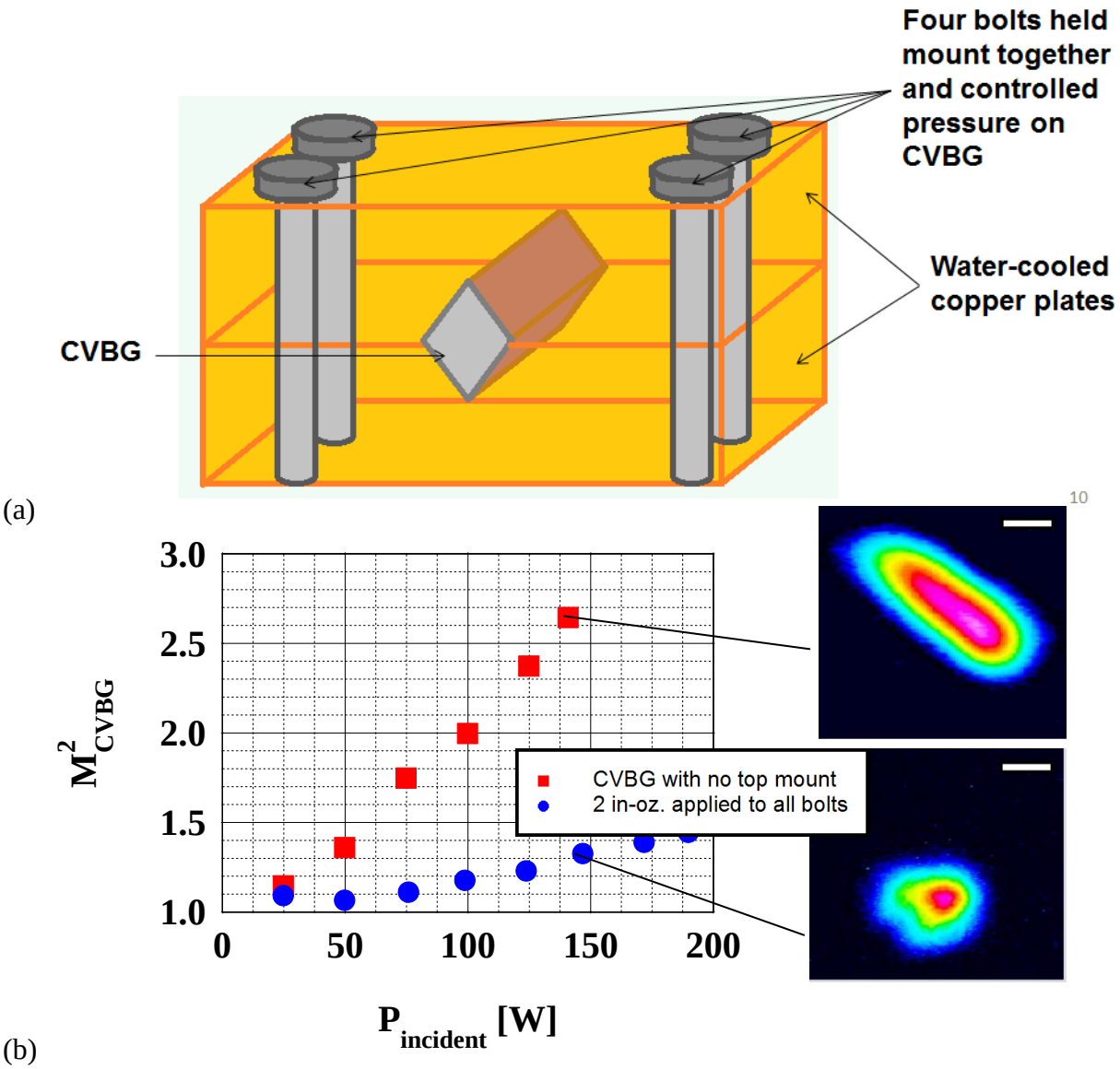

Figure 3.15 The CVBG bends under a thermal load unless the mounting configuration suppresses the bending. (a) The copper cooling mount for the CVBG (illustrated with CVBG in middle) needs to provide sufficient pressure on all sides of the CVBG to suppress thermally induced beam distortions. Pressure is controlled by applying torque to the bolts in the mount. Low torque (2 in.-oz.) is needed to suppress thermally induced bending of the CVBG, which is evident when the mount applies no pressure (e.g. the top mount makes no contact with the CVBG). (b) Measured and calculated M^2 vs. input power for CVBG. Red dots are the measured M^2 for a CVBG when the top block of the cooling mount makes no contact with the CVBG, which can then bend freely with thermal load. Blue dots are the measured M^2 for the same CVBG when a small torque (2 in.-oz.) is applied to each bolt in the copper cooling mount to suppress thermally-induced bending of the CVBG. Scale bars are 200 μm.

With the CVBG mounted with no top plate, it bends under a thermal load and the reflected beam exhibits spatial chirp. As shown in Figure 3.16, where the CVBG rests on a

copper mount with no pressure applied by the mount to suppress thermally-induced bending, spatial chirp is evident in the reflected beam for an incident power of 20 W.

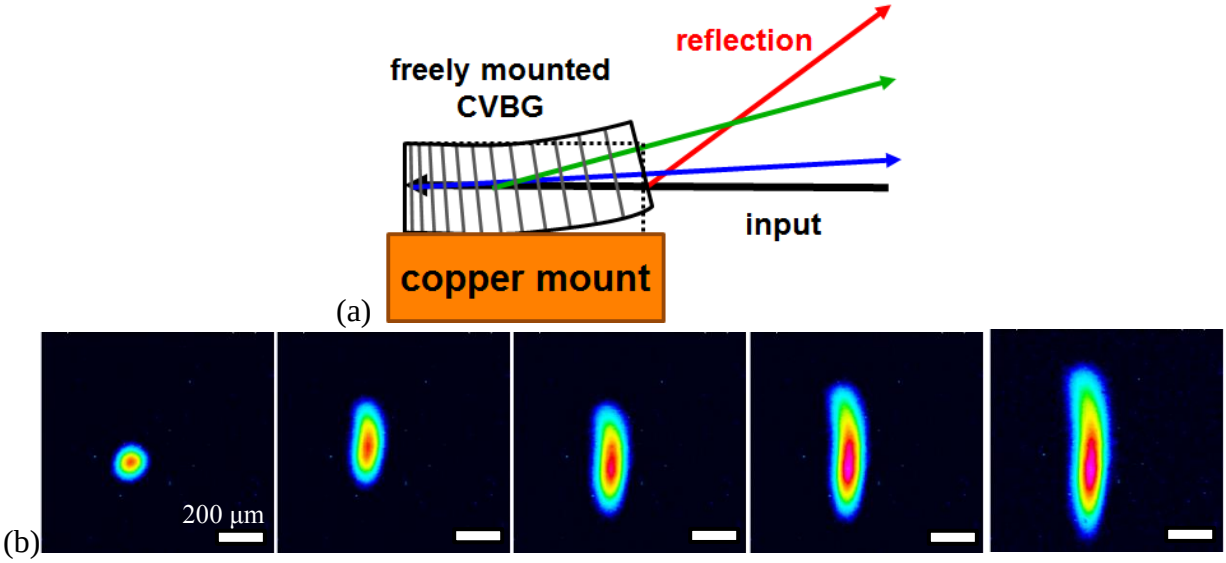

Figure 3.16 Beam distortion is evident in images of beam reflected from a CVBG that has no top mount to suppress thermally induced bending. (a) With the CVBG mounted freely, it bends under a thermal load, and the compressed pulses experience spatial chirp. (b) CCD images of reflected beam near-field images at different powers incident into the CVBG (10 W to 50 W) resting on a copper plate. Rapid beam degradation with increasing power is apparent here. Scale bar is 200 µm for all images.

We note that the CVBG bent in only one direction for such a mounting configuration. The copper mount underneath the CVBG acts as a heat-sink, inducing a thermal gradient that resulted in spatial chirp in the reflected beam. To test this idea, we rotated the CVBG 90° and measured the spatial chirp of the reflection CVBG for an incident power of 50 W (Figure 3.17). In this configuration, spatial chirp is evident in two directions, which implies that the spatial chirp is the result of both the thermal gradient as well as a thermally activated internal stress field, which we believe was residual from the writing process of the CVBG.

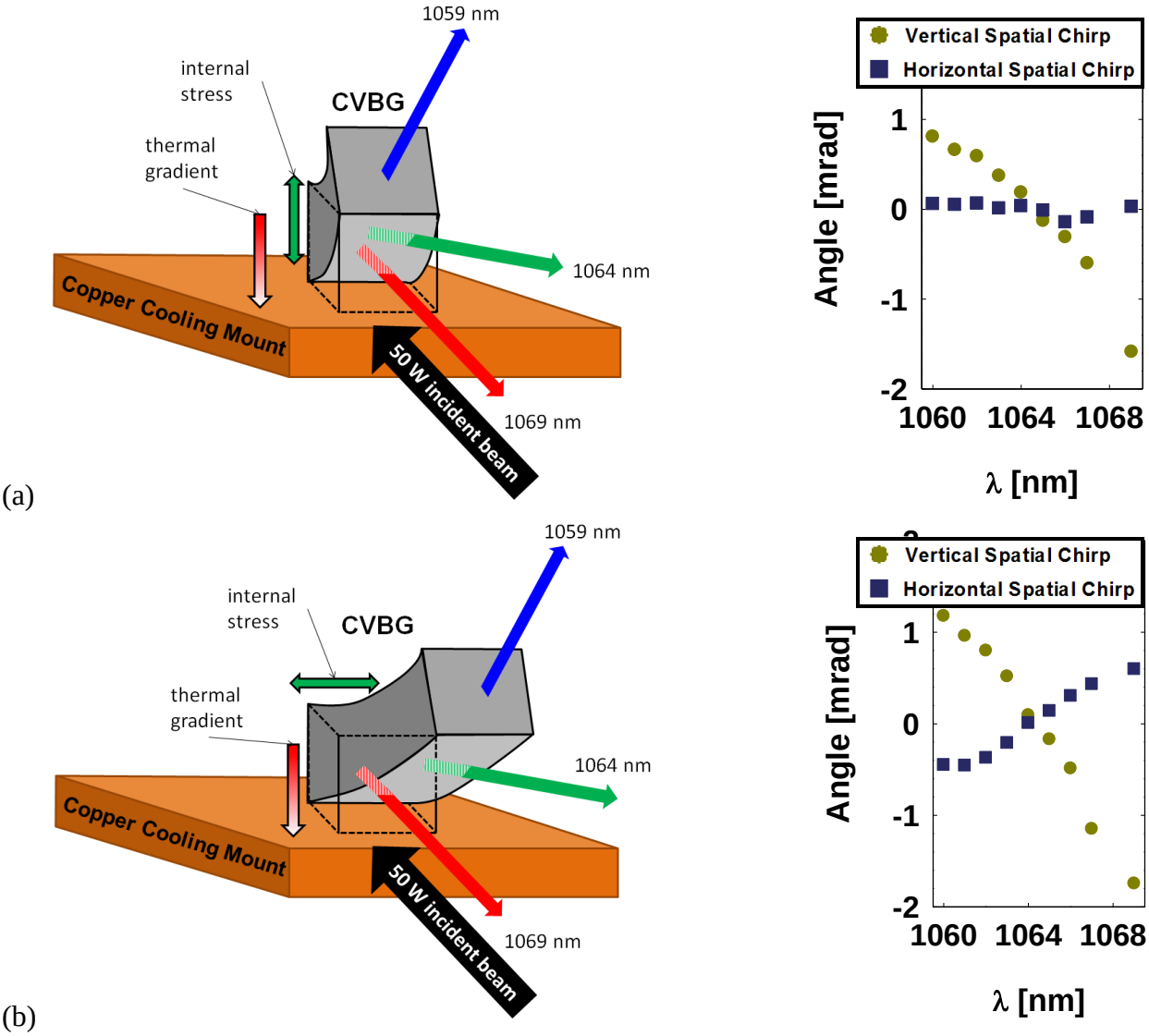

Figure 3.17 Spatial chirp of a CVBG with 50 W incident power and mounted on a copper plate. The bending of the CVBG is exaggerated for emphasis. (a) With the CVBG mounted upright, the reflection has 2.39 mrad of spatial chirp in one direction. Both a thermal gradient and a thermally activated internal stress field contribute to the spatial chirp. (b) With the CVBG mounted at a 90° angle, the reflection has 1.05 mrad of spatial chirp horizontally, where only the internal stress field contributes to the spatial chirp. Simultaneously, the reflection has 2.92 mrad spatial chirp vertically, which arises from only the thermal gradient. This indicates how each force affects spatial chirp. Because the spatial chirp in (a) was closer to the difference of the two measurements in (b) rather than to the sum of the measurements, we suspect that the two forces were competing in (a) and not combining constructively.

3.5 CVBG temporal fidelity at high average powers

I would like to thank Matt Rever for characterizing the quality of pulses recompressed with the CVBG, as described in this section.

The longitudinal temperature distribution described in section 3.3 also affects the temporal fidelity of the recompressed pulse. This temperature distribution produces a corresponding refractive-index modulation, which affects the local Bragg condition. In effect, this modifies dispersion characteristics of the CVBG with increasing thermal load. This effect can be compensated, however, if the CVBG is operated in a reciprocal configuration, such that both stretched-signal beam and compressed-signal beam are spatially overlapped (albeit propagating in opposite directions in the CVBG). This ensures that any dispersion modification induced by thermal loading produces phase contributions into stretched and recompressed pulses that are equal in magnitude but opposite in sign, resulting in complete cancellation of the net effect in the recompressed pulse.

To facilitate comparison to experiment, the thermo-optic coefficient is 8.6e-6 K^{-1}.

The plot shows good agreement between the model and the experiment. Also, the data shows that overlapping the beams is essential in obtaining high-fidelity recompressed pulses. Note that the optimal case of perfectly overlapping the beams results in transform-limited pulses, however, to avoid crosstalk and damage to the system, the compressed beam must be at a small angle with respect to the grating (and the stretched beam). Hence there will always be some temporal distortion that is in proportion to the incident laser power but inversely proportional to the CVBG absorption coefficient. Figure 3.18 illustrates the effect that the non-ideal overlapping has on the recompressed pulses for an 80% efficient, 3 cm long CVBG with 10 nm bandwidth for up to 200 W of input power at an absorption of 0.01 cm^{-1}. Transfer matrices were used to compute the effect of grating dispersion on the recompressed pulses.

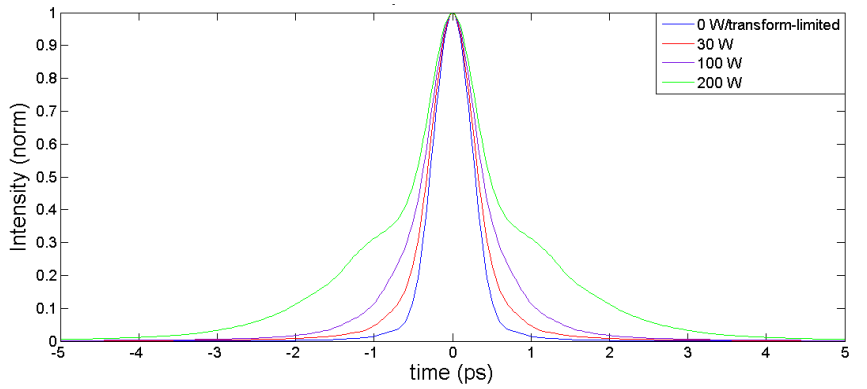

a. Computed recompressed autocorrelations for various input powers

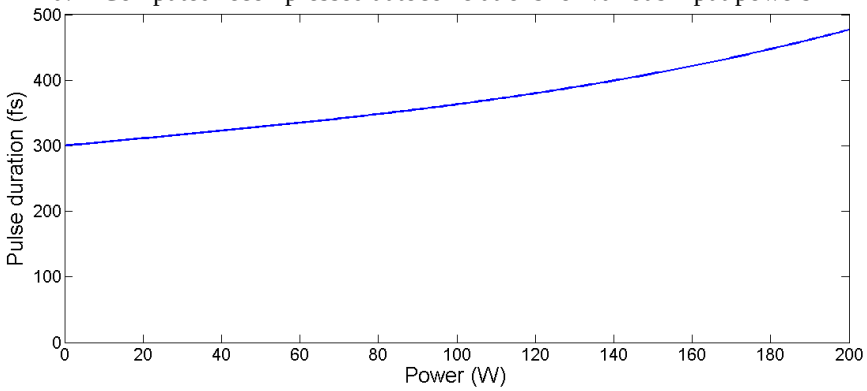

b. Recompressed FWHM pulse duration vs. input power for 10 nm CVBG

Figure 3.18 Computed recompressed autocorrelations and recompressed FWHM pulse duration vs. input power for 80% efficient, 3 cm long, CVBG with 10 nm bandwidth

Figure 3.18a shows the recompressed pulse autocorrelations as a function of input power, and Figure 3.18b shows the FWHM duration power dependence. As can be seen, the thermal effects have a much more profound effect on the wings than on the main pulse peak.

To verify the efficacy of the model, the autocorrelations computed at various powers and overlap conditions are compared to measurements. At low power (<10 W), the resulting pulses are found to be transform-limited (computed from the zero-phase FFT of the measured compressed spectrum) both in theory and measurement. At a moderate power of 50 W, a deviation from the transform-limit is observed, as shown in Figure 3.19.

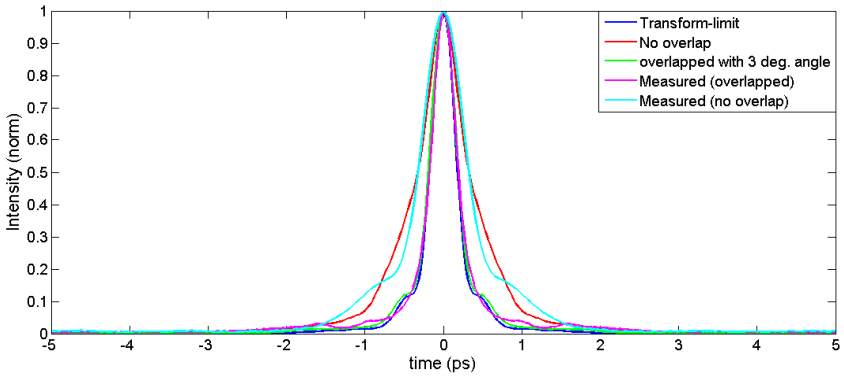

Figure 3.19 50 W autocorrelations, theoretical and measured

The plot shows good agreement between the model and the experiment. Also, the data shows that overlapping the beams is essential to obtain high-fidelity recompressed pulses. Note that the small angle at which the beam is sent into the CVBG implies that there will always be some temporal distortion that is proportional to the incident laser power but inversely proportional to the CVBG absorption coefficient.

Good agreement between the analysis and the measured data is also seen at higher powers, shown in Figure 3.20 and Figure 3.21, corresponding to 100 W of incident power and 150 W of incident power, respectively.

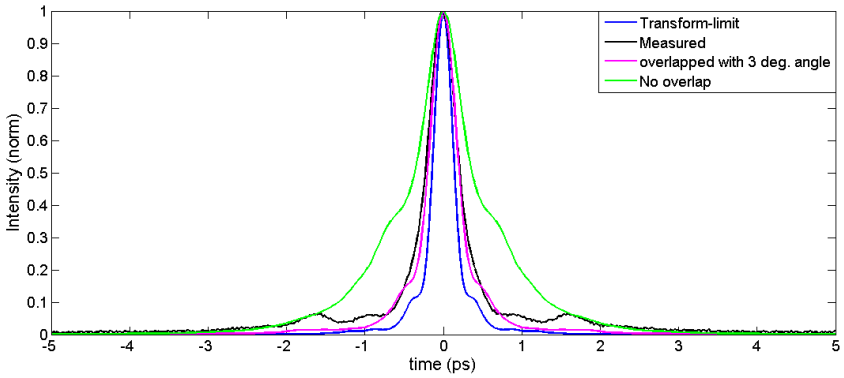

Figure 3.20 100 W autocorrelations, theoretical and measured

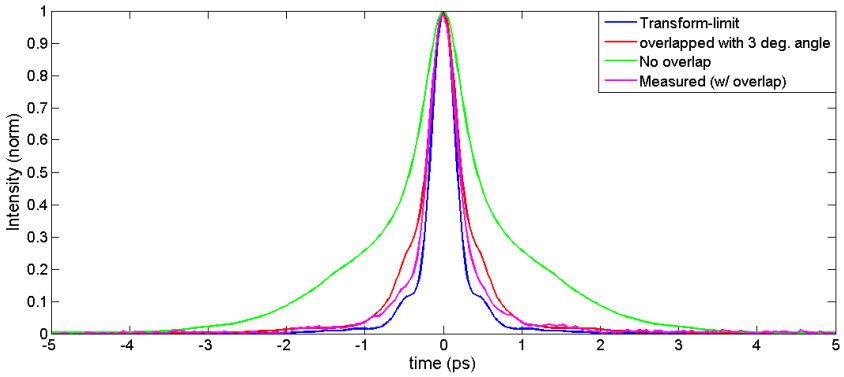

Figure 3.21 150 W autocorrelations, theoretical and measured

These plots indicate that the 3D model captures the power effects on the grating dispersion. Therefore, the performance at higher powers can be extrapolated.

The main result is that the longitudinal temperature distribution in the CVBG produces significant dispersion change at the power range from 100 W to ~200 W. However, because the effect of this longitudinal distribution can be compensated by overlapping counter-propagating beams in the same grating for stretching and recompression, temporal dispersion can be largely eliminated in this power range.

3.6 Generalized Results

Assuming that the optimal mounting conditions can be met, the spatial fidelity of the CVBG would be limited by the residual absorption, which could only be improved by reducing the absorbed power. Therefore, to generalize our simulation results for cases of different absorption coefficients, we recalculated them for a normalized product of power and absorption coefficient (measured in W/cm). This captures the fact that CVBG thermal loading depends not only on the incident optical power but also on its residual absorption. By decreasing this absorption, the thermal loading is reduced at fixed optical powers. Figure 3.22 shows reflected beam M^2 as a function of this normalized parameter.

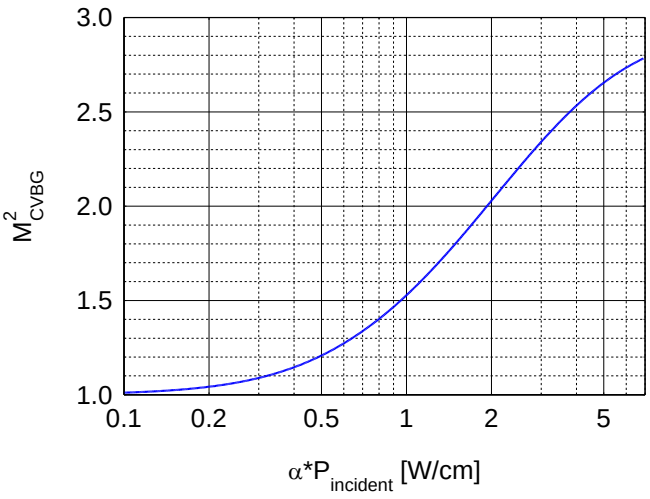

Figure 3.22 Spatial quality of the reflected beam as a function of incident power and CVBG substrate absorption coefficient.

In order for the CVBG to achieve better spatial fidelity under a high thermal load than that presented in this paper under the ideal mounting conditions, it is necessary to reduce the material absorption in the PTR substrate of the CVBG. Changes to the manufacturing techniques for CVBGs have reduced this absorption by an order of magnitude in the past, and it is possible for the next generation of CVBGs to have even less absorption.

To quantify the degradation of the recompressed pulse quality in a general way, a metric for the pulse duration that captures the various effects must be introduced. In analogy to the effective mode area commonly used to quantify the beam size exiting a fiber, an effective pulse duration is introduced as described in Eq. 3.11.

$$\tau_{eff} = \frac{\left(\int_{-\infty}^{\infty} P(t)dt\right)^2}{\int_{-\infty}^{\infty} P(t)^2 dt} \tag{3.11}$$

Here, P(t) is the temporal power signal and τ_{eff} is the pulse duration. This metric allows us to introduce a metric for the broadening that is independent of the bandwidth and transform-limited duration, as given in Eq. 3.12.

$$Q_t = \tau_{eff(recompressed)} / \tau_{eff(transform\text{-}limited)} \tag{3.12}$$

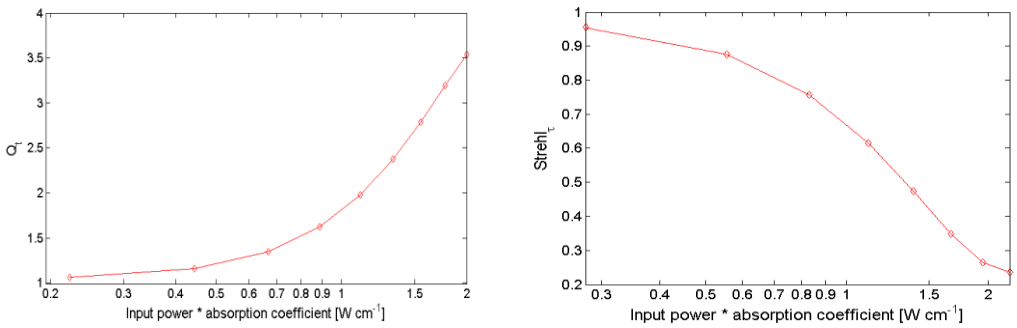

Figure 3.23 Recompressed pulse quality factor Q_t (left plot) and temporal Strehl ratio (right plot) as a function of thermal loading of CVBGs. Overlap between stretched and compressed beams in the same grating is assumed.

3.7 Conclusion

In summary, the main finding is that the power-scaling limits of the current generation of CVBGs is limited to somewhat below 200 W of average power at 1064 nm. Both experimental results and numerical modeling demonstrate that the main limiting factor is the transverse beam distortion, whereas temporal beam distortions can be compensated by overlapping stretched and recompressed beams in the CVBG. While numerical modeling suggests that the power limit for these transverse distortions would be closer to 1 kW, primarily because of the residual absorption in the PTR-glass substrate, experimental results show that the main limitation in CVBG performance is bending of the CVBG structure as induced by a high thermal load. From this, we can extrapolate how to improve the power-scaling performance of CVBGs, both by optimizing

the mounting conditions of the CVBG and by reducing the residual absorption of the PTR glass substrate.

3.8 References

1. L. Glebov, E. Flecher, V. Smirnov, A. Galvanauskas, and K.-H. Liao, “Stretching and compression of laser pulses by means of high efficiency volume diffractive gratings with variable periods in photo-thermo-refractive glass,” U.S. patent 7,424,185 B2 (9 September 2008).
2. G. Chang, M. Rever, V. Smirnov, L. Glebov, and A. Galvanauskas. "Femtosecond Yb-fiber chirped-pulse-amplification system based on chirped-volume Bragg gratings," Opt. Lett. 34, 2952-2954 (2009)
3. K-H. Liao, M-Y. Cheng, E. Flecher, V. I. Smirnov, L. B. Glebov, and A. Galvanauskas, "Large-aperture chirped volume Bragg grating based fiber CPA system," Opt. Express 15, 4876-4882 (2007)
4. L. Glebova, K. Chamma, J. Lumeau, and L. Glebov, “Photo-Thermo-Refractive glass – Properties and Applications,” OSA Technical Digest (CD) (Optical Society of America, 2011), paper AIThC2
5. S. Tjörnhammar, B. Jacobsson, V. Pasiskevicius, and F. Laurell. “Thermal limitations of volume Bragg gratings used in lasers for spectral control,” J. Opt Soc. Am. B **30**, 1402-1409 (2013)
6. M. Rever, S. Huang, C. Yahus, V. Smirnov, E. Rotari, I. Cohanoshi, S. Mokhov, L. Glebov, and A. Galvanauskas, "200 fs, 50 W Fiber-CPA System Based on Chirped-Volume-Bragg-Gratings," in *Conference on Lasers and Electro-Optics/International Quantum Electronics Conference*, OSA Technical Digest (CD) (Optical Society of America, 2009), paper CMBB2.
7. F. Laurell, P. Jelger, and V. Pasiskevicius, "Applications of Volume Bragg Gratings in High-Power Fiber Lasers," in *Optical Fiber Communication Conference*, OSA Technical Digest (CD) (Optical Society of America, 2010), paper OThQ3.
8. L. B. Glebov, "Fabrication and Applications of Volume Bragg Gratings," in *Advanced Photonics & Renewable Energy*, OSA Technical Digest (CD) (Optical Society of America, 2010), paper BMB1.
9. Y.-H. Chen and A. Galvanauskas. “Study of chirped pulse and Gaussian beam propagation in chirped volume Bragg grating compressors.” unpublished.

Chapter 4

Polarization dependence of high spatial frequency laser-induced periodic surface structures on silicon

4.1 Introduction

The discovery of laser-induced periodic surface structures (LIPSS) has been very intriguing because they present the ability to define structures on laser-irradiated surfaces with features well below the wavelength of the incident light, which means that features can be made smaller than the minimum achievable spot size. LIPSS have been studied on semiconductors such as silicon (Si) [1-10] and gallium arsenide (GaAs) [11-12], where LIPSS can change electro-optical properties, yielding an increase in optical absorption and photocurrent [12].

Although the physics guiding the formation of low spatial frequency LIPSS (LSFL) is fairly well understood, the physics guiding the formation of high spatial frequency LIPSS (HSFL) remains a topic of ongoing research with several competing models [11, 13-18]. One model [11] describes the evolution of HSFL through multiple surface morphologies. Initially, incident pulses excite valence electrons and soften inter-atomic bonds. Ions have a room temperature velocity distribution, and a small fraction can move away from their lattice site, drifting ¼ unit cell in about 1-2 ps before electrons relax and restore atomic bonds. Ions that move to interstitial sites significantly strain the lattice, and diffusion of these interstitials to the surface relieves this strain. Once adatoms reach the surface they coalesce into epitaxial islands

that are initially one or two atomic layers thick. Islands continue to grow with subsequent pulses. When islands reach a certain height, sets of islands begin to support a surface plasmon polariton (SPP) capable of inducing alignment of surface morphology because they are driven by preferential absorption at the crests of the SPP. Eventually, a LIPSS population forms with a period determined by the SPP wavelength. Strain accumulates in the LIPSS, and relaxation of the strain accumulation leads to bifurcation of the LIPSS. Experimental results of HSFL on GaAs are consistent with this model [11].

Of the many groups studying LIPSS on Si, one reported HSFL with an 80 MHz laser [1], while others reported LSFL with 1 kHz CPA systems [2-10]. Based on the aforementioned model, the formation of HSFL requires that incident pulses build a defect population faster than defects annihilate, and the recombination time of defects in Si might be much less than 1 ms. We show that a 49 MHz CPA system can be used to irradiate Si to form HSFL and to grow a thermal oxide. Moreover, the incident polarization defines the orientation of HSFL, which is consistent with the evolutionary model of HSFL.

4.2 Experimental Setup

The experimental setup is a chirped volume Bragg grating (CVBG) based fiber chirped pulse amplification (CPA) system that can provide 50 W average power and 10 μJ pulse energy at a variable repetition rate (Figure 4.1).

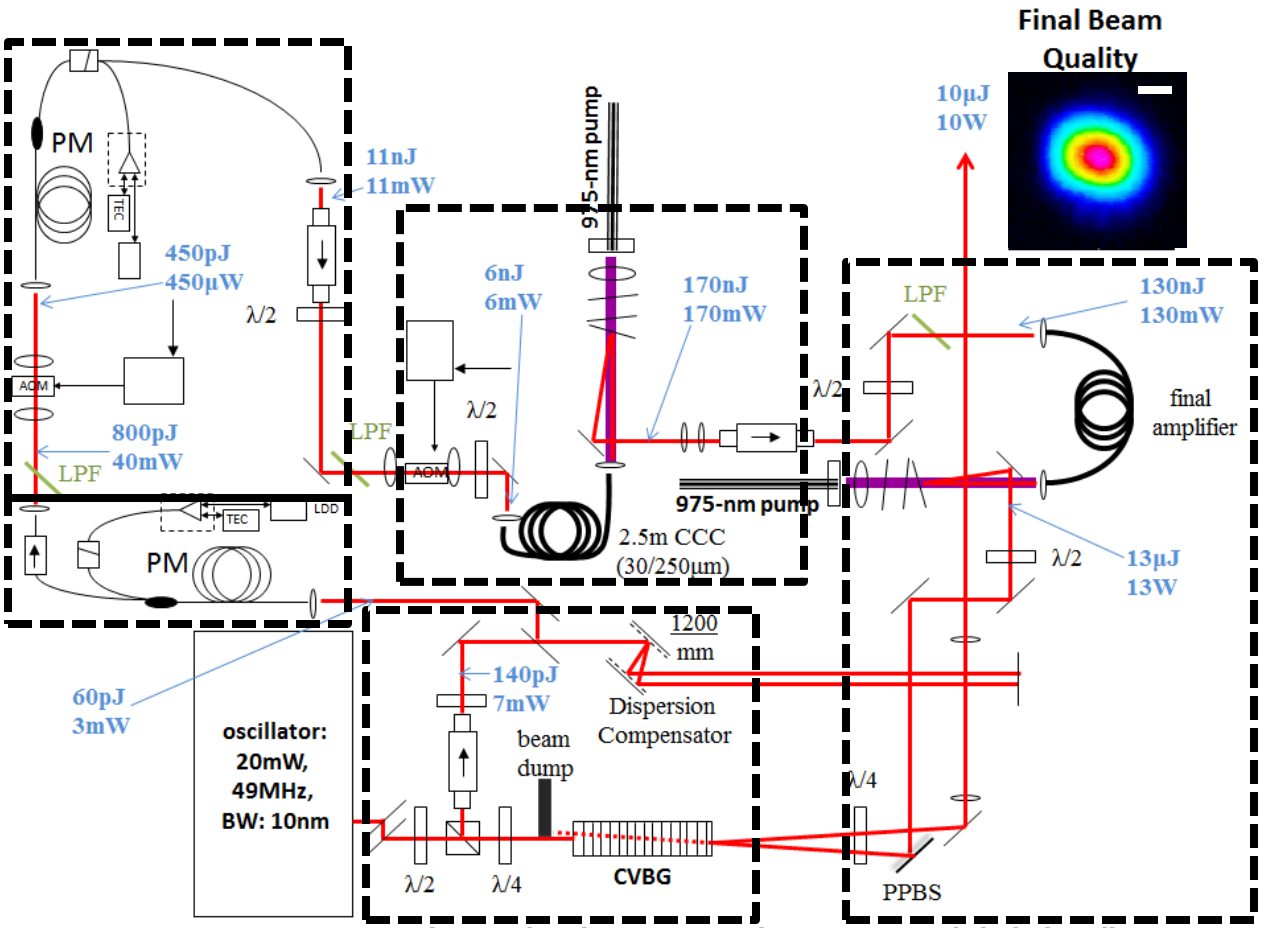

Figure 4.1 Experimental CVBG-based CPA system. The source is a mode-locked oscillator [20-21], and an acousto-optic modulator (AOM) sets the repetition rate for the system. A series of four amplifiers increase pulse energy to 10 µJ and average power to 50 W.

The source is a mode-locked oscillator with a 49 MHz repetition rate [20-21], and an acousto-optic modulator (AOM) downcounts the pulse train to set the repetition rate of the CPA system. The output Gaussian beam is linearly polarized and nearly diffraction-limited, with the measured $M^2 = 1.0$ in both directions (Figure 4.2a). The output pulses have a central wavelength of 1062 nm, and autocorrelations have a FWHM duration of 900 fs, corresponding to a FWHM pulse duration of 600 fs (Figure 4.2b).

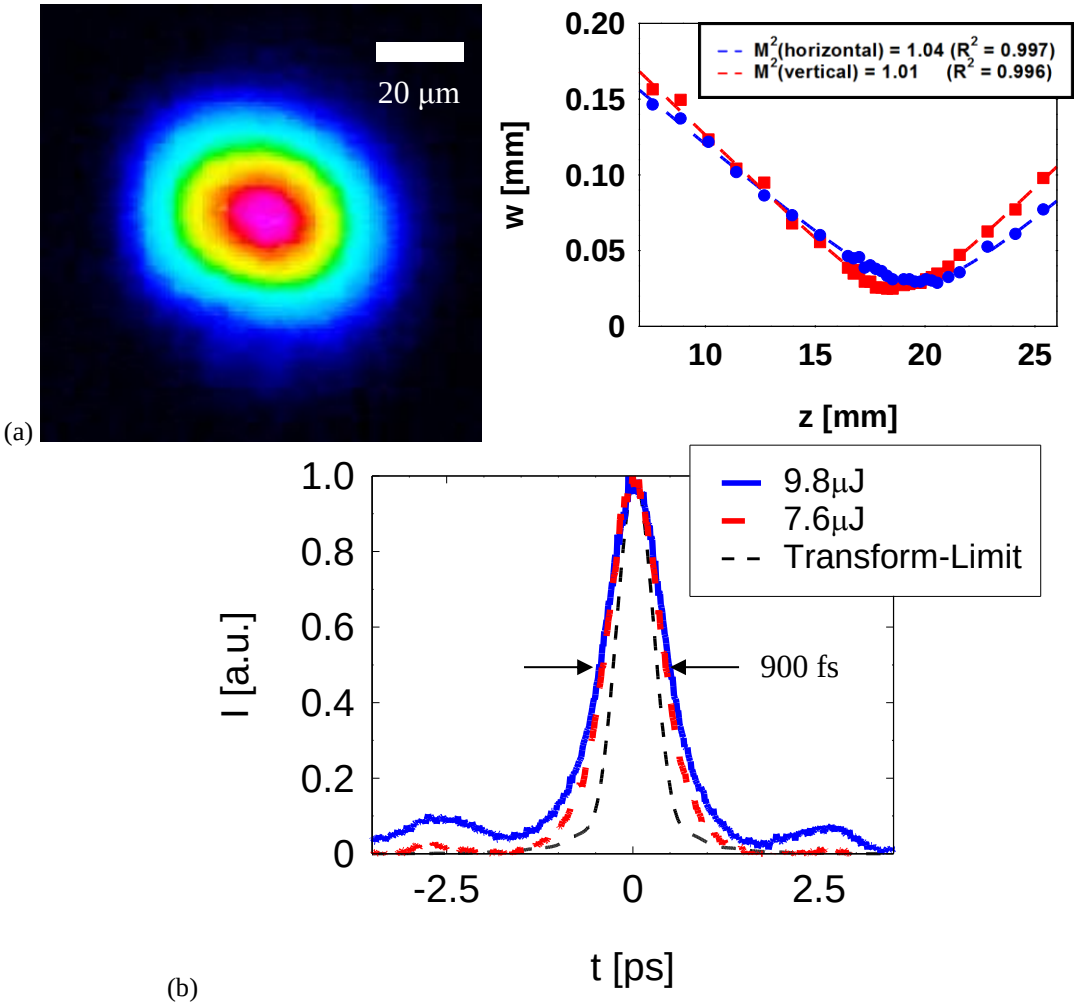

Figure 4.2 Experimental beam and pulse quality. (a) The output beam quality is diffraction-limited, and $M^2 = 1.0$ in both directions. (b) Autocorrelations of output pulses are 900 fs FWHM, corresponding to a FWHM pulse duration of 600 fs.

Before irradiation, 500 μm thick n-type (100) Si samples are cleaned with acetone, isopropanol, and ethanol, which is blown off with compressed dry nitrogen. Samples are irradiated in air in regions 40 μm wide by 1 mm long (Figure 4.3). Each region is irradiated with bi-directional raster-scanning, where a motorized translation stage translates the sample 1 mm to irradiate a track, and each subsequent track is irradiated in the opposite direction 2 μm below the previous track. The process is repeated until the entire region is irradiated.

Although scan direction reportedly influences the orientation of LSFL [5], it does not influence the orientation of HSFL on (100) Si. To demonstrate this, one sample is irradiated with

the incident polarization perpendicular to the scan direction, while another sample is irradiated parallel to the scan direction. In both cases, the orientation of HSFL is perpendicular to the incident polarization.

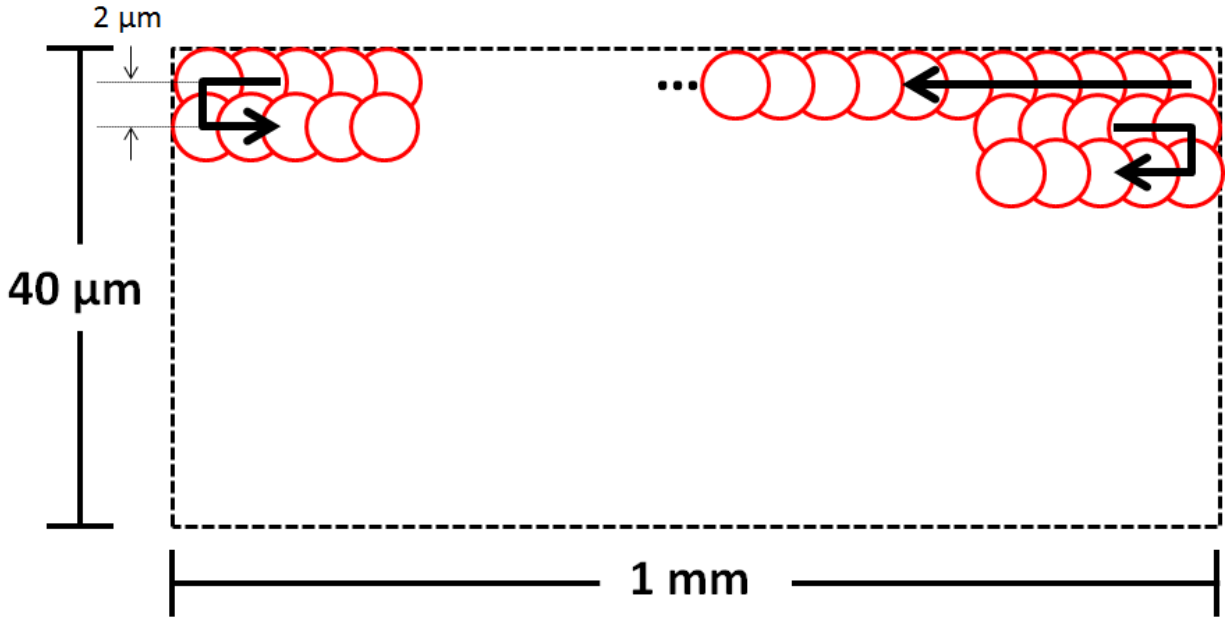

Figure 4.3 Raster scanning pattern used for HSFL formation on (100) Si. To irradiate a 40 µm X 1 mm region, a translation stage translates the sample 1 mm. An adjacent track is irradiated 2 µm away and is formed by scanning the sample anti-parallel to the initial scan direction. This pattern is repeated until the entire region is irradiated.

A halfwave plate and polarizing beam splitter control the fluence on target. HSFL form at fluences below the ultrafast melt threshold [22], which we estimate to be 0.33 J/cm^2 based on the ablation threshold of 0.38 J/cm^2 [23] and on the fact that the melt threshold is 15% lower than the ablation threshold for pulses centered at 780 nm [24].

We examine irradiated samples with a variety of techniques. Surface morphology is imaged with scanning electron microscopy (SEM, FEI Nova SEM/FIB) in secondary electron mode, and composition is measured with X-ray energy dispersive spectroscopy (EDS) from SEM. A laser confocal microscope (Olympus OLS 4000 LEXT) measures the height of

irradiated regions with a depth resolution of 12 nm. Samples are etched in buffered HF for 10 minutes to remove the thermal oxide that forms during irradiation, after which surface morphology is imaged with SEM.

4.3 Results and Discussion

Before etching, samples irradiated below melt threshold have aperiodic surface features (Figure 4.4a-b). An EDS measurement suggests the surface structure is SiO_2, which reaches a height of 850 ± 150 nm over the irradiated region (Figure 4.4c-d).

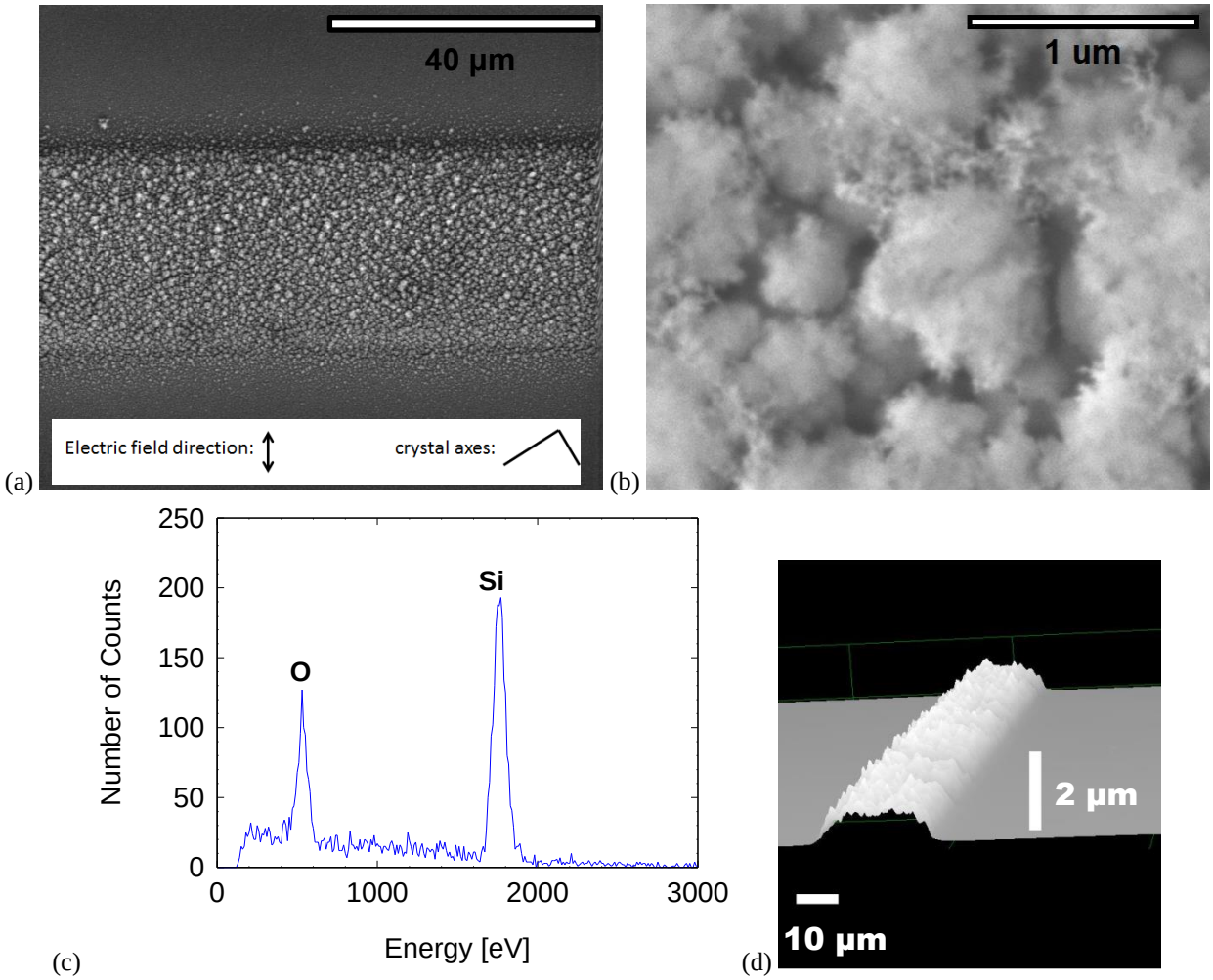

Figure 4.4 SEM image of irradiated Si surface before etching. The sample is irradiated at a fluence of 0.17 J/cm^2 at 49 MHz for 8*10^5 exposures per spot. (a-b) Aperiodic surface

features, about 1 μm in diameter, form on the irradiated region. (c) EDS suggests the existence of SiO_2, and (d) the structure reaches a height of 850 nm ± 150 nm. The scale bars on the last the image are 10 μm parallel to the surface and 2 μm in height.

The Si peak is higher than the O peak in the EDS measurement. Because EDS reveals the atomic composition of a material on the order of 1-10 μm below the surface [25], where penetration depth is a function of both the material and the accelerating voltage of the electron beam [26], the stronger Si peak suggests that the oxide is thinner than the penetration depth of the EDS.

LIPSS formations can be seen on the Si surface (Figure 4.5). The LIPSS period is 192 ± 19 nm, which is 0.18 ± 0.02 times the central wavelength of the incident pulses, and so they are HSFL [27]. We speculate that refraction at the air-oxide interface changes the fluence at the Si surface, although this might not influence the formation of HSFL. The growth of the oxide is governed by ultrafast absorption in Si, which is $6*10^5$ m^{-1} [28]. The thermal conductivity of Si decreases substantially with temperature [29], allowing heat to accumulate with subsequent pulses. If the pulse period is sufficiently long, heat accumulation would be negligible as the material would cool between pulses. If the pulse period is short enough, however, the thermal conductivity would decrease with each pulse. The time-dependent heat equation describes this more accurately [Eq. 4.1].

$$\rho C_p \frac{dT}{dt} + \nabla \cdot (-k(\boldsymbol{r},t)\nabla T(\boldsymbol{r},t)) = Q(\boldsymbol{r},t) \qquad 4.1$$

$$Q(\boldsymbol{r},t) = \alpha I(\boldsymbol{r},t)$$

In this equation, ρ is the mass density, C_p is the specific heat capacity, k is the thermal conductivity, T is the temperature, Q is the heat source, $\boldsymbol{r}$ is the spatial coordinate, and t is time.

The heat source is the absorption of the incident pulse train, where α is absorption and I is irradiance.

As the oxide grows, the air-glass interface takes on submicron surface features, as seen in the final formation in Figure 4.4**Error! Reference source not found.**b. Refraction at this interface distorts the wavefront of the incident pulses. The fluence at the Si surface is determined by wave propagation through the oxide, so an oxide with a thickness much less than the wavelength of the incident pulses will not substantially affect the fluence at the Si surface. Because thermal conductivity is temperature dependent and the temperature distribution depends on thermal conductivity, we expect the oxide to grow exponentially.

One consequence of this growth pattern is that the thickness of the oxide could be submicron until the final moments of irradiation, when the number of exposures far exceeds the number needed to form HSFL. The thermal oxidation would then be consuming the LIPSS. More precisely, if the Si near the interface melts and solidifies, it can solidify into amorphous-Si. Amorphous-Si has a thermal conductivity two orders of magnitude less than crystalline Si [30], although the α-Si layer may be too thin to store any significant amount of thermal energy. As a result, the temperature at the surface of the Si would still be determined primarily by the thermal conductivity of the (100) Si.

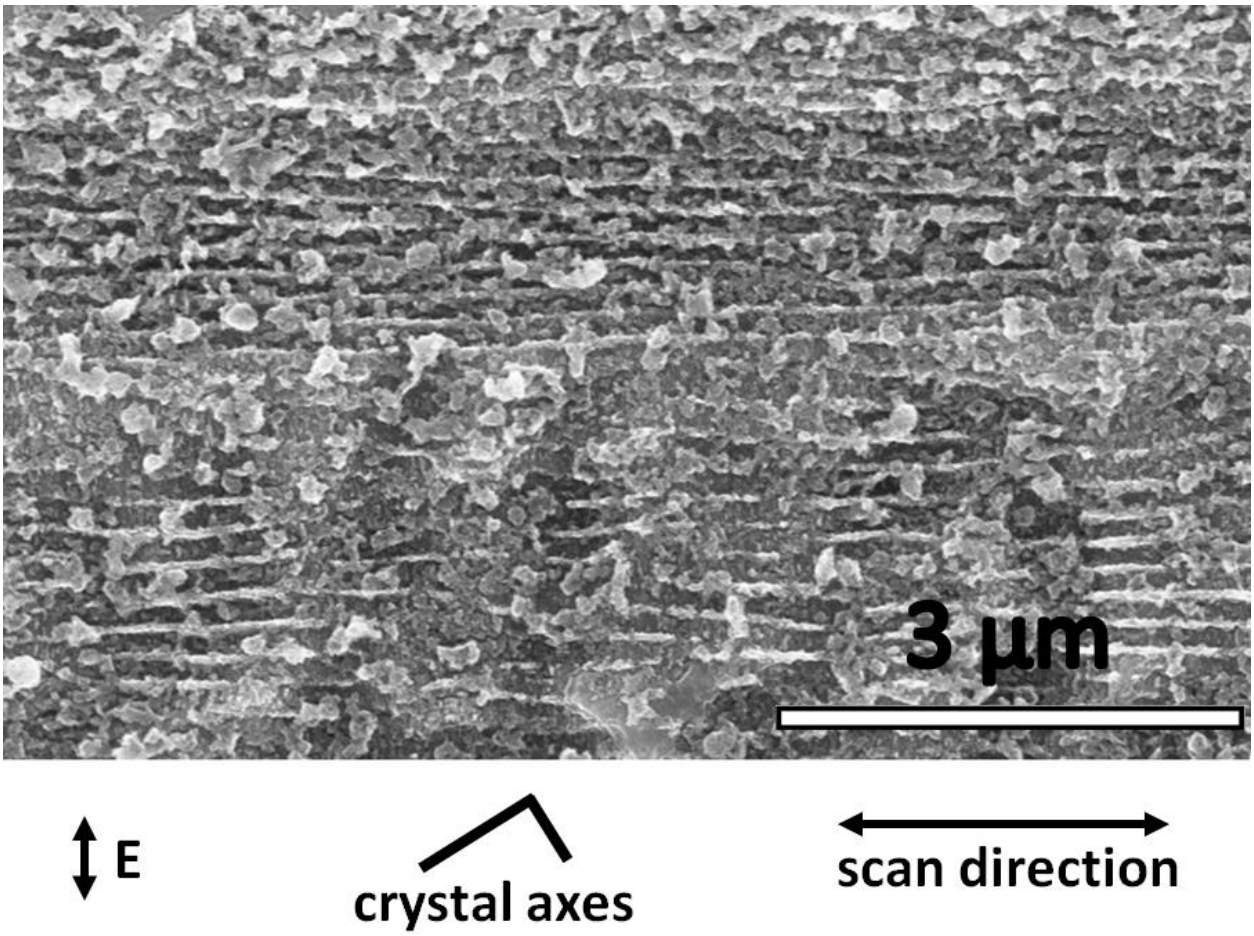

Figure 4.5 SEM of HSFL on (100) Si after etching off oxide. The sample is irradiated at a fluence of 0.17 J/cm^2 at 49 MHz with 8*10^5 exposures per spot. LIPSS formations have a period of 192 nm ± 19 nm, making them HSFL.

To demonstrate that the incident polarization defines the orientation of the HSFL, another sample is irradiated with the incident polarization parallel to the scan direction. Again, the HSFL formations are perpendicular to the incident polarization (Figure 4.6), revealing that it defines the orientation of HSFL, which is consistent with the model for the evolution of HSFL [11]. Moreover, the LIPSS period is 176 ± 14 nm, which is within one standard deviation of the LIPSS period for the first sample.

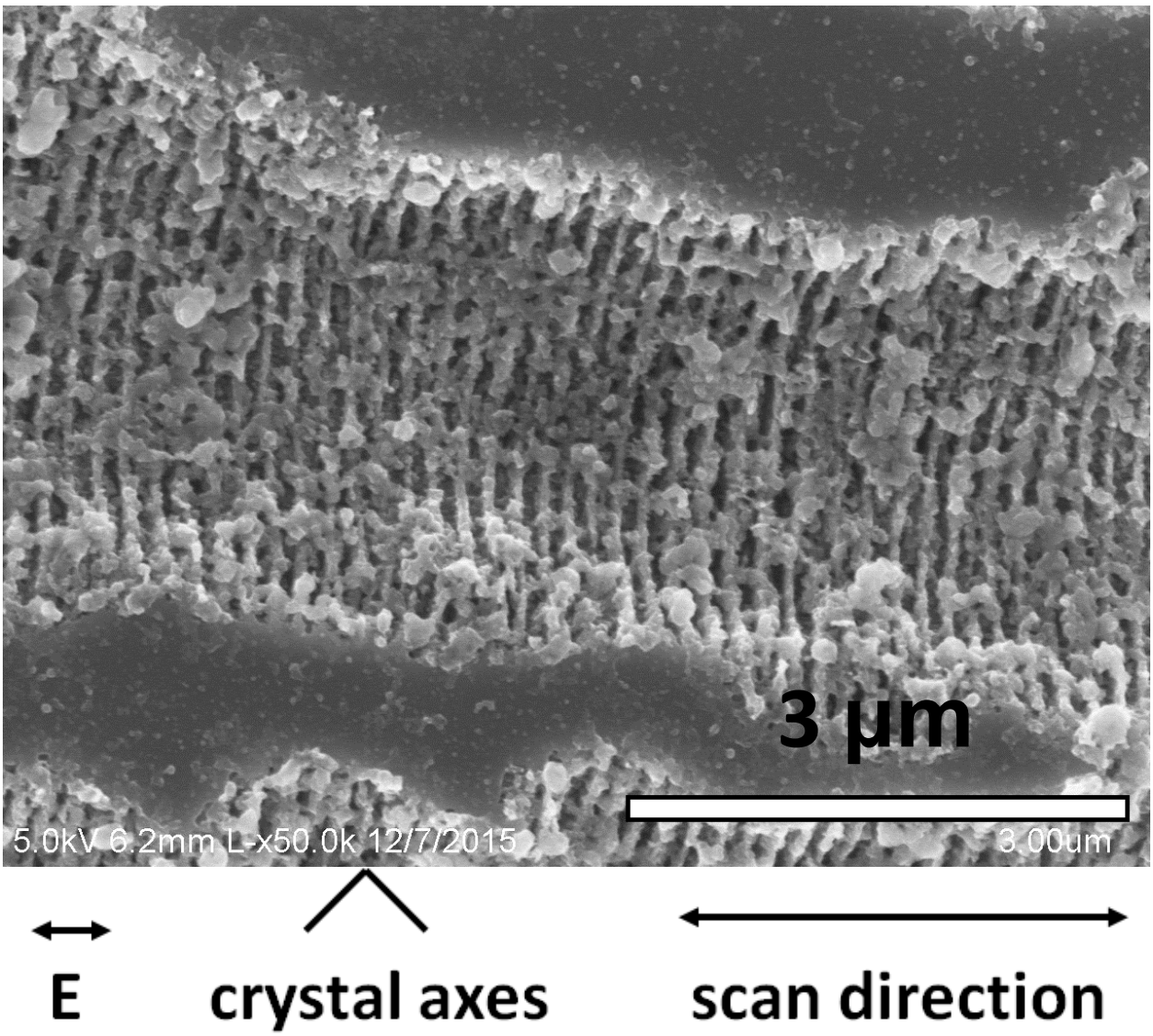

Figure 4.6 SEM of HSFL on Si, demonstrating that HSFL form perpendicular to incident polarization. The sample is irradiated at a fluence of 0.18 J/cm^2 at 49 MHz for 10^5 exposures. The LIPSS period is 176 nm ± 14 nm.

These results indicate that scan direction does not influence the orientation of HSFL on (100) Si, in contrast to a model showing that scan direction influences the orientation of LSFL on Si [5]. Instead, the orientation of the HSFL depends on the incident polarization, which is consistent with the model for the evolution of HSFL on semiconductors [11]. According to this model, the orientation of the HSFL is determined by SPP coupling at the surface of the semiconductor, and the SPP propagates along the direction of the incident polarization. The

polarization-dependence of HSFL formations on GaAs has already been shown [11]. Several other models exist to explain the polarization dependence of HSFL on semiconductors [13-18].

4.4 Conclusion

We have demonstrated that irradiation of (100) Si with a 49 MHz repetition rate CPA system can result in thermal oxidation and the formation of HSFL on the Si surface. Speculation about the thermal oxide suggests that it grows exponentially, and so it may not inhibit the formation of HSFL. Additionally, the orientation of the HSFL depends on the incident polarization and not on the scan direction. One explanation for this is that the model for the evolution of HSFL on GaAs, described in [11], applies to Si.

4.5 Acknowledgements

We thank the Michigan Center for Materials Characterization and the Lurie Nanofabrication Facility for the use of their equipment to characterize and etch samples.

4.6 References

1. R. Le Harzic, D. Dörr, D. Sauer, M. Neumeier, M. Epple, H. Zimmermann, and F. Stracke. "Large-area, uniform, high-spatial-frequency ripples generated on silicon using a nanojoule-femtosecond laser at high repetition rate." Optics Letters **36**(2), pp 229-231, 2011.
2. R. Kuladeep, V. Saikiran and D. N. Rao. "Femtosecond laser direct writing of sub-wavelength surface structures on metal and semiconductor materials." 12th International Conference on Fiber Optics and Photonics T3A.41, Kharagpur, India, 2014.
3. L. Jiang, W. Han, X. Li, Q. Wang, F. Meng, and Y. Lu. "Crystal orientation dependence of femtosecond laser-induced periodic surface structure on (100) silicon." Optics Letters **39**(11), 2014.
4. G. Deng, G. Feng, K. Liu, and S. Zhou. "Temperature dependence of laser-induced micro/nanostructures for femtosecond laser irradiation of silicon." Applied Optics **53**(14), pp 3004-3009, 2014.
5. P. Liu, L. Jiang, J. Hu, S. Zhang, and Y. Lu. "Self-organizing microstructures orientation control in femtosecond laser patterning on silicon surface." Optics Express **22**(14), #208658, 2014.
6. G. F. B. Almeida, R. J. Martins, A. J. G. Otuka, J. P. Siqueira, and C. R. Mendonca. "Laser induced periodic surface structuring on Si by temporal shaped femtosecond pulses." Optics Express **23**(21), #248153, 2015.
7. M. Bounhalli, M. Muth, O. Varlamova, and J. Reif. "Femtosecond Laser Ablation from Silicon and Ripples Formation: Evolution of Surface Excitation." The European Conference on Lasers and Electro-Optics, Paper# CM4_5, Munich, Germany, 2011.
8. M. Huang, F. Zhao, Y. Cheng, N. Xu, and Z. Xu. "The morphological and optical characteristics of femtosecond laser-induced large-area micro/nanostructures on GaAs, Si, and brass." Optics Express **18**(S4), #131320, 2010.
9. T. J.-Y. Derrien, J. Krüger, T. E. Itina, S. Höhm, A. Rosenfeld, and J. Bonse. "Rippled area formed by surface plasmon polaritons upon femtosecond laser double-pulse irradiation of silicon." Optics Express **21**(24), #197904, 2013.
10. W. Han, L. Jiang, X. Li, Q. Wang, H. Li, and Y. Lu. "Anisotropy modulations of femtosecond laser pulse induced periodic surface structures on silicon by adjusting double pulse delay." Optics Express **22**(13), #209279, 2014.
11. Abere, M. "From Point Defects to Ripples: Ultrafast Laser Induced High Spatial Frequency Laser Induced Periodic Surface Structures." Dissertation, University of Michigan, Ann Arbor 2015. Print.
12. Z-Y Zhao, Z-Q Song, W-Z Shi, and Q-Z Zhao. "Optical absorption and photocurrent enhancement in semi-insulating gallium arsenide by femtosecond laser pulse surface microstructuring." Optics Express **22**(10), #208639, 2014.
13. A. D. Dufft, A. Rosenfeld, S. K. Das, R. Grunwald, and J. Bonse. "Femtosecond laser-induced periodic surface structures revisited: A comparative study on ZnO." Journal of Applied Physics **105**, 034908, 2009.

14. B. A. Borowiec and H. K. Haugen. “Subwavelength ripple formation on the surfaces of compound semiconductors irradiated with femtosecond laser pulses.” Applied Physics Letters **82**, 4462, 2003.
15. C. T. Q. Jia, H. X. Chen, M. Huang, F. L. Zhao, J. R. Qiu, R. X. Li, Z. Z. Xu, X. K. He, J. Zhang, and H. Kuroda. “Formation of nanogratings on the surface of a ZnSe crystal irradiated by femtosecond laser pulses.” Physics Review B **72**, 125429, 2005.
16. F. Q. Wu, Y. Ma, R. Fang, Y. Liao, Q. Yu, X. Chen, and K. Wang. “Femtosecond laser-induced periodic surface structure on diamond film.” Applied Physics Letters **82**, 1703, 2003.
17. J. Reif, O. Varlamova, S. Varlamov, and·M. Bestehorn. “The role of asymmetric excitation in self-organized nanostructure formation upon femtosecond laser ablation.” Applied Physics A **104**, pp 969-973, 2011.
18. G. G. Miyaji and K. Miyazaki. “Origin of periodicity in nanostructuring on thin film surfaces ablated with femtosecond laser pulses.” Optics Express **16**, 16265, 2008.
19. W. L. Barnes, A. Dereux, and T. W. Ebbesen. “Surface plasmon subwavelength optics.” Nature **424**, pp 824-830, 2003.
20. A. Chong, J. Buckley, W. Renninger and F. Wise. “.All-normal-dispersion femtosecond fiber laser.” Optics Express **14**(21), #72994, 2006.
21. A. Chong, W. Renninger, and F. W. Wise. “High-energy femtosecond fiber lasers.” Proceedings of SPIE **6873**, 68730P, 2008.
22. S. K. Sundaram and E. Mazur. “Inducing and probing non-thermal transitions in semiconductors using femtosecond laser pulses.” Nature Materials **1**(4), December 2002.
23. D. P. Wan, J. Wang, and P. Mathew. “Energy deposition and non-thermal ablation in femtosecond laser grooving of silicon.” Machining Science and Technology **15**(3), pp 263-283, 2011. DOI: 10.1080/10910344.2011.595324.
24. H. O. Jeschke, M. E. Garcia, M. Lenzner, J. Bonse, J. Krüger, and W. Kautek. “Laser ablation thresholds of silicon for different pulse durations: theory and experiment.” Applied Surface Science pp 839-844, 2002.
25. R.S. Frenkel and D. W. Aitken. “Energy Dispersive X-Ray Emission Spectroscopy.” Applied Spectroscopy **24**(6), pp 557-566, 1970.
26. P. J. Potts. A Handbook of SILICATE ROCK ANALYSIS. Blackie & Sons, Ltd. 1987. Chapter 9.
27. J. Bonse, J. Krüger, S. Höhm, and A. Rosenfeld. “Femtosecond laser-induced periodic surface structures.” Journal of Laser Applications **24**(4), 042006, 2012.
28. M. A. Green and M. J. Keevers. “Optical properties of intrinsic silicon at 300 K.” Progress in Photovoltaics: Research and Applications **3**(3), pp 189–192, 1995. doi:10.1002/pip.4670030303
29. C. Prakash. “Thermal conductivity variation of silicon with temperature.” Microelectronic Reliability **18**, p 333, 1978.
30. H-S. Yang, D. Cahill, X. Liu, J. L. Feldman, R. S. Crandall, B. A. Sperling, and J. R. Abelson. “Anomalously high thermal conductivity of amorphous Si deposited by hot-wire chemical vapor deposition.” Physical Review B **81**, 104203, 2010.

Chapter 5

Second-Harmonic Generation in Scleral Collagen as a Guide for Controlled Subsurface Photodisruption

5.1 Introduction

Various proposed treatments of ocular infirmities, such as presbyopia and glaucoma, have involved the creation of subsurface channels in the sclera at precise depths [1, 2]. Femtosecond lasers are suitable to make these channels in a procedure similar to that of laser-assisted in situ keratomileusis (LASIK) surgery, which applies femtosecond lasers to corneal tissue. Channels form when focused laser pulses induce highly localized subsurface photodisruption that leaves minimal damage to the surrounding tissue [3].

Femtosecond lasers are not yet used in clinical settings to perform scleral surgery because clinical femtosecond lasers operate with a central wavelength around 1 μm, for which the sclera strongly attenuates the incident beam, primarily because of scattering [4]. Overcoming this attenuation has been difficult because the scattering coefficient varies strongly between samples, for which there could be several reasons, including hydration levels, intraocular pressure and tissue mechanical properties. One proposed solution involves optically clearing the sclera [5], although it may not be viable for *in vivo* applications. Another proposed solution is to use a central wavelength of 1.7 μm, for which scleral tissue is minimally scattering. Precise channel formation in sclera has been demonstrated *in vivo* for this wavelength [2], but this involves the

use of optical parametric amplification, which increases the complexity and reduces the reliability of a clinical system.

Performing precise scleral surgery with clinical femtosecond lasers requires knowing the optical properties of the tissue so as to predict the pulse energy needed for subsurface incisions. Without this measurement, excessive pulse energy would produce shallow incisions while insufficient energy would yield no incision.

This challenge inhibits the application of clinical femtosecond lasers to scleral surgery. Having a non-invasive probe that can make preliminary measurements to determine the scattering coefficient of the sample could make possible new treatments that require making subsurface incisions in the sclera. Because scleral tissue produces substantial second harmonic generation (SHG) [6], we investigate the use of SHG in scleral collagen as a probe that can measure the local optical properties of the tissue and determine the pulse energy needed for a subsurface incision.

5.2 Theoretical Model: Second Harmonic Generation

Tissues rich in type-I collagen are efficient media for SHG because of the non-centrosymmetric triple helical structure of the collagen molecules [6]. Sclera is composed of ~50% type-I collagen by weight and is known to emit a strong SHG signal in both the forward and backward direction when excited by a focused femtosecond laser pulse [7, 8]. For an *in vivo* application, an external detector can measure the backward-propagating SHG (B-SHG), whereas the forward-propagating SHG (F-SHG) will penetrate into the posterior sclera towards the vitreous chamber of the eye globe, where it is difficult to measure. Our analysis, therefore, focuses on the B-SHG that escapes the tissue, which depends on the tissue optical properties,

including the attenuation of the incident beam as it focuses in the tissue, the nonlinear susceptibility of the tissue around the focal plane, and the attenuation of the B-SHG signal emitted from the focal volume. The attenuation of the incident beam is assumed to be exponential with propagation depth z in the tissue, characterized primarily by $\mu_{s,\omega}$, the scattering coefficient of the frequency of the incident beam, which is much greater than the absorption coefficient [4]; the attenuation of the B-SHG is characterized similarly with $\mu_{s,2\omega}$.

Given the highly irregular structure of the lamellar collagen fibrils [9], the nonlinear susceptibility d_{eff} is expressed simply as a scalar quantity independent of the incident field polarization. The irradiance of the B-SHG $I_{2\omega}$ at the focal depth z_0 relates to the irradiance of the incident beam I_ω as follows:

$$I_{SHG}(z_0) = \left(\xi_B(z_0)\frac{\eta d_{eff}^2(z_0)}{A(z_0)}\right)\exp\{-2\mu_{s,\omega}z_0\} * I_\omega^2(z_0) \tag{5.1}$$

where ξ_B is the fraction of total SHG emitted backward, η is the characteristic impedance of the tissue, and A is the area of the beam, which presumably increases with depth because of scattering. Although B-SHG efficiency has been observed to decrease with depth [10-11], its behavior is not clearly defined, so experimental results were needed to determine the depth dependence of ξ_B, d_{eff}, and A, the factors that contribute to the B-SHG conversion efficiency. Taking the attenuation of the B-SHG signal into account as it propagates to the surface of the tissue, the measured signal by a detector is:

$$U_{meas} = \zeta_{exp}\left(\frac{\xi_B(z_0)d_{eff}^2(z_0)\eta}{A(z_0)\tau}\right)\exp\{-(2\mu_{s,\omega} + \mu_{s,2\omega})z_0\} * U_0^2 \tag{5.2}$$

where U_0 is the incident energy, τ is the pulse duration, and ζ_{exp} is a constant that combines various experimental parameters, including detector gain and quantum efficiency, lens collection angle, and filter transmission. This simple model ignores the contributions of any F-SHG photons that are backscattered.

The terms in Eq. 5.2 can be systematically combined to understand their physical meaning. One term, the exponential term $2\mu_{s,\omega} + \mu_{s,2\omega}$, represents the total scattering in the tissue, which we define as the compound scattering coefficient of the tissue. The amplitude in parenthesis is the B-SHG conversion rate of the tissue, which gives the B-SHG conversion efficiency for an arbitrary input energy. For our experiments, we normalize the B-SHG conversion efficiency for each sample to the highest measured conversion efficiency. We expect the B-SHG conversion efficiency to change with depth because of the irregular structure and composition of the sclera, which is primarily a mixture of collagen molecules and intraocular fluid [9].

Both tissue properties, the compound scattering coefficient and the B-SHG conversion efficiency, can be experimentally extracted by measuring the B-SHG signal at different focal depths and fitting an exponential curve to the data. The curve fit gives the amplitude and the exponential decay of the data, where the amplitude corresponds directly to the B-SHG conversion efficiency at the surface of the tissue but the exponential decay does not correspond directly to the compound scattering coefficient. Because we need to determine the functional form of B-SHG conversion efficiency with depth, it was necessary to measure data at multiple lateral locations and to relate the amplitude to the exponential decay $\mu_{measure}$ with Eq. 5.3:

$$\mu_{measure} = (2\mu_{s,\omega} + \mu_{s,2\omega}) + \gamma \ln\left(\frac{\xi_B(0) d_{eff}^2(0) \eta}{A(0)\tau}\right) \tag{5.3}$$

Experimental data from all samples verified that the form of Eq. 5.3 is appropriate and quantified γ for each sample.

5.3 Experimental Setup and Method

To test this model, full porcine ocular globes were acquired on ice from a slaughterhouse and processed them less than 24 hours after extraction. After each specimen was brought to room temperature, the extra-ocular muscles and conjunctiva were carefully removed with surgical scissors without damaging the scleral surface. To control for variations in intra-ocular pressure in globes that deflated during transport, balanced salt solution was injected through the optic nerve to maintain a pressure closer to physiological levels (~15 mmHg [12]). The globe was then positioned in a customized screw mount to applanate the treatment region against a glass window through which the laser pulses were delivered. Care was taken to ensure that the applanated scleral region was free of naturally-occurring pigmentation to minimize any effects of local absorption on laser attenuation.

Both probe pulses and subsurface cavitation pulses were delivered to the samples with a femtosecond fiber laser (Amplitude Systèmes, Satsuma) (Figure 5.1a) that provided ~400 fs pulses at a central wavelength of 1030 nm and a repetition rate of 40 kHz. A motorized half-wave plate and polarizer controlled incident pulse energy, up to a maximum of 6.5 μJ. An aspheric lens (Thorlabs, C230TMD-B) with an effective numerical aperture (NA) of 0.35 focused the laser beam into the porcine samples, which were mounted on an XY motorized stage. Moreover, galvanometric scanners (Thorlabs, GVSM002) were used to sweep the laser focus laterally across the sample.

Our experimental method consisted of two consecutive stages. First, single low-energy probe pulses were delivered at several depths and many different lateral locations across a 0.5 mm X 1 mm region of the tissue to stimulate the B-SHG signal and extract the local optical properties with Eq. 5.2. The area of the region was similar to an area suitable for scleral implants and was large enough to resolve with an optical coherence tomography (OCT) scanner. Care was taken to ensure that the pulse energy was kept well below energy levels where molecular or mechanical damage was suspected. The incident pulses were focused at several depths below the surface, from 200 μm to the target depth of 300 μm where the incision was later attempted, to extract experimentally the local optical properties by fitting the data to Eq. 5.2. The amplitude and exponential decay from the curve fits at each lateral location were later processed with Eq. 5.3 to determine the rate γ at which conversion efficiency changed with depth. The B-SHG signal from each pulse was collected through the focusing lens and spectrally isolated from reflections at the fundamental wavelength using a dichroic mirror (532/1064 nm) and a pair of spectral filters (a narrow-band 515 nm filter as well as a Schott low pass color filter). A photomultiplier tube detector (Hamamatsu) collected the B-SHG signal, and a USB-connected oscilloscope (Rigol) digitized and recorded the amplified signal.

After collecting B-SHG over the entire 0.5 mm X 1 mm region, we attempted to perform femtosecond laser disruption in the same area in the tissue at a depth of 300 μm. To this end, the laser pulse energy was incrementally adjusted until a disruption layer was observed using an OCT (Zeiss Visante). To form each disruption layer, high-energy (μJ) pulses were delivered at a 40 kHz repetition rate while galvanometric scanners swept the beam ±40 μm to either side of focus (10 mrad) and a motorized translation stage translated the sample at 0.05 mm/s until a 1 mm long region was irradiated. This process was repeated six times to irradiate the entire

0.5 mm X 1 mm region. After the area was irradiated, the sample was imaged with an OCT to determine the minimum energy needed for subsurface damage. Figure 5.1b is an OCT image showing a 3 mm long incision at 260 μm depth below the scleral surface. Note that the dark area below the incision plane is an OCT artifact produced by losses in the OCT signal due to strong scattering along that plane.

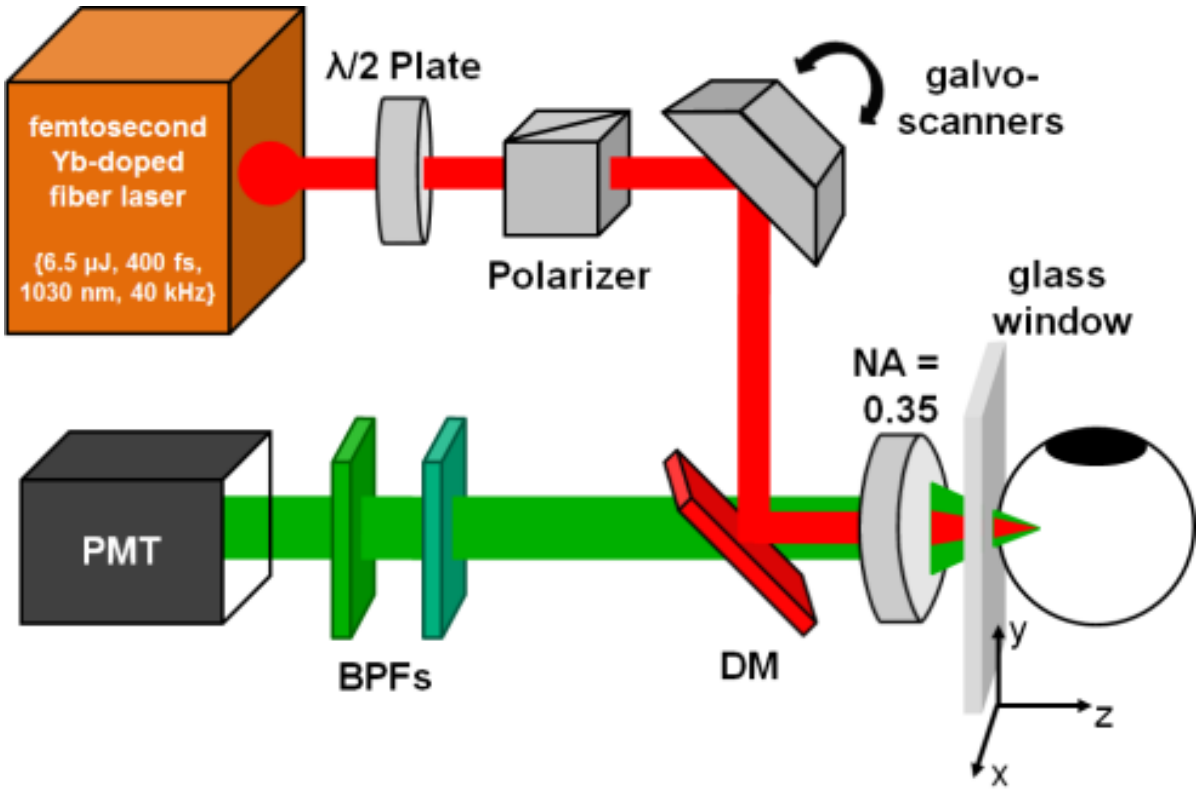

(a)

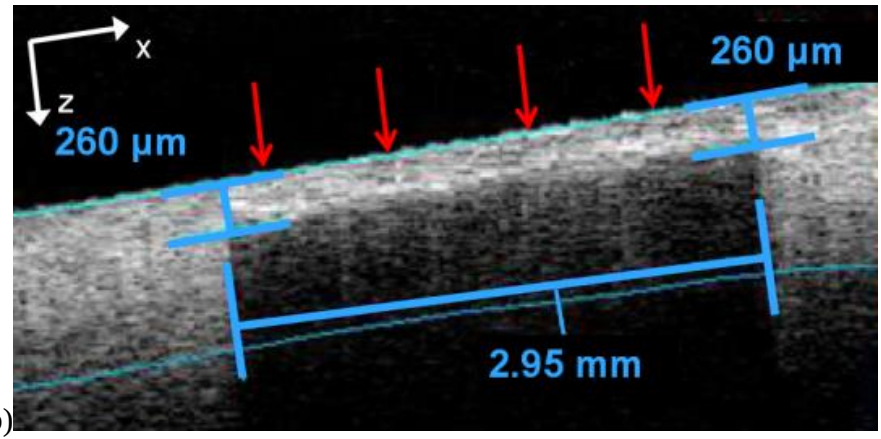

(b)

Figure 5.1 (a) Experimental setup for B-SHG measurements and femtosecond laser microsurgery. Pulses from a femtosecond fiber laser were focused using a 0.35 NA aspherical lens into unpigmented regions of sclera in whole *ex vivo* porcine ocular globes. A half-wave plate and polarizer controlled the incident pulse energy to alternate between low-energy B-SHG probe pulses and high energy (µJ) surgery pulses. B-SHG signal generated in the sclera was collected by the focusing lens, spectrally filtered using a dichroic mirror (DM) and 2 bandpass filters (BPFs), and detected with a photo-multiplying tube (PMT). When applying high-energy pulses, the tissue was translated 1 mm along the X direction using a motorized stage while the laser focus was swept ±40 µm across the Y direction with the galvo scanners to create 2D subsurface incisions parallel to the scleral surface. Several parallel adjoining tracks were made serially to form incisions 0.5 mm in Y by 1 mm in X. (b) After an incision was attempted, an OCT revealed if the attempt was successful. In this image, a 3 mm long subsurface incision was made successfully at a depth of 260 µm.

5.4 Results and Discussion

For 26 porcine globes, we collected B-SHG data, namely the compound scattering coefficient and the normalized B-SHG conversion efficiency, as well as the minimum pulse energy required for an incision. Each globe was sampled at multiple sites, each the same size (0.5 mm X 1 mm, 200-300 μm range of depths for B-SHG measurements), and for each site, the B-SHG signal was obtained from single laser pulses focused at various depths. The focal depth was measured relative to the anterior scleral surface, which was determined accurately by translating the objective lens along the direction of propagation while monitoring the B-SHG signal, which peaked as the focus of the beam crossed the glass-tissue interface (Figure 5.2a).

We then measured the B-SHG signal at several different focal depths, and by fitting the results for each lateral location to the exponential form in Eq. 5.2, we extracted the normalized B-SHG conversion efficiency at the surface and the exponential decay of the signal (Figure 5.2b). The values for all lateral locations in the sample were also averaged to obtain an average and standard deviation of the B-SHG conversion efficiency across the region where a subsurface incision was attempted.

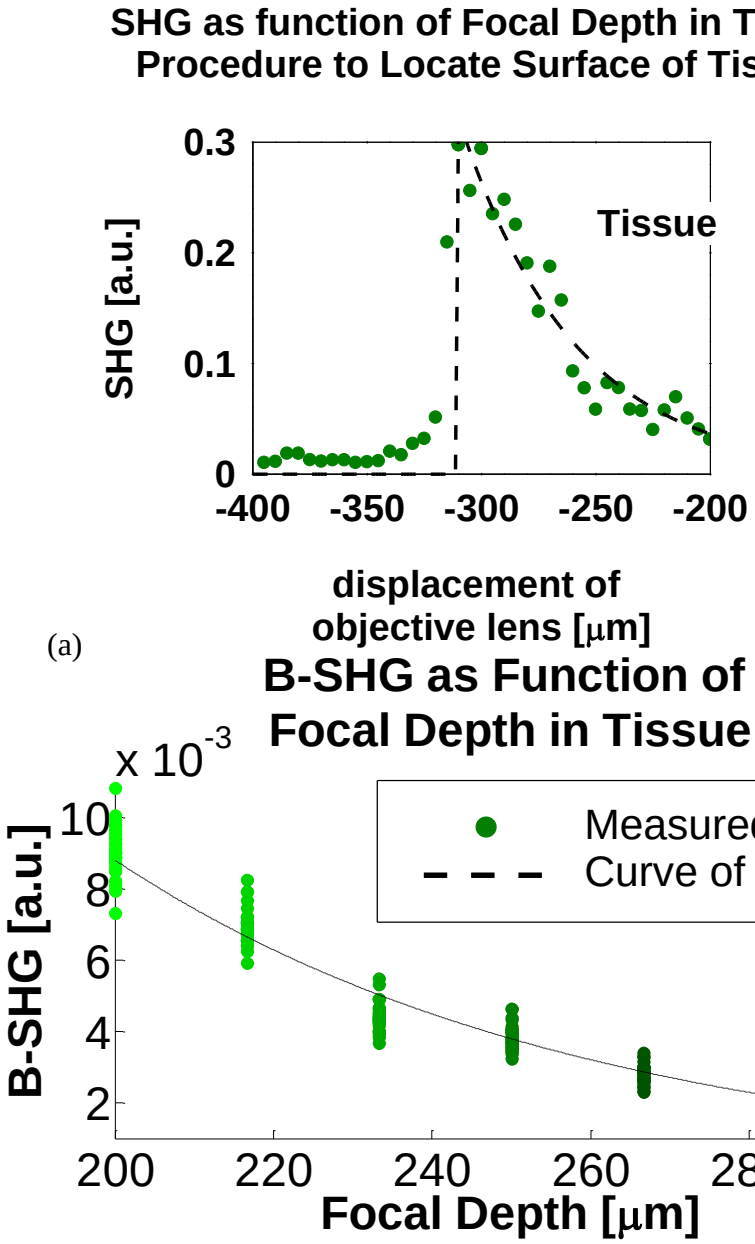

Figure 5.2 (a) B-SHG was used to determine the surface of the tissue so as to focus accurately at the target depth. Measured B-SHG signal (green dots) from the center of the region of interest in a single porcine scleral sample peaked at the surface of the tissue and decayed exponentially with focal depth. (b) Measured B-SHG signal (green dots) sampled with the laser focused at depths ranging from 200 to 300 μm below the surface. The corresponding exponential fit of this data to Eq. 5.2 (dashed line) yielded the averaged B-SHG conversion efficiency (0.26 a.u.) and exponential decay (168 cm^{-1}). A curve fit for each lateral location yielded the B-SHG conversion efficiency and exponential decay for each lateral location in the probed region.

With this data from the sample, we were able to determine how the B-SHG conversion efficiency changed with depth. The B-SHG conversion efficiency and exponential decay were compared for all lateral locations, which revealed a highly logarithmic relation between the exponential decay and the B-SHG conversion efficiency (Figure 5.3). It is worth noting that all 26 porcine ocular globes showed this relation. Based on Eq. 5.2, the compound scattering coefficient would not be strongly related to the B-SHG conversion efficiency, so we determined that the B-SHG conversion efficiency was decreasing exponentially with depth at a rate γ and that the constant in the logarithmic relation in the data must be the average compound scattering coefficient in the sample. From this, we were also able to determine the average and standard deviation of the compound scattering coefficient for each region of the ocular globe.

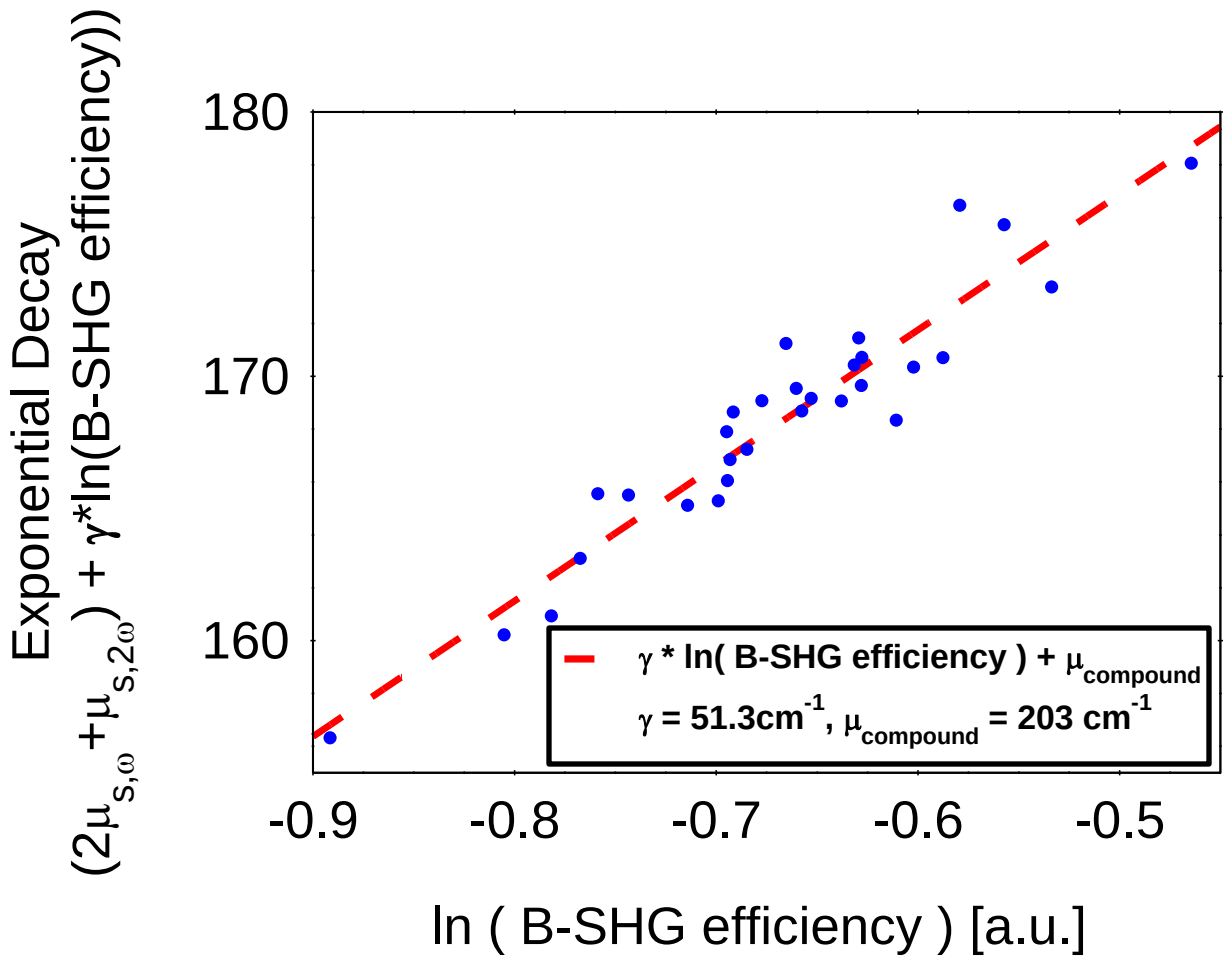

Figure 5.3 Measured B-SHG signal from Figure 5.2 plotted by lateral location. At each lateral location, the corresponding B-SHG conversion efficiency and exponential decay (blue dots) were strongly correlated, revealing the relation of the exponential decay in the measurement to the change in B-SHG conversion efficiency with depth. The linear curve fit of this data could then be interpreted with Eq. 5.3 (dashed line) to determine the measured γ, assumed to be uniform in the region, as well as the compound scattering coefficient for each lateral location in the sample.

Averaging over all 26 ocular globes, we obtained a mean compound scattering coefficient of 201 ± 25 cm^{-1}, which was in excellent agreement with previously published results that measured the porcine sclera optical properties using a conventional integrating sphere [4].

To relate the local optical properties of the sclera to the energy needed to create subsurface incisions, high-energy incident pulses were focused at a depth of 300 μm and a subsurface incision was attempted with increasing pulse energy until a distinct photodisruption

layer was observed in OCT images. The OCT revealed the photodisruption layer with a shadow beneath the layer; this shadow was attributed to scattering of the OCT signal by cavitation bubbles produced during irradiation from high-energy pulses.

For each scleral sample from which we collected B-SHG data, pulse energy was increased incrementally until subsurface damage was achieved. In Figure 5.4, which is the OCT scan of the sample shown in Figure 5.2 and in Figure 5.3, 3 adjacent subsurface incisions were attempted at a 300 μm depth with pulse energy of 4.6 μJ, 5.2 μJ, and 5.9 μJ. While the lowest two energy levels did not result in strong contrast in the OCT image about the focal plane, the highest energy resulted in a distinct shadow. We determined the threshold for photodisruption to be the lowest energy at which we observed a clear OCT shadow (5.9 μJ in this case), and we repeated this process of determining the damage threshold for all 26 samples after measuring the optical properties for each sample.

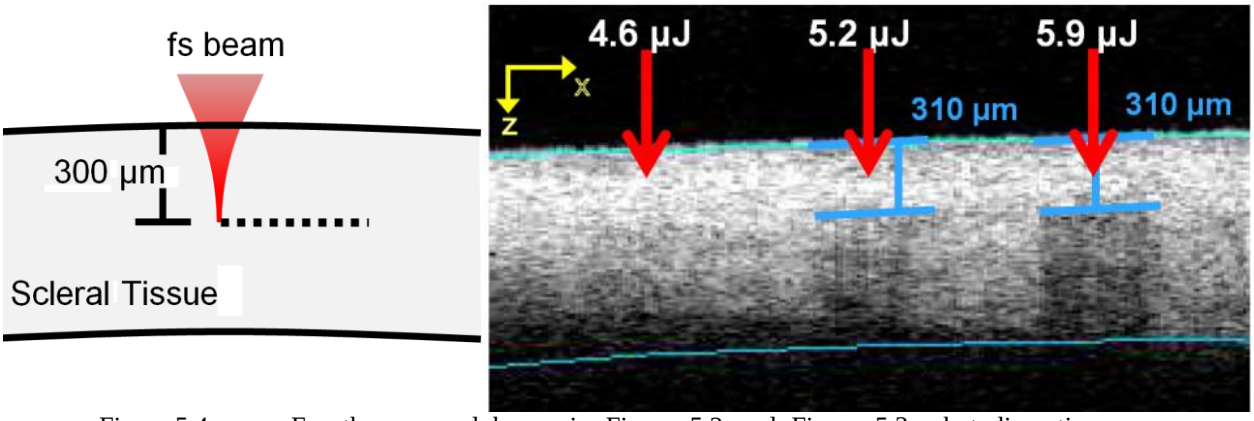

Figure 5.4 For the same globe as in Figure 5.2 and Figure 5.3, photodisruption was attempted at a target penetration depth of 300 μm with a range of incident pulse energy, specifically 4.6 μJ, 5.2 μJ, and 5.9 μJ. The OCT resolved damage at 300 μm for the incident pulse energy of 5.9 μJ.

For practical applications, it is necessary to find a correlation between the tissue optical properties and the energy threshold for photodisruption so that B-SHG can be used as a non-

invasive probe to predict this energy. The data collected from all 26 ocular globes reveals a moderate negative correlation between the normalized B-SHG conversion efficiency and the energy threshold for photodisruption (ρ=-0.614) (Figure 5.5a). To explain this, we assume that the B-SHG conversion efficiency depended mostly on the collagen molecules and negligibly on the interfaces between the intraocular fluid of the sclera and the collagen fibrils, which might have generated weak SHG signals [13]. Because a pure collagen scaffold has a considerably lower damage threshold [14] than water [15], we speculate that a higher density of collagen molecules yields a higher B-SHG conversion efficiency and a lower damage threshold, hence the negative correlation.

We would also expect the data to reveal that the energy threshold for photodisruption would depend exponentially on the scattering coefficient, albeit on the scattering coefficient of the fundamental wavelength rather than the compound scattering coefficient. Comparing the compound scattering coefficient to the energy threshold for photodisruption for the same data set (Figure 5.5b), the best fit reveals an exponential dependence of the energy threshold on the compound scattering coefficient after applying a correction factor to reduce the compound scattering coefficient to $\mu_{s,\omega}$, the scattering coefficient of the incident beam. This correction factor was 4.4, and based on previously published results, we expect this correction factor to be slightly greater than 4 [16].

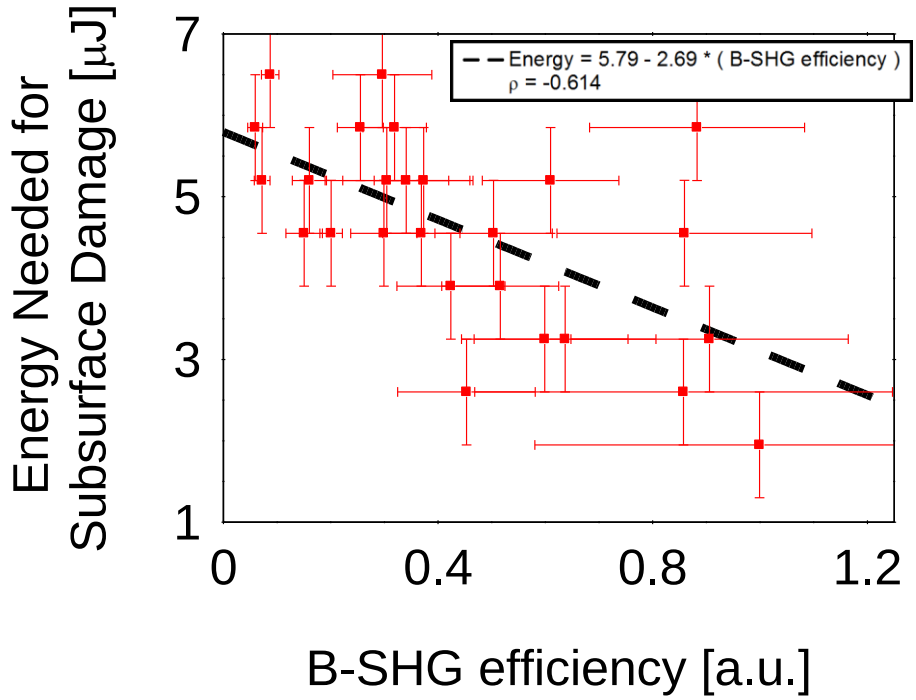

(a)

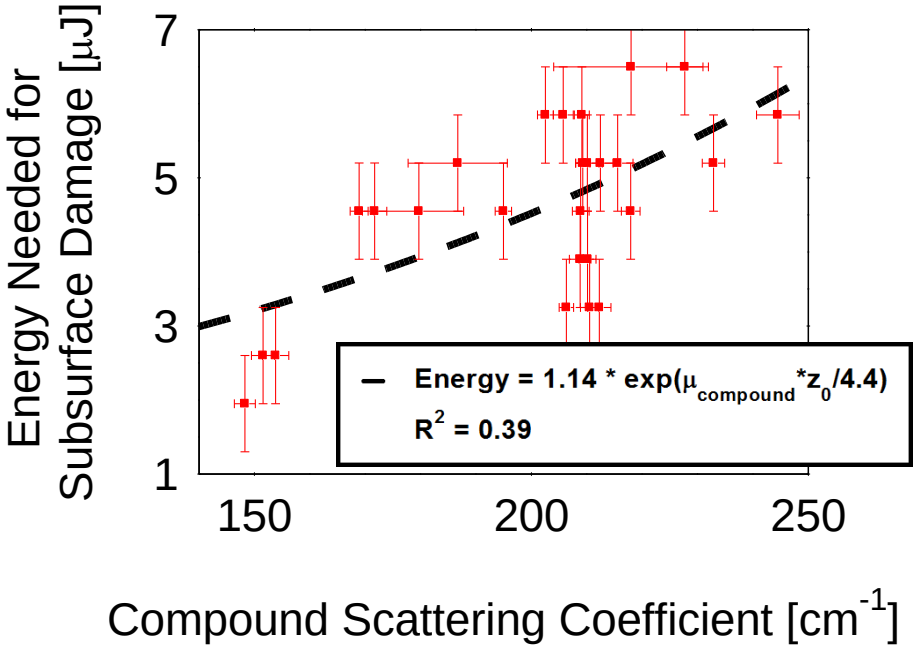

(b)

Figure 5.5 Energy needed for subsurface damage relates to the B-SHG conversion efficiency and the scattering coefficient of the incident beam. For 26 porcine ocular globes, the pulse energy needed for subsurface damage was compared to (a) the B-SHG conversion efficiency and (b) the compound scattering coefficient ($2\mu_{s,\omega} + \mu_{s,2\omega}$) of the B-SHG probe. (a) A moderate negative correlation (ρ = -0.614) was observed between B-SHG conversion efficiency and the minimum pulse energy needed for photodisruption at a penetration depth of 300 μm. (b) An exponential dependence of the minimum pulse energy needed for cavitation on ($2\mu_{s,\omega} + \mu_{s,2\omega}$) indicated the correction factor of 4.4 to reduce ($2\mu_{s,\omega} + \mu_{s,2\omega}$) to $\mu_{s,\omega}$, where previously published results indicate a correction factor slightly larger than 4 [16].

Based on these results, we see that we can use B-SHG as a non-invasive probe to determine the scattering coefficient for the tissue at the wavelength of the incident beam. We also introduce a relation between the B-SHG conversion efficiency and the energy needed for subsurface damage. These relations could be used, with some error, to determine the energy needed for subsurface cavitation in *ex vivo* porcine sclera.

5.5 Conclusion

We demonstrate that it is possible to use B-SHG in collagen-rich tissues, such as the sclera, to measure the tissue optical properties. Local measurements of these properties could then be used to estimate the laser parameters needed for subsurface disruption in the tissue, leading to more precise subsurface surgical incisions. This technique offers new modalities for the treatment of various ocular infirmities like glaucoma and presbyopia.

5.6 References

1 M. Qazi, J. Pepose, J. Shuster. “Implantation of Scleral Expansion Band Segments for Treatment of Presbyopia.” American Journal of Ophthalmology **134**(6), December 2002.

2 D. Chai, G. Chaudhary, E. Mikula, H. Sun, R. Kurtz, T. Juhasz. “*In vivo* femtosecond laser subsurface scleral treatment in rabbit eyes.” Lasers in Surgery and Medicine **42**, pp 647-651, 2010.

3 K Plamann, F Deloison, F Druon, E Mottay, F Morin, F Aptel, P Georges, V Nuzzo, C L Arnold, D A Peyrot, M Savoldelli, A Courjaud, M Hanna, C Crotti, J-M Legeais. “Ultrashort pulse laser surgery of the cornea and the sclera.” Journal of Optics **12**, 2010.

4 M. Hammer, A. Roggan, D. Schweitzer, G. Müller. "Optical properties of ocular fundus tissues -- an *in vitro* study using the double-integrating-sphere technique and inverse Monte Carlo simulation." Phys Med Biol **40**, 1995.

5 A.A. Alekhin, A.A. Ionin, S.E. Kozhushko, I.M. Kourylyova, S.I. Kudryashov, K.K. Kuz’min, V.G. Likhvansteva, M.V. Samoylov, L.V. Seleznev, D.V. Sinitsyn, S.D. Zakharov. “*In vitro* femtosecond laser subsurface micro-disruption inside human cornea and pre-cleared sclera.” Laser Physics Letters **7**(6), pp 463-466, 2010.

6 Lodish H, Berk A, Zipursky SL, et al. Molecular Cell Biology. 4th edition. New York: W. H. Freeman; 2000. Section 22.3, Collagen: The Fibrous Proteins of the Matrix. Available from: http://www.ncbi.nlm.nih.gov/books/NBK21582/

7 M. Han, G. Giese, J. Bille. “Second harmonic generation imaging of collagen fibrils in cornea and sclera.” Optics Express **13**(15), pp 5791-5797, 2005.

8 F.W. Keeley, J.D. Morin, S Vesely. “Characterization of Collagen from Normal Human Sclera.” Exp. Eye Res. **39**, pp 533-542, 1984.

9 Y. Komai, T. Ushiki. “The three-dimensional organization of collagen fibrils in the human cornea and sclera.” Investigative Ophthalmology & Visual Science **32**(8), July 1991.

10 R. LaComb, O. Nadiarnykh, S. S. Townsend, and P. J. Campagnola. “Phase matching considerations in second harmonic generation from tissues: Effects on emission directionality, conversion efficiency and observed morphology.” Optics Communications **281**, pp 1823-1832 2008.

11 G. Hall, K. Elicieri, P. Campagnola. “Simultaneous determination of the second-harmonic generation emission directionality and reduced scattering coefficient from three-dimensional imaging of thick tissues.” Journal of Biomedical Optics **18**(11), 116008, November 2013.

12 J. H. K. Liu, D. F. Kripke, R. E. Hoffman, M. D. Twa, R. T. Loving, K. M. Rex, B. L. Lee, S. L. Mansberger, and R. N. Weinreb.. “Elevation of Human Intraocular Pressure at Night under Moderate Illumination.” IOVS **40**(10), September 1999.

13 R. Boyd. “Nonlinear Optics.” Burlington, MA: Academic Press. ISBN: 978-0-12-369470-6. 2008. Chapter 2.

14 Y. Liu, S. Sun, S. Singha, M. Cho, R. Gordon. “3D femtosecond laser patterning of collagen for directed cell attachment.” Biomaterials **26**, 2005.

15 C. Schaffer, B. Nishimura, E. Mazur. “Thresholds for femtosecond laser-induced breakdown in bulk transparent solids and water.” Proceedings of SPIE, 3451, 1998.

16 A. N. Bashkatov, E. A. Genina, V. I. Kochubey, V. V. Tuchin. “Optical Properties of Human Sclera in Spectral Range 370-2500nm.” Biomedical Optics and Spectrometry **109**(2) pages 197-204, 2010.

Chapter 6

Conclusions and Future Work

Since the first demonstration of CPA [1], ultrashort pulses have found many applications, and the CBG has served as a compact pulse stretcher-compressor for CPA systems [2]. We explored the limitations in the reciprocity of a CBG as well as the power-handling capabilities of a CVBG in a high average power system.

We have demonstrated that the reciprocity of a CBG could be optimized to provide high efficiency pulse compression. Apodization has been known to compromise bandwidth and improve pulse quality, and we show that the degree of apodization could be carefully selected to meet design criteria for the efficiency, bandwidth, and pulse quality of a CBG-based CPA system. The degree of apodization was measured here as the power of the super Gaussian used as the apodization function.

We have also explored the use of a CVBG in a high average power system to determine limitations in its performance. The primary limitation was the spatial quality of the compressed signal beam, and this was the primary limitation because the CVBG was found to bend under a thermal load. This bending could be suppressed mechanically, namely by the mounting conditions of the CVBG. In the case where the bending of the CVBG was fully suppressed, the beam quality remained the primary limitation in the performance of the CVBG, where absorption

of the incident beam transformed the CVBG into a GRIN lens with substantial chromatic aberration, resulting in spatial distortions to the reflected beam.

Understanding the performance limitations of the CVBG in a high average power CPA system, we were able to apply the CVBG to a 50 W average power CPA system with a variable repetition rate. With this system, we studied the formation of HSFL on (100) Si with 600 fs pulses centered at 1060 nm at a repetition rate of 49 MHz, and we found that the average irradiance heated the Si locally, thereby growing a thermal oxide that competed with HSFL formation. HSFL formation was the dominant mechanism defining Si morphology when the average irradiance was minimized. Moreover, the variable repetition rate of the CPA system has made it possible to explore the dependence of HSFL formations on the lifetime of Frenkel defects in Si.

Finally, we have demonstrated that compact fiber CPA system could be used in ophthalmology, where B-SHG could be used as a non-invasive probe in sclera to measure local properties of the tissue. These tissue properties could then be used to approximate the energy needed for subsurface damage. This opened the door to achieving subsurface scleral surgery with femtosecond lasers at a precise depth for treating infirmities such as glaucoma and presbyopia.

6.1 Unanswered questions

The work presented here left open a number of questions that could be addressed with additional work.

One question involved the fluence at focus as (100) Si samples were irradiated with the 50 W laser. The fluences reported for the formations described in Chapter 4 were the fluences at the focus of an unscattered beam. Because of thermal oxidation, however, the air-SiO_2 interface

would have provided a weak reflection that reduced fluence at the Si-SiO_2 interface. Moreover, images taken after irradiation showed that the oxide broke at some point during irradiation, and the rough air-SiO_2 interface would have scattered the incident beam during irradiation and distorted the wavefront of the beam at the surface of the Si, further reducing the fluence at the Si surface. Moreover, when the thickness of the oxide became comparable to the Rayleigh range of the incident beam, as in the case when the reported fluence was 0.34 J/cm^2, the beam probably started to diffract by the time it reached the surface of the Si, and fluence would have been reduced further. The actual fluence at the Si interface was not well characterized, however. With a more thorough understanding of the scattering and wavefront distortions of the incident beam by the rapidly expanding thermal oxide, we could have properly characterized the fluence at the Si surface in these experiments.

Explaining the thermal oxidation more thoroughly would involve modeling rapid thermal oxidation on irradiated Si. Because the SiO_2 formations formed on the millisecond time scale, this model could not ignore the time-dependent term of the heat equation, which was ignored in Chapter 3. Moreover, the thermal conductivity of Si [4] and of SiO_2 [5 for thin layers up to 2.3 μm thick, 6 for bulk] was temperature dependent, and the temperature distribution changed as the SiO_2 layer grew, adding further complexity to the model. Another factor to consider would be the temperature dependence of the refractive index of SiO_2, which would affect the scattering of incident pulses off the air-SiO_2 interface. These might not comprise all the factors needed for such a model, but understanding the thermal oxidation during irradiation would allow us to explain more fully the conditions under which HSFL formed.

One of the more interesting questions involved the absence of LIPSS on Si when samples were irradiated with a stationary beam. Within one beam diameter, the local Si atoms were

irradiated for an exposure time on the order of 10 ms. When a single region of Si was irradiated, however, no LIPSS could be seen, in contrast to experiments performed on GaAs [3]. To demonstrate this, a sample was irradiated with a beam that remained stationary for a given dwell time. To control the dwell time, galvanometric scanners (Cambridge Technologies, 1064 nm dielectric mirrors) positioned the beam on the sample, then moved the beam away to a beam dump after the desired dwell time had elapsed. Because single irradiated regions were difficult to find with an SEM, we used the largest spot size ($1/e^2$ diameter: 33 μm) for which we could make markers at a fluence of 0.5 J/cm^2 with the 50 W laser. To achieve this spot size, a 10 cm lens focused the beam, and the galvos operated between the lens and the sample.

To cool the Si when irradiating at such a high average power, the sample was mounted on a cooper cooling block that had 8 °C process water flowing through it. The copper mount was meant to remove heat from the back of the sample, where heat was conducted through the sample at a rate determined by the thermal conductivity of Si [4]. The region was exposed under similar conditions for which LIPSS were made (0.22 J/cm^2, 49 MHz, 20 ms exposure time for 10^6 pulses), (Figure 6.1). EDS measurements confirmed that the region did not have a thick oxide on the surface.

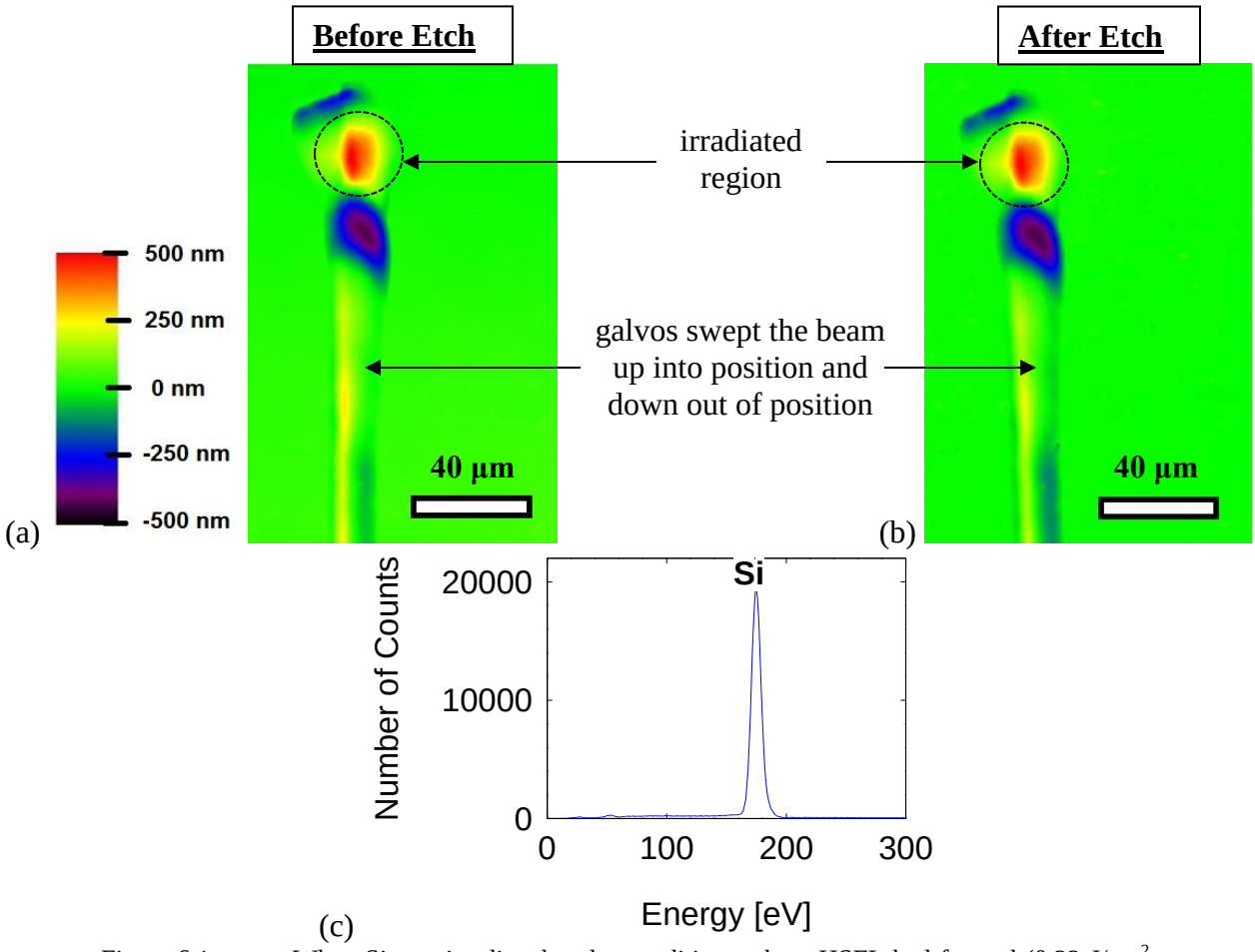

Figure 6.1 When Si was irradiated under conditions where HSFL had formed (0.22 J/cm^2, 10^6 pulses, 23.4 W average power) but with a stationary beam instead of a translated beam, a mound of Si formed on the surface. (a) A mound formed on top to a thickness of 0.5 µm (measured with the LEXT; this false color image indicated the height of the mound, where color represented height (colorbar on left)). After etching, (b) LEXT measurements showed no change in surface morphology (false color image, same colorbar in (a) applied to this image). (c) An EDS measurement confirmed that only Si remained after etching. The region was irradiated with a 23.4 W average power beam at a repetition rate of 49 MHz (pulse energy was 0.48 µJ) for 20 ms (10^6 pulses), and 1/e^2 spot diameter was 33 µm (target fluence was 0.22 J/cm^2). The sample was fixed to a copper cooling mount. Although SiO_2 formed above HSFL for a fluence around 0.2 J/cm^2 on Si, it did not form for a stationary beam.

Analyzing the region with an SEM (Figure 6.2) revealed that no LIPSS had formed on the surface.

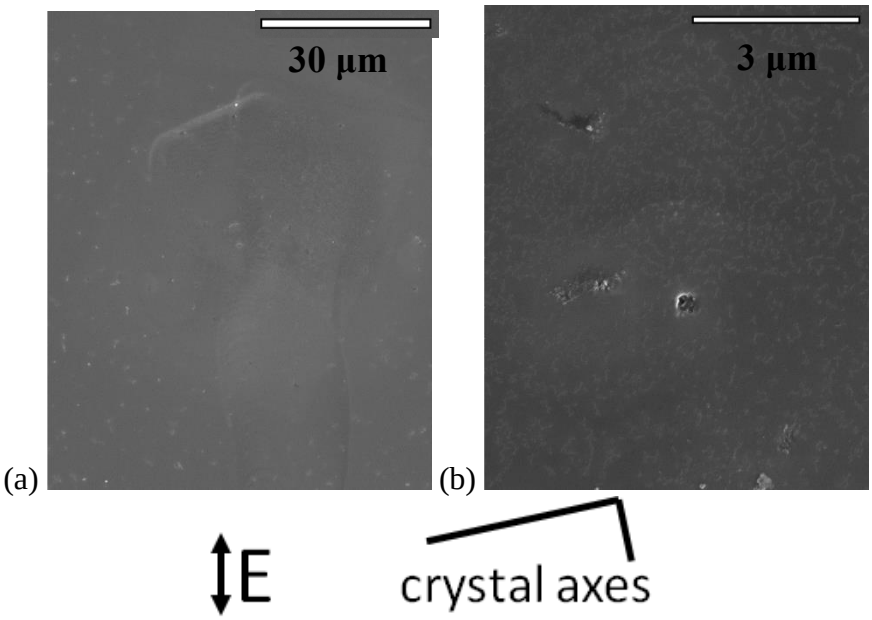

Figure 6.2 No LIPSS formed when Si was irradiated with a stationary beam (0.22 J/cm^2, 10^6 pulses, 23.4 W average power). (a) The irradiated region was difficult to see in an SEM on a 30 µm scale, and (b) closer examination revealed no LIPSS formation on the surface. For the sample above, parameters and experimental conditions were the same as in Figure 6.1. Although HSFL formed for fluences around 0.2 J/cm^2 on Si, they did not form for a stationary beam.

If the sample were irradiated further, however, a crater formed in the region. As shown below (Figure 6.3), Si was irradiated under the same experimental conditions as shown above (Figure 6.2) but for 50 ms and 100 ms.

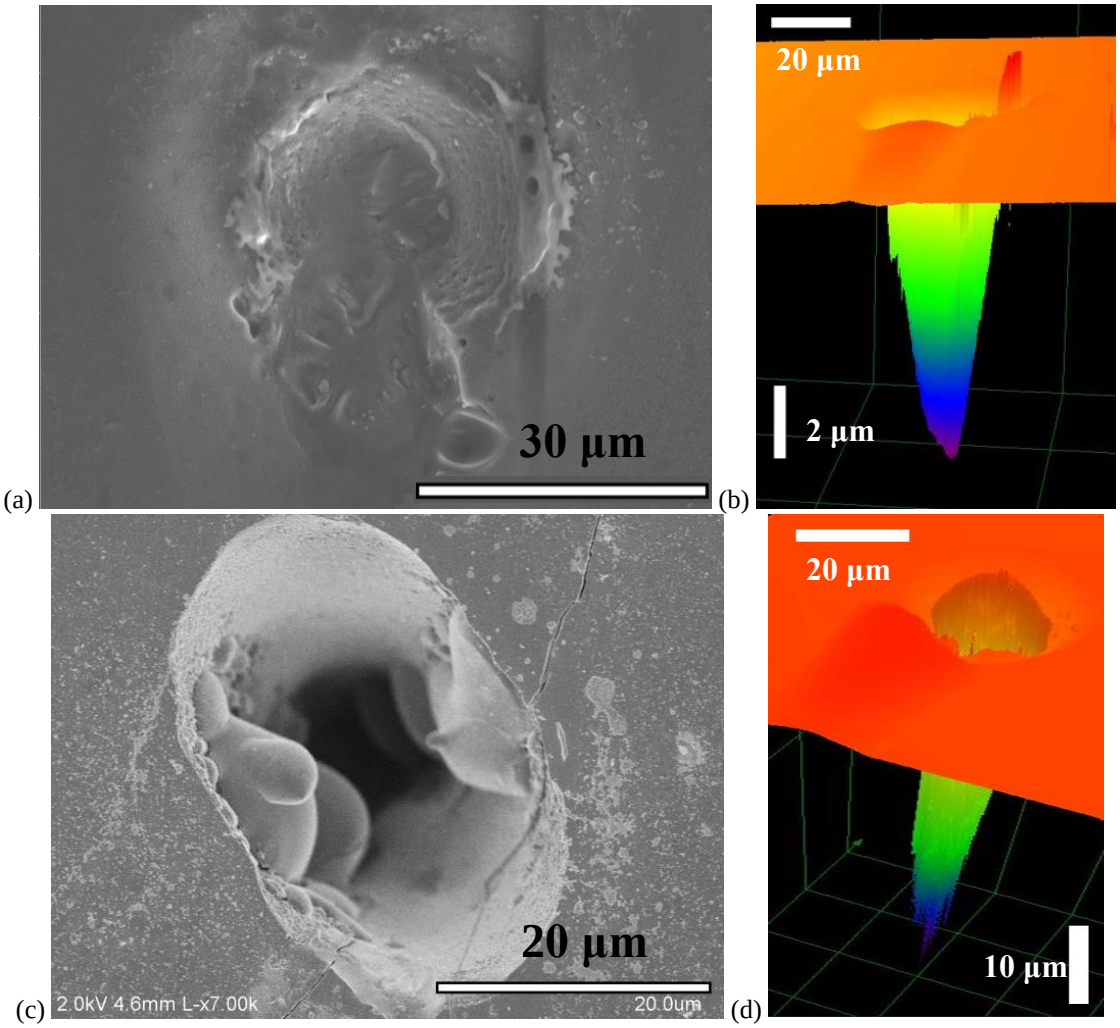

Figure 6.3 Crater formation on Si. When Si was irradiated for too long, a crater formed in the surface. For the sample above, parameters were the same as in Figure 6.2 except that the exposure time varied. (a) An SEM image of exposure for 50 ms ($2.5*10^6$ pulses) shows a hole, and (b) 3D LEXT measurements show the hole to be 11.0 µm deep (scale bars: 20 µm laterally and 2 µm deep). (c) An SEM image for 100 ms ($5*10^6$ pulses) exposure, for which (d) it was impossible to measure the depth (3D LEXT measurement estimated the depth to be 34.2 ± 9.8 µm) (scale bars: 20 µm laterally and 10 µm deep). Images were taken after etching the sample. We saw here that the thermal load limited the exposure time for a given region of the sample.

Given that irradiation conditions were similar to those for which HSFL formed, it was very interesting to see this Si morphology, especially without a thick oxide layer, as shown by the EDS measurement. The samples had been cooled from behind, and because of the high thermal conductivity of Si (156 W/mK at 300 °K [4]), enough heat may have been removed to prevent the rapid thermal oxidation reported in Chapter 4. If that were so, the Si morphology

observed above remains a mystery, as does the fact that we did not see any LIPSS when irradiating Si with a stationary beam.

Another interesting question involved the shape of the focused beam used to form LIPSS here. The Gaussian beams used for these experiments provided variable fluence to the samples, where the fluence in the wings was much lower than that of the peak. Consequently, when the pulses irradiated samples, the target fluence for the experiment was in center of the beam, but lower fluences affected the periphery of the region. A flat-top beam would provide uniform fluence over a given region rather than this variable fluence. Because of the tight requirements in the beam delivery system described in chapter 4, the pulses needed to be delivered as Gaussian beams to minimize beam expansion along the beam path and thereby minimize clipping on the optics. If the beam were to be reshaped, it would need to happen shortly before focusing the beam on target.

As for the prospect of scleral surgery, the most pressing question was how the results from *ex vivo* porcine scleral samples would have translated into *in vivo* human sclera. Obtaining the answer to this question would have required several steps, each answering a lesser question. For example, one could ask if the results taken *ex vivo* could be applied to tissue *in vivo*, and the answer would involve experimentation in sedated animals, which were usually rabbits. For both porcine and rabbit tissue, scattering values for infrared light in sclera differ from those of humans [7], and so results from *in vivo* rabbits would not directly translate to human sclera. If such experiments were to reveal enough information that a clear understanding of the surgical procedure could be developed for people, then *ex vivo* experiments in humans would probably be enough to verify that understanding. Otherwise, there would be no way to avoid experimentation

in *in vivo* human sclera. To establish a novel surgical procedure in human sclera, meeting guidelines from the Food and Drug Administration (FDA) would also be necessary.

6.2 References

1 D. Strickland and G. Mourou. “Compression of Amplified Chirped Optical Pulses.” Optics Communications **56**(3), pp. 219-221, 1985.

2 P. Tournois, P. Hartemann, “Bulk chirped Bragg reflectors for light pulse compression and expansion.” Optics Communications **119,** pp 569-575, 1995.

3 M. Abere. “From Point Defects to Ripples: Ultrafast Laser Induced High Spatial Frequency Laser Induced Periodic Surface Structures.” Dissertation, University of Michigan, Ann Arbor 2015. Print.

4 C. Prakash. “Thermal conductivity variation of silicon with temperature.” Microelectronic Reliability **18**, p 333, 1978.

5 M. B. Kleiner. “Thermal conductivity measurements of thin silicon dioxide films in integrated circuits.” IEEE Transactions on Electron Devices **43**(9), pp 1602-1609, 1996.

6 Y. S. Touloukian, Ed. Thermophysical Properties of Matter. New York IFI/Plenum, **2**(193), 1970.

7 A. N. Bashkatov, E. A. Genina, V. I. Kochubey, and V. V. Tuchin. “Optical Properties of Human Sclera in Spectral Range 370–2500 nm.” Biomedical Optics and Spectroscopy **109**(2) pp 197-204, 2010.

Appendix:

Analytical Model of Beam Distortions in Thermally Loaded Azimuthally-Symmetric Reflective CVBG

A1. Analytical Model

A high-power beam incident on a CVBG induces a thermal load on the CVBG via absorption of the beam, which results in a volumetric temperature distribution determined both by the shape of the beam and by the power distribution along the CVBG. This temperature distribution, in turn, alters the refractive index by the thermo-optic effect, which transforms the CVBG into a graded-index (GRIN) lens. Because each spectral component reflects from a unique longitudinal position in the CVBG, it encounters a GRIN lens of a unique thickness and, therefore, a unique focal length. The result is that when compressing an amplified stretched pulse, the beam becomes chromatically aberrated.

To understand this phenomenon more completely, we begin by analyzing the volumetric temperature distribution. The temperature distribution is a solution to the steady-state heat transfer equation, given in Eq. 3.5 and repeated below [A1.1]. In this equation, T(r,z) is the volumetric temperature distribution, k is the coefficient of heat conduction, and Q(r,z) is the heat source. In the case of a high average power Gaussian beam incident on a CVBG, heat is generated by absorption of the incident beam, where α is the absorption coefficient (in W/m), P(z) is the peak power at longitudinal point z, and w_0 is the $1/e^2$ beam width.

$$\nabla \cdot \left(-\mathrm{k}\nabla \mathrm{T}(\mathrm{r},\mathrm{z})\right) = Q(r,z) \tag{A1.1}$$

$$Q(r,z) = \frac{\alpha P(z)}{(\pi w_0^2/2)} \exp\left\{-\frac{2r^2}{w_0^2}\right\} \tag{A1.2}$$

$$\nabla \cdot \left(-\mathrm{k}\nabla \mathrm{T}(\mathrm{r},\mathrm{z})\right) = \frac{2\alpha P(z)}{\pi w_0^2} \exp\left\{-\frac{2r^2}{w_0^2}\right\} \tag{A1.3}$$

$$\nabla \cdot \left\{-\mathrm{k}\left(\frac{dT}{dr}\boldsymbol{r} + \frac{1}{r}\frac{dT}{d\theta}\boldsymbol{\theta} + \frac{dT}{dz}\boldsymbol{z}\right)\right\} = \frac{2\alpha P(z)}{\pi w_0^2} \exp\left\{-\frac{2r^2}{w_0^2}\right\} \tag{A1.4}$$

$$-k\left(\frac{d^2T}{dr^2} + \frac{1}{r}\frac{dT}{dr} + \frac{1}{r^2}\frac{d^2T}{d\theta^2} + \frac{d^2T}{dz^2}\right) = \frac{2\alpha P(z)}{\pi w_0^2} \exp\left\{-\frac{2r^2}{w_0^2}\right\} \tag{A1.5}$$

We can solve this equation by assuming that the temperature distribution takes the form $T(r, \theta, z) = T_r(r)*T_\theta(\theta)*T_z(z)+T_0$. Because the heat source here depends both on r and z, this assumption would hold if conduction were primarily in one direction, so that terms on the left-hand side vary along only one coordinate and the temperature distribution in the other coordinates would closely follow the heat source (e.g. so that $P(z)/T_z(z)$ would be constant (Figure 1A)). We find that conduction would be primarily radial under certain cooling conditions and for a particular incident spectrum. To eliminate the azimuthal component of the conduction, the CVBG would need to be cooled uniformly on all its sides, which would be nearly equidistant from the center, and the heat source would need to have no azimuthal dependence. To minimize the longitudinal component of the conduction, the length of the CVBG would need to be much greater than its width, it would need to be insulated at its front and back facets, and the longitudinal components of the heat source would need to be linear (which comes from matching the spectrum of the incident beam to the reflectivity spectrum of the CVBG).

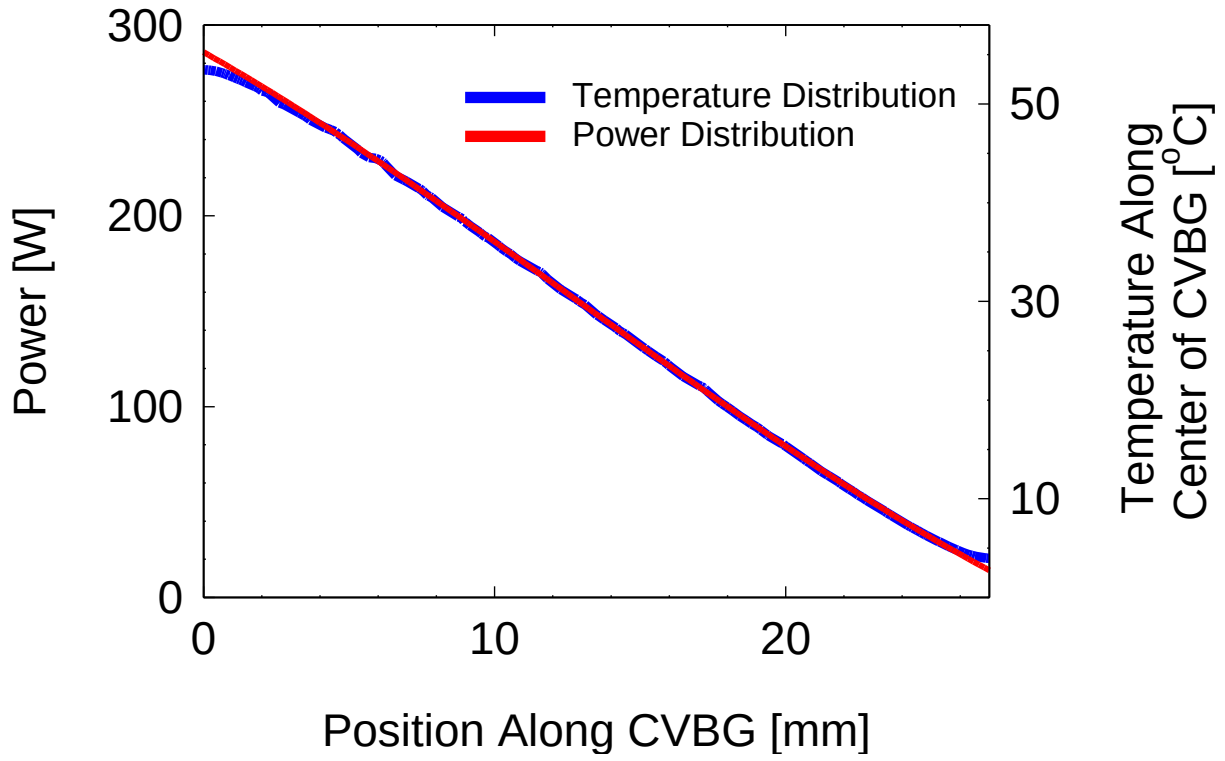

Figure 1A Longitudinal power distribution and temperature distribution along CVBG. Longitudinal power distribution $Q_z(z)$ compared to temperature distribution $T_z(z)$ in center of CVBG for a CVBG (5 mm wide, 6 mm high, 27 mm long) insulated at the front and back facets but conductively cooled on its edges, with an incident beam of 2 mm ($1/e^2$ diameter). The temperature and power distributions match almost perfectly, indicating that conduction longitudinally along the CVBG is proportional to the power distribution (i.e. radial conduction is the primary form of conduction). The approximation fails marginally at the ends of the CVBG.

This reduces the heat transfer equation to an ordinary differential equation with respect to radius. Here, each component of the temperature distribution and the heat source is written in a short-hand form (e.g. $T_r(r) \rightarrow T_r$, $T_\theta(\theta) \rightarrow T_\theta$, etc.) and ' denotes differentiation.

$$T_\theta T_z \left(T_r'' + \frac{T_r'}{r}\right) = \frac{Q_r Q_z}{-k} = \frac{2\alpha P(z)}{-k\pi w_0^2} \exp\left\{-\frac{2r^2}{w_0^2}\right\} \tag{A1.6}$$

$$T_\theta T_z (r T_r'' + T_r') = \frac{2\alpha P(z)}{-k\pi w_0^2} r \exp\left\{-\frac{2r^2}{w_0^2}\right\} \tag{A1.7}$$

$$T_\theta T_z (\int r T_r'' dr + T_r) = C_1(\theta, z) - \frac{2\alpha P(z)}{k\pi w_0^2} \int r \exp\left\{-\frac{2r^2}{w_0^2}\right\} dr \tag{A1.8}$$

$$T_\theta T_z (rT_r' - \int T_r' dr + T_r) = C_1(\theta, z) + \frac{\alpha P(z)}{2\pi k} \exp\left\{-\frac{2r^2}{w_0^2}\right\} \quad \text{(A1.9)}$$

$$T_\theta T_z (rT_r' - T_r + T_r) = C_1(\theta, z) + \frac{\alpha P(z)}{2\pi k} \exp\left\{-\frac{2r^2}{w_0^2}\right\} \quad \text{(A1.10)}$$

$$rT_\theta T_z T_r' = C_1(\theta, z) + \frac{\alpha P(z)}{2\pi k} \exp\left\{-\frac{2r^2}{w_0^2}\right\} \quad \text{(A1.11)}$$

$$T_\theta T_z T_r' = \frac{C_1(\theta,z)}{r} + \frac{\alpha P(z)}{2\pi k} \frac{1}{r} \exp\left\{-\frac{2r^2}{w_0^2}\right\} \quad \text{(A1.12)}$$

$$T_\theta T_z T_r = C_0(\theta, z) + C_1(\theta, z) \ln(r) + \frac{\alpha P(z)}{2\pi k} \int \frac{1}{r} \exp\left\{-\frac{2r^2}{w_0^2}\right\} dr \quad \text{(A1.13)}$$

$$T_\theta T_z T_r = C_0(\theta, z) + C_1(\theta, z) \ln(r) + \frac{\alpha P(z)}{4\pi k} Ei\left(-\frac{2r^2}{w_0^2}\right) \quad \text{(A1.13a)}$$

To solve for C_1, we use the initial condition that dT/dr = 0 at r = 0 [A1.16], which is to say that the temperature distribution is radially symmetric about the middle of the CVBG.

$$T'(0, \theta, z) = \lim_{r \to 0} T'(r, \theta, z) = 0 \quad \text{(A1.14)}$$

$$\lim_{r \to 0} \frac{1}{r} \left[C_1(\theta, z) + \frac{\alpha P(z)}{2\pi k} \exp\left\{-\frac{2r^2}{w_0^2}\right\}\right] = 0 \quad \text{(A1.15)}$$

$$C_1(\theta, z) = -\frac{\alpha P(z)}{2\pi k} \quad \text{(A1.16)}$$

The other initial condition is that the temperature at the boundary r_0 is known to be $T_r(r_0) = T_b$ [A1.17].

$$T(r_0, \theta, z) = T_b = C_0(\theta, z) + \frac{\alpha P(z)}{2\pi k} \left[\frac{1}{2} Ei\left(-\frac{2r_0^2}{w_0^2}\right) - \ln(r_0)\right] \quad \text{(A1.17)}$$

$$C_0(\theta, z) = T_b + \frac{\alpha P(z)}{2\pi k} \left[\ln(r_0) - \frac{1}{2} Ei\left(-\frac{2r_0^2}{w_0^2}\right)\right] \quad \text{(A1.18)}$$

This is the full temperature distribution [A1.19]. Note that it is identical to the temperature distribution for a cylindrical rod heated with a Gaussian beam [1].

$$T(r,\theta,z) = T_b + \frac{\alpha P(z)}{2\pi k}\left[\ln\left(\frac{r_0}{r}\right) + \frac{1}{2}Ei\left(-\frac{2r^2}{w_0^2}\right) - \frac{1}{2}Ei\left(-\frac{2r_0^2}{w_0^2}\right)\right] \quad \text{(A1.19)}$$

The parabolic approximation of T(r, θ, z) is important because it will simplify the calculations of the spatial distortions in the reflected beam that arise indirectly from the temperature distribution. More precisely, the gradient of the temperature distribution [Eq. A1.20] will affect the reflected beam.

$$\nabla T(r,\theta,z) = \frac{\alpha P(z)}{2\pi k} * \frac{1}{r}\exp\left(-\frac{2r^2}{w_0^2}\right) \quad \text{(A1.20)}$$

Writing the first few terms of the Taylor expansion of this gradient shows more clearly where the parabolic approximation fails with respect to beam radius.

$$\nabla T(r,\theta,z) = \frac{\alpha P(z)}{2\pi k w_0}\left[-2\left(\frac{r}{w_0}\right) + 2\left(\frac{r}{w_0}\right)^3 - \frac{4}{3}\left(\frac{r}{w_0}\right)^5 + \cdots\right] \quad \text{(A1.21)}$$

From this, we see that the parabolic approximation holds for the same diameter of the beam regardless of the beam radius.

This temperature gradient induces a localized change in refractive index (by the thermo-optic effect), as described in Eq. A2.1, which causes the reflected beam to focus as it exits the CVBG. Here, $\frac{dn}{dT}$ is the thermo-optic coefficient.

$$n = n_0 + \frac{dn}{dT}\Delta T + \left(\frac{d^2n}{dT^2}\right)\Delta T^2 + \cdots \quad \text{(A2.1)}$$

Where nonlinear terms in Eq. A2.1 were insignificant (≥ 500 °C, [2]), the change in refractive index depended only on the linear term.

$$n = n_0 + \frac{dn}{dT}\Delta T \quad \text{(A2.2)}$$

This gradient index transforms the CVBG into a GRIN lens, which causes light to refract as it propagates through the lens (Figure 2A). A common GRIN lens is the SELFOC lens, which has a graded refractive index characterized by the parabolic profile given in Eq. A3.1, where $n_0\gamma^2 r$ is the gradient of the refractive index [3, 4].

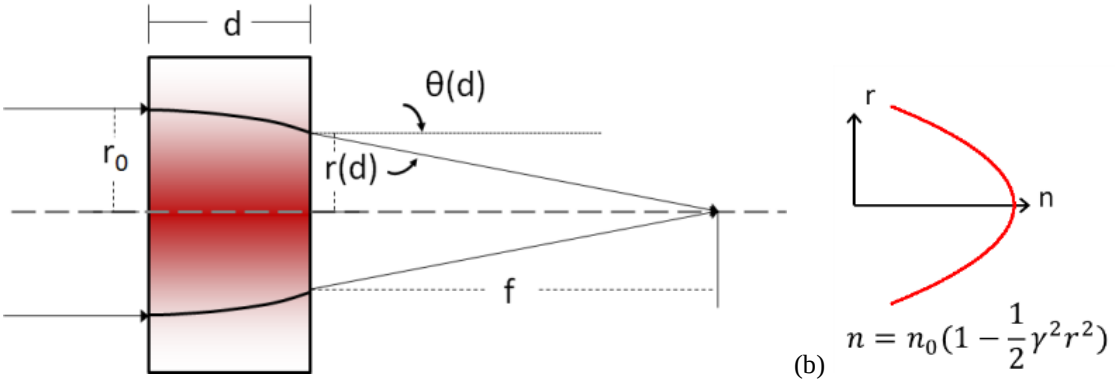

Figure 2A Fundamental operation of GRIN lens. (a) Collimated light incident on a graded-index lens refracts inside the lens and comes to a focus on the opposite side. The lens has thickness *d*, and collimated rays (θ_0=0) incident at r_0 away from the optical axis refract inside

the lens and emerge at radial distance r(d) and at angle θ(d). These rays intersect the optical axis at a distance f from the lens. (b) The refractive index profile is typically parabolic with respect to radius and is characterized by $n=n_0(1-\frac{1}{2}\gamma^2r^2)$.

$$n(r) = n_0\left(1 - \frac{1}{2}\gamma^2 r^2\right) \tag{A3.1}$$

The behavior of the SELFOC lens has been characterized before [4], and its behavior describes that of the thermally-loaded CVBG when the parabolic approximation of the refractive index holds in the CVBG. To make this approximation, we must find that all higher-order terms in Eq. A1.19 are negligible.

$$T(r,\theta,z) \approx T(0,\theta,z) - \frac{\alpha P(z)}{2\pi k}\frac{r^2}{w_0^2} \tag{A4.1}$$

For a SELFOC lens of thickness d, incident rays follow a sinusoidal path with a periodic length of $2\pi/\gamma$ [5]. The radial position and angle of each ray at distance d, therefore, are characterized by Eq. A5.1 and Eq. A5.2.

$$r(d) = r_0\cos(\gamma d) + \frac{\theta_0}{\gamma}\sin(\gamma d) \tag{A5.1}$$

$$\theta(d) = \frac{dr}{dz} = -\gamma r_0\sin(\gamma d) + \theta_0\cos(\gamma d) \tag{A5.2}$$

This can be represented in matrix form, as shown in Eq. A5.3.

$$M\begin{bmatrix} r_0 \\ \theta_0 \end{bmatrix} = \begin{bmatrix} \cos(\gamma d) & \frac{\sin(\gamma d)}{\gamma} \\ -\gamma\sin(\gamma d) & \cos(\gamma d) \end{bmatrix}\begin{bmatrix} r_0 \\ \theta_0 \end{bmatrix} = \begin{bmatrix} r(d) \\ \theta(d) \end{bmatrix} \tag{A5.3}$$

The focal length of this GRIN lens is given by Eq. A5.4, where n_1 is the refractive index outside the lens [1].

$$f = \frac{(n_1/n_0)}{\gamma sin(\gamma d)} \tag{A5.4}$$

When γd is small enough that sin(γd) ≈ γd (and cos(γd) ≈ 1), the focal length and matrix representation of the lens can be simplified.

$$f = \frac{(n_1/n_0)}{\gamma^2 d} \tag{A5.5}$$

$$M = \begin{bmatrix} 1 & d \\ -\gamma^2 d & 1 \end{bmatrix} \tag{A5.6}$$

To model the thermally-loaded CVBG, we use a series of GRIN lenses of small thickness *d*, for which we denote the matrix of the i^{th} lens as shown [Eq. A5.7].

$$M_i = \begin{bmatrix} 1 & d \\ -\gamma_i^2 d & 1 \end{bmatrix} \tag{A5.7}$$

The CVBG can then be modeled as a series of N GRIN lenses placed back-to-back, for which the matrix of the system can be calculated with Eq. A5.7. Here, we assume that terms of d^4 and higher are negligible.

$$M_N = \prod_{i=1}^{N} M_i \approx$$

$$\begin{bmatrix} 1-\sum_{i=1}^{N}(i-1)\gamma_i^2 d^2 & Nd-\sum_{i=1}^{N}((i-1)N-i(i+1))\gamma_i^2 d^3 \\ -\sum_{i=1}^{N}\gamma_i^2 d+\sum_{i=1}^{N}\sum_{j=i+2}^{N}(j-i-1)\gamma_i^2\gamma_j^2 d^3 & 1-\sum_{i=1}^{N}(N-i)\gamma_i^2 d^2 \end{bmatrix} \quad \text{(A5.8)}$$

The effective focal length of the system can be determined with a collimated input. The exiting position and angle can be calculated from Eq. A5.8 to determine where the rays cross the axis of propagation [A5.9].

$$M_N \begin{bmatrix} r_0 \\ 0 \end{bmatrix} = \begin{bmatrix} r_{out} \\ \theta_{out} \end{bmatrix} = \begin{bmatrix} r_0(1-\sum_{i=1}^{N}(i-1)\gamma_i^2 d^2) \\ r_0\left(-\sum_{i=1}^{N}\gamma_i^2 d+\sum_{i=1}^{N}\sum_{j=i+2}^{N}(j-i-1)\gamma_i^2\gamma_j^2 d^3\right) \end{bmatrix} \quad \text{(A5.9)}$$

The output angle will change according to Snell's law.

$$n_0 \sin[\theta_{out}] = sin\theta_{air} \quad \text{(A5.10)}$$

From this, we can calculate where the rays will come to focus for the system of GRIN lenses.

$$tan\theta_{air} = -\frac{r_{out}}{f_{system}} \quad \text{(A5.11)}$$

Combining Eq. A5.9-A5.11, we find the focal length of the system [A5.12].

$$f_{system} = \frac{r_0\left(1-\sum_{i=1}^{N}(i-1)\gamma_i^2 d^2\right)}{\tan\left(sin^{-1}\left\{n_0 \, sin\left[r_0\left(\sum_{i=1}^{N}\gamma_i^2 d-\sum_{i=1}^{N}\sum_{j=i+2}^{N}(j-i-1)\gamma_i^2\gamma_j^2 d^3\right)\right]\right\}\right)} \quad \text{(A5.12)}$$

In the limit at thickness d→0, the focal length of the system takes the form of integration, where L_G is the finite length of the entire set of GRIN lenses.

$$\lim_{d\to 0} f_{system} = \frac{r_0\left(1-\int_0^{L_G}\gamma^2(z)zdz\right)}{\tan\left(sin^{-1}\left\{n_0\, sin\left[r_0\left(\int_0^{L_G}\gamma^2(z)dz-\int_0^{L_G}\left[\int_z^{L_G}(z'-z)\gamma(z')^2dz'\right]\gamma(z)^2dz\right)\right]\right\}\right)} \quad \text{(A5.13)}$$

Assuming that the output angle is small, the trigonometric functions can be removed with the approximations that $\tan\theta \approx \theta$ and $\sin\theta \approx \theta$.

$$\lim_{d\to 0} f_{system} = \frac{1-\int_0^{L_G}\gamma(z)^2zdz}{n_0\left(\int_0^{L_G}\gamma(z)^2dz-\int_0^{L_G}\left[\int_z^{L_G}(z'-z)(\gamma(z')^2)dz'\right]\gamma(z)^2dz\right)} \quad \text{(A5.14)}$$

The equation may be simplified further when the second term in the denominator is very small. The second term accounts for changes in refraction as each ray of the beam changes in angle. As the beam changes in angle, the refraction of the beam is more than the sum of angles from individual components in the system, and the second term in the denominator is the first-order approximation of that. If the overall output angle is small enough to ignore this first-order approximation, the second term in the denominator may be ignored [Eq. A5.15]. For reference, the error in the first approximation ($\tan\theta \approx \theta$) is $\leq$ 1% for up to 170 mrad.

$$\left[\int_z^{L_G}(z'-z)(\gamma(z')^2)dz'\right] \ll 1 \Rightarrow f_{system} \approx \frac{1-\int_0^{L_G}\gamma(z)^2zdz}{n_0\int_0^{L_G}\gamma(z)^2dz} \quad \text{(A5.15)}$$

We also observe that for the second term in the numerator, we can replace z with L_G to identify a lower bound for the equation and thereby find a minimum focal length of the system.

$$\int_0^{L_G} \gamma(z)^2 L_G dz > \int_0^{L_G} \gamma(z)^2 z dz \Rightarrow f_{system} > \frac{1-\int_0^{L_G} \gamma(z)^2 L_G dz}{n_0 \int_0^{L_G} \gamma(z)^2 dz} = \frac{1}{n_0 \int_0^{L_G} \gamma(z)^2 dz} - \frac{L_G}{n_0} \quad \text{(A5.16)}$$

We can eliminate the second term in Eq. A5.16 if the physical length of the entire GRIN lens system is very small when compared to the focal length of the system [Eq. A5.17].

$$f_{system} \approx \frac{1}{n_0 \int_0^{L_G} \gamma(z)^2 dz} \quad \text{(A5.17)}$$

This focal length applies to any system of SELFOC GRIN lenses placed back-to-back for which the aforementioned assumptions apply. For the case of a thermally-loaded CVBG, we can compare the gradient of the parabolic refractive index given in Eq. A3.1 with the gradient of the parabolic approximation of the thermally-loaded CVBG described in Eq. A4.1.

$$|\nabla n(r)| = n_0 \gamma^2 r \approx \frac{dn}{dT} \frac{\alpha P(z)}{\pi k w_0^2} r \quad \text{(A6.1)}$$

We can now rewrite Eq. A5.17 in terms of parameters related to the temperature distribution in the CVBG. Because of the assumptions made here, the result is nearly identical to that of [1], with the exception that we do not assume a specific longitudinal power distribution P(z) and so leave the integration of P(z) in the denominator.

$$f_{system} \approx \frac{1}{\int_0^{L_G} \frac{dn}{dT}\left(\frac{\alpha P(z)}{k\pi w_0^2}\right) dz} = \frac{k\pi w_0^2}{\alpha \frac{dn}{dT} \int_0^{L_G} P(z) dz} \tag{A6.2}$$

The effective focal length of a thermally-loaded CVBG must take this focal length into account twice because each spectral component in the incident beam travels to a point of reflection, represented by z(λ) in Eq. A6.3, and back to the front of the CVBG. Using the imaging equation, we find that the focal length of the CVBG is half that of Eq. A6.2.

$$\frac{1}{f_{eff}(\lambda)} = \frac{1}{f_{system}} + \frac{1}{f_{system}} \Rightarrow f_{eff}(\lambda) = \frac{k\pi w_0^2}{2\alpha \frac{dn}{dT} \int_0^{z(\lambda)} P(z) dz} \tag{A6.3}$$

Each spectral component focuses at a different location outside the CVBG. This results in longitudinal spatial distortions to the beam. The full effect of these distortions can be determined by calculating the spatial profile of each wavelength of the reflected beam and integrating across the spectrum. In general, the irradiance of the beam along the optical axis for any given transverse position is given by Eq. A7.1, where r is the radial distance from the optical axis, BW is the bandwidth of the CVBG, w_0 is the beam waist, z_R is the Rayleigh range, and s is the shift in focus relative to the focus of the central wavelength.

$$I(r) = \int_{-BW}^{BW} \frac{\exp\left\{-\left(\frac{r}{w_0(\lambda)}\right)^2 / \left(1 + \frac{s(\lambda)^2}{z_R^2(\lambda)}\right)\right\}}{1 + \frac{s(\lambda)^2}{z_R^2(\lambda)}} d\lambda \tag{A7.1}$$

Because the focal length of the CVBG is wavelength-dependent, it changes the shift in focus, the spot size, and the Rayleigh range of each wavelength. The shift in focus of each wavelength is $f_{eff}(\lambda)$ away from the plane of reflection for λ [Eq. A7.2].

$$s(\lambda) = f_{eff}(\lambda)(\lambda - \lambda_0)\frac{L}{BW} \tag{A7.2}$$

Using the imaging equation for paraxial rays [Eq. A7.3], we can determine where the beam would focus based on the Rayleigh range of the incident beam. From this, we can calculate the changes to the spot size [Eq. A7.6] and Rayleigh range [Eq. A7.8] of the beam for each wavelength.

$$\frac{1}{f} = \frac{1}{s_0} + \frac{1}{s_1} \tag{A7.3}$$

$$(f_{real})^{-1} = \left(f_{eff}(\lambda)\right)^{-1} + \left(z_{R,in}\right)^{-1} \tag{A7.4}$$

$$NA = \frac{\lambda}{\pi w_0} = w_{in}/f_{real} \tag{A7.5}$$

$$w_0(\lambda) = w_{0,in} f_{eff}(\lambda)/(f_{eff}(\lambda) + z_{R,in}) \tag{A7.6}$$

$$z_R(\lambda) = \pi w_{0,in}^2/\lambda \tag{A7.7}$$

$$z_R(\lambda) = z_{R,in} f_{eff}^2(\lambda)/\left(f_{eff}(\lambda) + z_{R,in}\right)^2 \tag{A7.8}$$

To calculate the spatial distortion to the beam based on these wavelength dependent parameters, we integrate the irradiance of the beam across the spectrum. The maximum irradiance is found along the optical axis (z = 0) [A7.9], and the radial point at which the irradiance is $1/e^2$ of the maximum is the $1/e^2$ radius of the beam ($w_{0,total}$) [A7.10].

$$I_{max} = \int_{-BW}^{BW} \frac{1}{1+\frac{f_{eff}(\lambda)^2}{z_R^2(\lambda)}} d\lambda \tag{A7.9}$$

$$I(w_{0,total}) = \int_{-BW}^{BW} \frac{\exp\left\{-M^2/\left(1+\frac{f_{eff}(\lambda)^2}{z_R^2(\lambda)}\right)\right\}}{1+\frac{s(\lambda)^2}{z_R^2(\lambda)}} d\lambda \tag{A7.10}$$

By setting $I(w_{0,total}) = I_{max}/e^2$, we solve for the M^2 value of the beam using numerical integration.

A2. References

1. M. E. Innocenzi, H. T. Yura, C. L. Fincher, and R. A. Fields. "Thermal modeling of continuous-wave end-pumped solid-state lasers." Applied Physics Letters **56**(19), May 1990.
2. C.Z. Tan and J. Arndt. "Temperature dependence of refractive index of glassy SiO_2 in the infrared wavelength range." Journal of Physics and Chemistry of Solids **61**, pp 1315-1320, 2000.
3. J. Evans. "Simple forms of equations of rays in gradient-index lenses." American Journal of Physics **58**(8), pp 773-778, August 1990.
4. M. Bass, editor. Handbook of Optics: Devices, Measurements, & Properties. New York, NY: McGraw-Hill, Inc. (vol. 2, ed. 2), 1995. ISBN 0-07-047974-7. Ch 9.
5. K. Nishizawa. "Chromatic aberration of the SELFOC lens as an imaging system." Applied Optics **19**(7), pp. 1052-1055, 1980.